December 2020

Analyzing Strain Localization, Kinematic Partitioning and Fluid Flow in the Pulo Do Lobo Metasedimentary Rocks Along the Southern Iberian Shear Zone, Andalucia, Spain

Nancy Alejandra Carman
University of Wisconsin-Milwaukee

ANALYZING STRAIN LOCALIZATION, KINEMATIC PARTITIONING AND FLUID FLOW IN THE PULO DO LOBO METASEDIMENTARY ROCKS ALONG THE SOUTHERN IBERIAN SHEAR ZONE, ANDALUCIA, SPAIN

by

Nancy Alejandra Carman

A Thesis Submitted in

Partial Fulfillment of the

Requirements for the Degree of

Master of Science

in Geosciences

at

The University of Wisconsin-Milwaukee

December 2020

ABSTRACT

ANALYZING STRAIN LOCALIZATION, KINEMATIC PARTITIONING AND FLUID FLOW ALONG IN THE PULO DO LOBO METASEDIMENTARY ROCKS ALONG THE SOUTHERN IBERIAN SHEAR ZONE, ANDALUCIA, SPAIN

by

Nancy Alejandra Carman

The University of Wisconsin-Milwaukee, 2020
Under the Supervision of Professor Dyanna Czeck

The Southern Iberian Shear Zone is a regional scale ductile shear zone that placed Beja-Acebuches metabasites over metapelite and quartzite rocks of the Pulo do Lobo Formation in a transpressional deformation with components of thrust and left-lateral movement. This project evaluates factors that contributed to strain localization at a variety of scales within the Pulo do Lobo formation, including lithologic variations, microstructures, and fluid flow. Additionally, microstructural data are used to test whether kinematic partitioning accompanied strain localization.

Grain scale asymmetric indicators of sigma-type clasts, S-C fabrics, and asymmetric folds indicate dominant thrust motion. Strain intensity and metamorphic grade increase towards the shear zone. Within about 170 m, relatively low-grade slates with regional slaty cleavage transition to garnet-zone amphibolite metamorphism and closely-spaced, strong schistose foliation. Microstructures indicate a gradual increase in crystal-plasticity towards the shear zone that likely allowed for gradual strain increase. However, fluid interaction promoted additional deformation mechanisms near the shear zone including diffusive mass transfer (most prevalent <50 m) and localized embrittlement (< 10 m). Isocon plots of major element concentrations indicate no

significant volume change across the strain gradient. Na_2O depletion paired with possible CaO enrichment are likely related to the stability of more Ca rich feldspars at higher metamorphic grade, suggesting that the fluid migration along the shear zone catalyzed metamorphic reactions. MgO enrichment is consistent with metasomatic alteration, potentially with a fluid source from the metabasites. K_2O enrichment, previously also documented in the metabasites, is additional evidence of fluid flow along the shear zone. The angle between C and C' fabrics is used to estimate kinematic vorticity across the strain gradient. In most samples, mean kinematic vorticity numbers between 0.86-0.98 indicate simple shear dominated strain, which did not vary significantly across the strain gradient.

Factors that controlled strain localization along the Southern Iberian Shear Zone vary with scale. At the terrane scale, the rheologic boundary between the Beja-Acebuches metabasites and the Pulo do Lobo formation is of primary importance. At the hm scale, fluid channeled along the shear zone further localized strain by enhancing strain softening metamorphic reactions and promoting diffusive mass transfer and embrittlement. At the cm-m scale, contrasting rheologies of quartzites and metapelites controlled strain localization. This study provides an example of how strain localization is accomplished within the mid-lower crust during tectonic events.

TABLE OF CONTENTS

LIST OF FIGURES

LIST OF TABLES

ACKNOWLEDGEMENTS

I would love to first thank my thesis advisor, Dr. Dyanna Czeck for all the opportunities she has given me as an undergraduate and graduate student in the Geosciences department at UW-Milwaukee. She has been one of the most influential and greatest mentors in my academic career and I'm glad I crossed paths with her. She is one of the most hard-working professors that I have met at UWM, that's dedicated to her work as well as her students. Her love of teaching is evident through her passion of structural geology, though not an easy topic, she makes it understandable and enjoyable. Her endless support, charisma, dedication in our project with the analysis and writing portions are greatly appreciated throughout the years I've been working with her. Her constructive criticism has pushed me in being confident enough to articulate my ideas to the scientific community, my peers, my friends, and my parents. These various ways of communication have helped mold my brain in presenting ideas to different audiences. Dyanna's endless efforts in getting funding for various projects, especially for acquiring the UWM RACAS awards and IRES grant EAR-1854155 for the Pulo do Lobo project are also to be noted and greatly appreciated. I would also love to thank Sheryl Stephenson for the collection of my first set of Pulo do Lobo samples. I would also love to thank my Spanish colleagues, Dr. Carlos Fernández and Dr. Manuel Díaz-Azpiroz for collecting my second set of samples in 2018 and third set in 2020. Their guidance in analysis as well as during the field, providing figures for the region, their vast knowledge of the region and hospitality is greatly appreciated. I would also love to thank the Office of Undergraduate Research for funding my research through SURF grants as an undergraduate when I embarked on the Pulo do Lobo journey. I would love to thank Dr. Lindsay McHenry for allowing me to use her XRF lab and her valuable input throughout the years. I would also love to thank the GSA Graduate Research Grant committee, UWM

Geosciences Department, and the Wisconsin Geological Society for giving me the opportunity to continue with my research. I want to thank my committee members Dr. Lindsay McHenry and Dr. Barry Cameron for being in my committee and always pushing me to do my best with regards to corrections on papers, letters of recommendations, and just talk about science.

I want to express my deepest gratitude to my former professor Dr. Orkan Umurhan, who always believed in me and expected no less of me. Without his support I wouldn't be where I am today as a future scientist. I would also love to thank my friend Austin Scheib, for his support and help over the years. In addition to that, I would love to thank my parents, grandparents and brother for their unconditional love and endless support ever since I was a young girl. I'm proud to say that I'll be the first one in the family with a Master's degree and will continue with the doctorate. I would also love to thank my in-laws, Gary and Sharon Carman, for their love, support and cheering me on until the finish line. Finally, I would like to thank my loving and caring husband, Jason Carman, for all the support and help he has given me during my graduate school career. He made sure to keep me fed and gave me that extra push to finish on time. I'll repay the same actions as he finishes his project. I'm deeply grateful and love Jason for all that he has done for me and we're truly a team and will continue to be in the years to come, thank you for always believing in me and encouraging me to do my best in everything.

CHAPTER 1: Introduction

1.1 Objective

The Southern Iberian Shear Zone (SISZ) located in southwestern Spain, is a ductile shear zone that formed during oblique collision. It has well-documented kinematics, variable strain magnitude, and fluid interaction (Díaz-Azpiroz & Fernández, 2005; Díaz-Azpiroz et al., 2006; Díaz-Azpiroz et al., 2007; Díaz-Azpiroz et al., 2008; Fernández et al., 2013), making it an ideal candidate for a detailed study on strain localization.

Strain localization refers to both the processes that cause strain intensity to be heterogeneously distributed within rocks, and the resultant highly strained zones that are adjacent to more weakly or undeformed rock. Strain localization is responsible for the formation of faults and ductile shear zones that allow stresses imparted by tectonic plate interactions to be accommodated along discrete structures. It is an important phenomenon throughout the crust resulting in major rheological contrasts that affect crustal architecture and tectonics, fluid flow, and potential seismicity. Unraveling the factors that cause strain localization is imperative to several of the "Grand Challenges" identified in a recent Tectonics Community Vision Document including: Understanding Variations in Rheology Throughout the Lithosphere (Challenge #2) and Understanding Fault Zone Behavior from Earth's Surface to the Base of the Lithosphere (Challenge #3) (Huntington et al., 2018).

Factors that cause strain to localize are lithological contrasts (Druguet et al., 2008; Horsman et al, 2008), reduced grain size (Lise and Savage, 1982), formation of deformation fabrics (Bukovská et al., 2016;), strain-softening metamorphic reactions (Beach et al., 1980), and/or fluid infiltration that enhances the weakening of the rock (Carter et al., 1990; Wawrzyniec

et al., 1999; Cox, 2002; Yonkee et al., 2013; Stephenson, 2018). The purpose of this project is to document strain localization and determine the dominant factor or factors that contribute to it in the metasedimentary rocks of the Pulo do Lobo (PdL) formation along the SISZ at a variety of scales. At the terrane scale, the SISZ localized at the rheological boundary between the Beja-Acebuches metabasites (BAM) to the northeast and the metasedimentary PdL rocks to the southwest. Geochemical and microstructural data from within the BAM demonstrated that localization was achieved through fluid migration from the shear zone conduit which caused retrograde metamorphism and strain softening (Stephenson, 2018; Czeck et al., 2019). However, within the PdL, the factors causing strain localization may be different. Unlike the BAM, the PdL contains heterogeneous lithologies: interbedded quartzites and schists. In this research, structural, petrologic, and geochemical observations are used to evaluate the relative importance of factors controlling strain localization within the PdL.

In tandem, we will be evaluating kinematic partitioning along the shear zone. In some studies, researchers have suggested that when strain magnitude partitions into domains of high and low strains, high strain zones are simple shear dominated and low strain zones are pure shear dominated (Jones and Tanner, 1995; Zhang et al., 2009). Kinematic partitioning can also occur due to geometrical constraints along curved shear zone segments (Giorgis et al., 2017), so the straight SISZ provides an opportunity to test the relationship between strain and kinematic partitioning without influence of geometric factors.

Combined with previous research in the BAM, this research allows us to more fully understand the factors controlling strain localization and kinematic partitioning along and across a major bounding shear zone, and can be used to better understand this process that is fundamental to our understanding of plate tectonics and the architecture of the crust.

1.2 Why would we want to study strain localization and fluid-rock interactions in the mid-lower crust?

Strain localization is essential to understand plate tectonics and the construction of the crust, however, the processes that control it are complex. For the ductile crust, most strain localization studies have focused on small-scale shear zones and shear bands (Braudy et al., 2016; Bukovská et al., 2016). However, fewer studies have analyzed ductile strain localization at the regional scale and tracked strain relative to distance from a shear zone (Arbaret et al. 2000, Carreras, 2001). The strain patterns that form are often complex with anastomosing geometries or multiple localized zones (Arbaret et al., 2000; Carreras, 2001), especially in regions with heterogeneous lithology, because localization is a complex process that may be controlled by a combination of lithological contrasts, reduced grain size, formation of deformation fabrics, and/or fluid infiltration.

Fluid can affect rock strength, deformation mechanisms, and strain localization in various ways (Carter et al., 1990). Fluids can affect rock strength by promoting mineral reactions that weaken the rock (Beach, 1980). Fluids can enhance brittle deformation when fluid pressure exceeds rock strength causing fracture (Axen et al., 2001). Conversely, fluids can enhance ductile deformation by accelerating diffusion rates (Wintsch and Yi, 2002) and/or causing hydrolytic weakening that promotes dislocation creep (Griggs, 1967). Rock deformation causes fabrics in cataclasites and mylonites that further create easy pathways for fluid flow. Ultimately, a positive feedback between deformation, fluids, and metamorphism promotes rock weakening and strain localization (Carter et al., 1990, Barnes et al., 2004).

1.3 Strain localization along the Southern Iberian Shear Zone

At the terrane scale, the SISZ itself is controlled by a major lithological boundary between BAM metabasite rocks to the northeast and PdL metasedimentary rocks to the southwest. Within the metabasite rocks, syndeformational fluid at least partially controlled SISZ strain localization (Stephenson, 2018; Czeck et al., 2019). In this study, we will test whether fluids also acted to localize deformation within the PdL by documenting geochemical, metamorphic, and microstructural signatures that record fluid flow and compare them to qualitative measures of strain intensity.

CHAPTER 2: Geologic Background

2.1 Tectonic Evolution

The Rheic Ocean separated the paleocontinents of Gondwana and Laurussia (Laurentia-Baltica-Avalonia) after the closure of Iapetus (Figure 1; Nance and Linnemann, 2008). This closure has long been recognized in Europe and is separate from the Iapetus Ocean closure which created the Caledonide orogen. The suture from the Rheic Ocean extends 10,000 km from Mexico to Turkey and its closure assembled the vast majority of the Variscan-Alleghanian-Ouachita orogeny as seen in Figure 2. However, the Rheic Ocean is not as well known in North America because its suture lies beneath the sediments of the Coastal Plain or was removed during the later opening of the Atlantic Ocean and Gulf of Mexico (Nance et al., 2010).

The Iberian Peninsula was assembled during the oblique tectonic collision between the Laurentia-Baltica and Gondwana continents during the closing of the Rheic Ocean during the Carboniferous Period (Figure 3). In southern Iberia, one can observe the record of its evolution from the rifting stages in the Cambrian to its final closure during the Variscan orogeny in the Late Paleozoic (Quesada et al., 1994). The Rheic Ocean suture is possibly preserved by the Beja-Acebuches metabasites of midocean ridge affinity and the Pulo do Lobo accretionary prism (e.g. Matte, 2001), although radiometric dates suggest that these rocks preserve a narrow related ocean basin rather than the Rheic Ocean proper (Azor et al., 2008). The Ossa-Morena zone was the Carboniferous edge of the Gondwana continent and, together with the Central Iberia zone to the north, includes a complete documentation of the Ordovician through Devonian passive margin of Gondwana during opening of the Rheic Ocean (Sánchez-García et al., 2003, 2008, 2010). Later, that edge of Gondwana was sutured to the exotic terrane South Portuguese zone

during Rheic Ocean closure. Deformation was localized along the suture between the Ossa-Morena and the South Portuguese zones and is known as the Southern Iberian Shear Zone (Figure 4). Suture zones are arguably important tectonic boundaries because they record the remnants of ancient ocean basins.

Figure 1: Early reconstruction of the Rheic Ocean prior to the closing of the Iapetus. Simplified map from Nance et al., 2010.

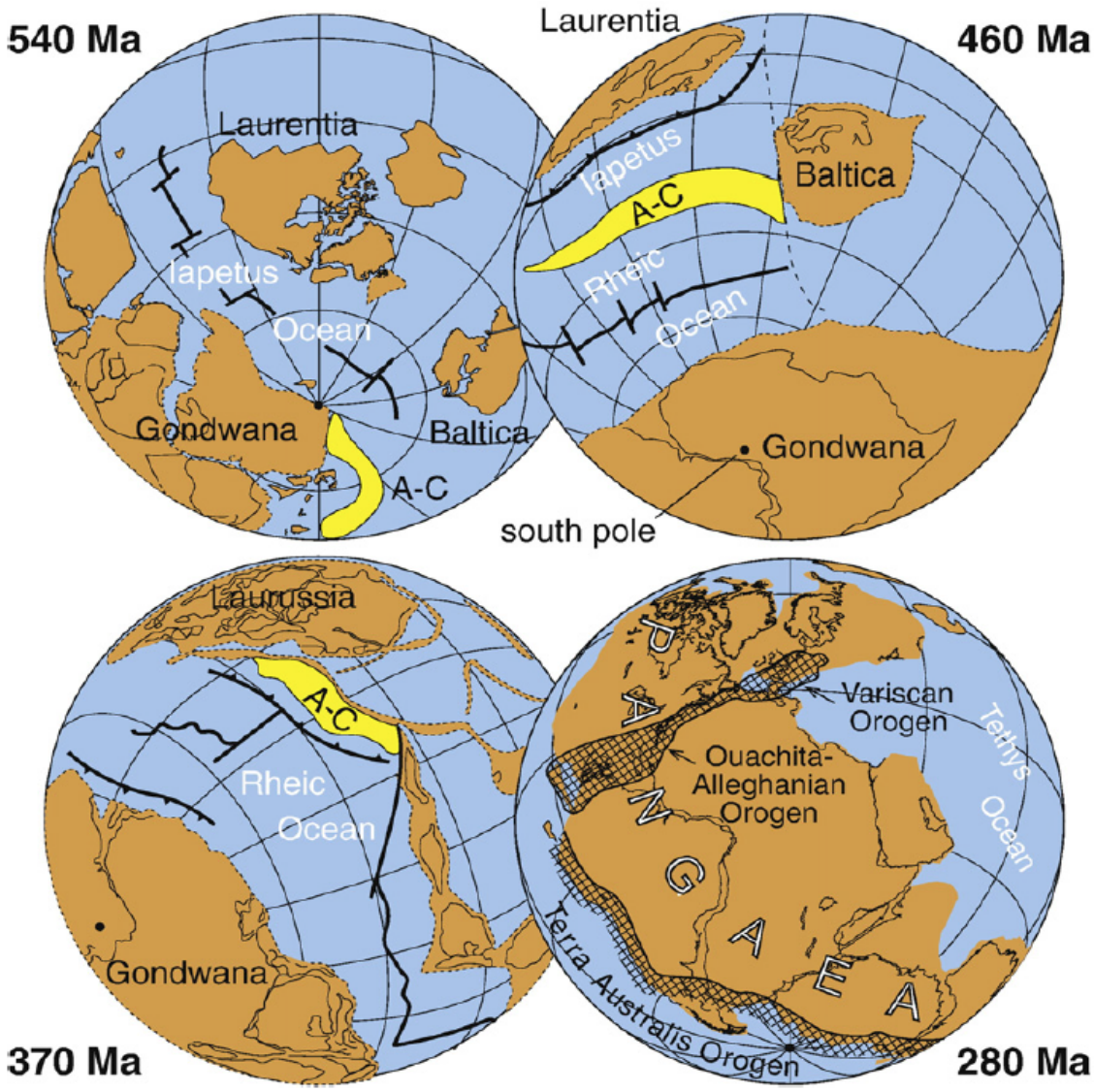

Figure 2: Paleozoic plate reconstructions highlighting the evolution of the Rheic ocean. At 540 Ma, the Iapetus ocean formed between Gondwana and Laurentia. By 460 Ma, Avalonia-Carolinia (A-C) had been separated from Gondwana, creating the Rheic Ocean. By 370 Ma, the Iapetus ocean closed during collision of Laurentia, Baltica, and Avalonia-Carolinia to form Laurussia. Lastly, the Rheic Ocean closed by 280 Ma creating the Ouachita-Alleghanian Orogen in North America and the Variscan Orogen in Europe. Map modified from Scotese, 1997.

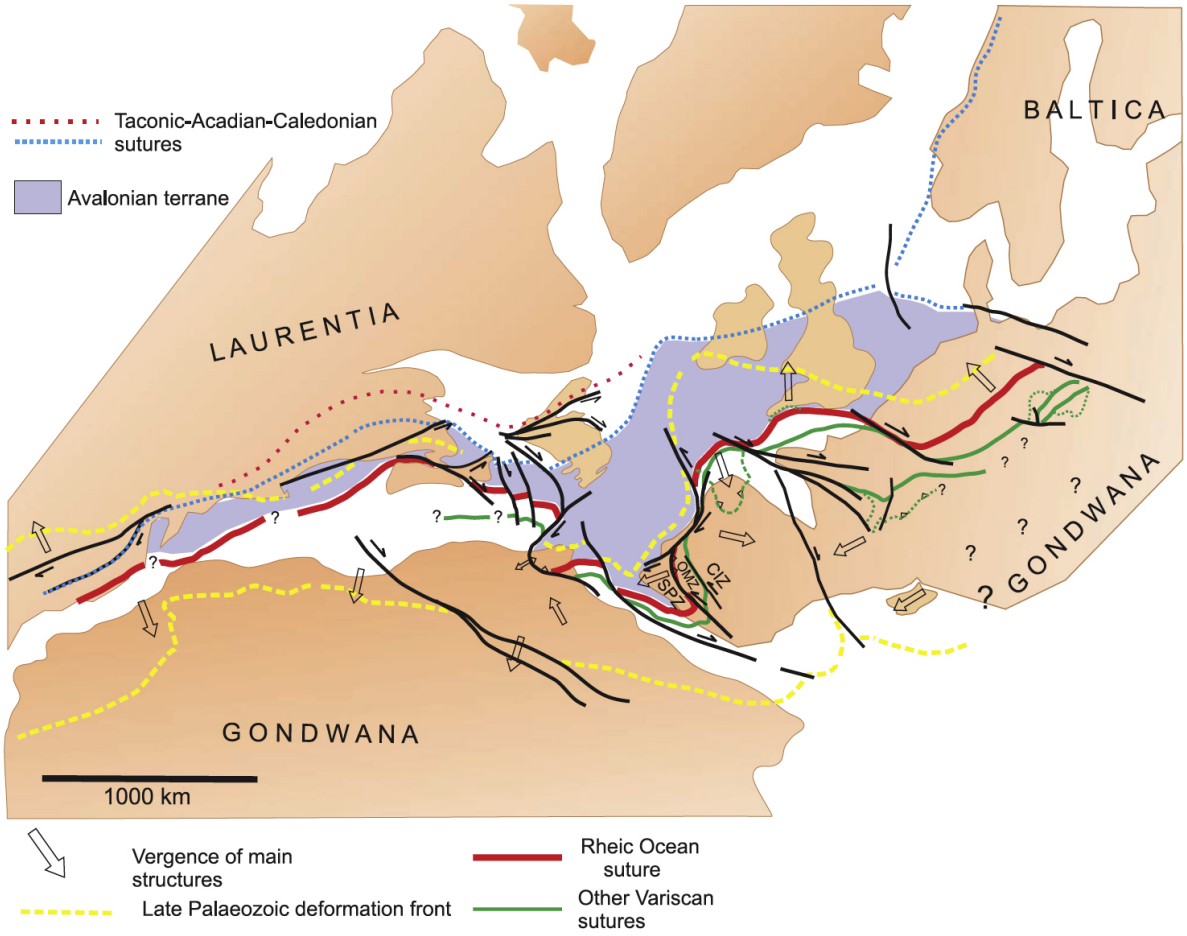

Figure 3: Tectonic reconstruction during the Carboniferous (~300 Ma) collision between Gondwana and Laurentia-Baltica. Together, the Central Iberia Zone (CIZ) and the Ossa Morena Zone (OMZ) in the Iberian Peninsula formed during passive margin sedimentation along the Rheic Ocean edge. During Rheic Ocean closure, the Southern Iberian Shear Zone formed at the tectonic boundary of the exotic terrane South Portuguese Zone (SPZ) and the OMZ. Map from Azor et al., 2008.

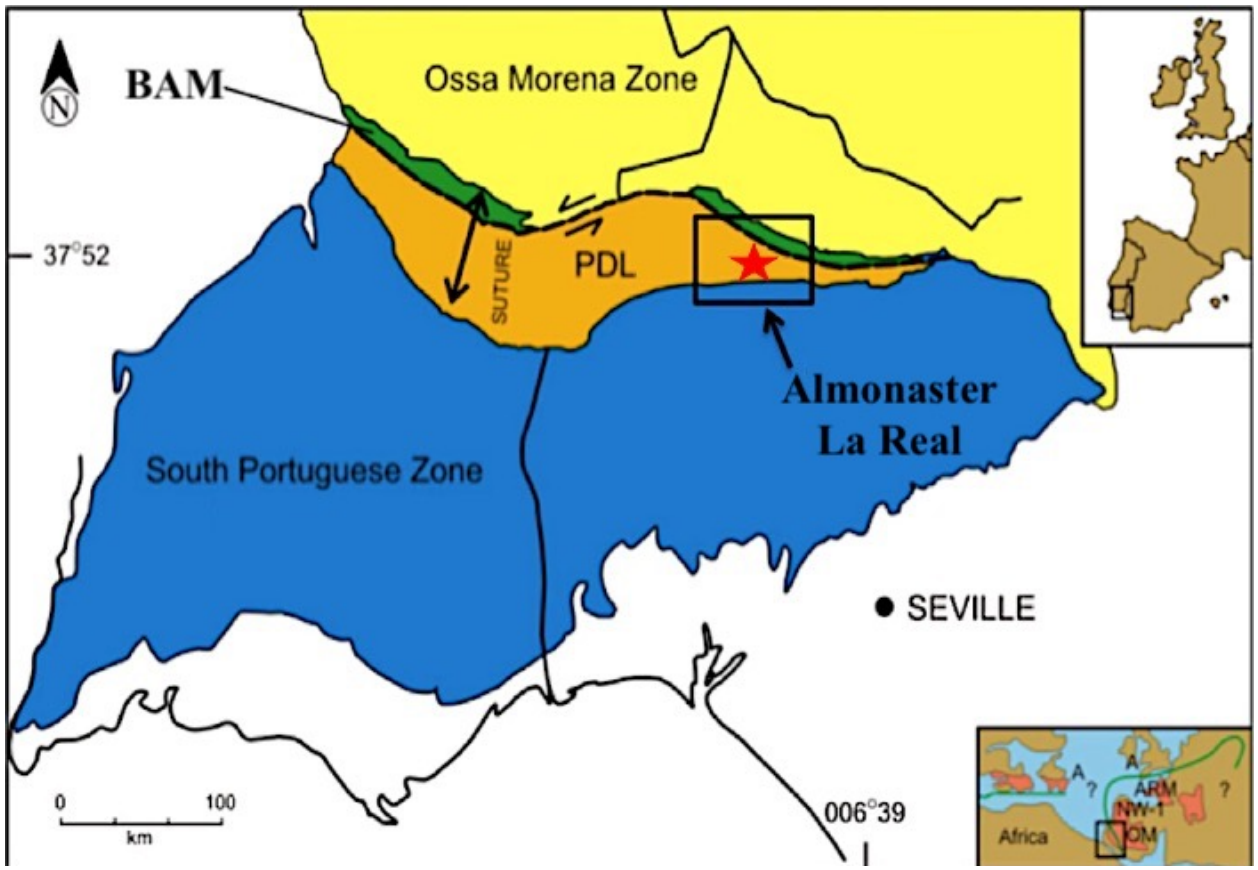

Figure 4: Map of tectonic subdivisions of Southern Iberia showing the Ossa-Morena Zone, South Portuguese Zone and the Variscan suture which consists of the Beja-Acebuches Metabasites (BAM) and the Pulo do Lobo accretionary prism (PDL). The SISZ is the suture between the BAM and the PdL. Modified from Dahn et al., 2014.

2.2 Geology of the SISZ

2.2.1 Ossa-Morena Zone (OMZ)

The Ossa Morena Zone (OMZ) is interpreted to be a composite terrane accreted to the Central Iberian Zone during the late Proterozoic Cadomian orogeny (Braid et al., 2010). It contains a diverse collection of Precambrian units that formed prior to accretion and Paleozoic units deposited unconformably over top. The Paleozoic sequence includes pre-orogenic and syn-orogenic successions.

2.2.2 Beja-Acebuches Metabasites (BAM)

The BAM has a MORB affinity based on geochemical analysis (Bard and Moine, 1979; Castro et al., 1996; Stephenson, 2018) and identification of an internal ophiolite sequence (Quesada et al., 1994). The metabasites have been interpreted as remnants of the major oceanic suture between the Iberian Massif and the South Portuguese exotic terrane (Bard and Moine, 1979; Castro et al., 1996), or more recently, with the addition of geochronology evidence, as remnants of a smaller rifted ocean basin formed during a transtensional event (Azor et al, 2008). According to this interpretation, the main continent-continent collision occurred slightly later.

During the prolonged deformation related to collision, the BAM endured a broad early high temperature/low pressure metamorphic and deformational event (e.g., Castro et al., 1996; Díaz-Azpiroz and Fernández, 2005). This event was followed by a localized deformation forming the SISZ, which produced mylonitic shear zone fabrics and retrograde greenschist – lower amphibolite metamorphism in the BAM (Crespo-Blanc and Orozco, 1988; Castro et al., 1996; Díaz Azpiroz and Fernández, 2003, 2005). The retrograde metamorphism was likely

related to uplift and exhumation of rocks during the ongoing collision (resulting in lower metamorphic grade at shallower crustal depths).

In the BAM, the metamorphic grade increases towards the top of the structure with the introduction of clinopyroxene and compositional banding of plagioclase and amphibole-rich layers. The four main rock types in the BAM from top of structure to bottom (contact with PdL at the SISZ) are coarse-grained banded amphibolites containing clinopyroxene (w/ cpx), medium-grained banded amphibolites without clinopyroxene (w/o cpx), folded and sheared amphibolites, and mafic chlorite schists (Castro et al., 1996; Díaz-Azpiroz and Fernández, 2005; Stephenson, 2018).

2.2.3 Pulo do Lobo Domain

A late Paleozoic complex, the Pulo do Lobo Domain, consists of fault-bounded tectonostratigraphic units that strike east-west and dip steeply to the north (Eden, 1991; Simancas et al., 2003; Braid et al., 2010). It most often is interpreted to represent an exposed accretionary prism and suture zone of the closure of the final stages of the Paleozoic Rheic Ocean and the merger of Gondwana and Laurussia (Eden 1991; Onézime et al., 2003), but recent detrital zircon data suggest its provenance is more complex (Braid et al., 2011). Many studies have focused on describing the internal tectonostratigraphic units, and there is some disagreement about divisions and nomenclature (Eden, 1991; Giese et al., 1999; Braid et al., 2010; Quesada et al., 2019). The Pulo do Lobo Domain consists of lower units sometimes described as mélange, including the basal Pulo do Lobo (PdL) Formation, comprised of interbedded metapelites and quartzites, unconformably overlain by flysch units consisting of siltstone and greywacke. The overall Pulo do Lobo Domain has an antiformal structure, but has been internally complexly deformed within

different mélange domains having been pervasively folded and thrusted at low grade metamorphic conditions (Crespo Blanc, 1989; Silva et al., 1990; Eden, 1991; Onézime et al., 2002; Braid et al., 2010). The focus of this project is the northern-most portion of the PdL, where it is in contact with the BAM (Fig. 6); it contains interbedded quartzites and metapelites (slates, phyllites, and mica schists). A second metamorphic event related to the SISZ forms locally along the boundary, typically described as retrograde event (e.g., Braid et al., 2010). Peak metamorphism in the PdL reached greenschist facies with temperatures of 400-450° C and pressure of 2 kbar pressure (Ábalos et al., 2002), although metamorphic grade and conditions of the PdL near the SISZ boundary has not been studied.

Nomenclature of and within the Pulo do Lobo Domain is problematic. Different internal divisions and names are used in Spain compared to Portugal, and even researchers within Spain use different terms (see for example Ábalos et al., 2002; Pereira et al., 2018; Quesada et al., 2019). Some researchers refer to the broad Pulo do Lobo regional sequence as the Pulo do Lobo Domain and others as the Pulo do Lobo Zone. Some consider it the northernmost portion of the South Portuguese Zone whereas others group it with the BAM as part of a small oceanic domain between the SPZ and the OMZ. For our purposes, we refer to the large regional unit as the Pulo do Lobo Domain to reflect that it is not a large zone like the SPZ, but instead is a small suture-related sequence of oceanic basin rocks including the PdL and BAM ophiolite sequence. Additionally, the parts of the Pulo do Lobo Domain that are called the Pulo do Lobo Formation vary by research group. For example, Quesada et al. (2019) refer to the PdL rocks at the boundary in Almonaster as "Alájar mélange," linking those rocks to rocks found at the boundary in Alájar. For this study we call the rocks at the SISZ boundary in Almonaster the PdL Formation for the following reasons. In Alájar, we observed metabasites interspersed with

metasedimentary rocks; while some interpret these as mélange relationships, we interpret them as thrust slices because they occur as small slivers parallel to foliation rather than fragmental blocks. In the metasedimentary rocks of the Almonaster outcrop, we observed continuous bedding. There are no such slices of metabasites and no evidence of fragmental geometries, so we choose to use the term PdL Formation.

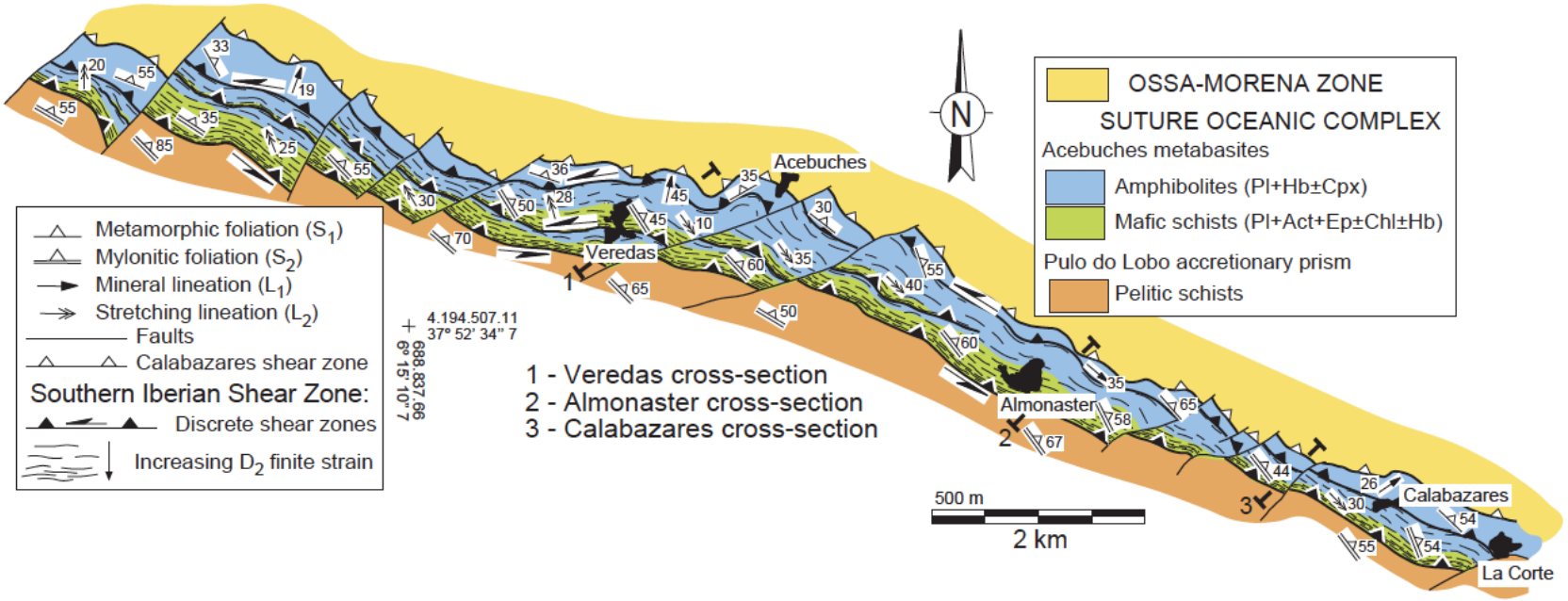

Figure 5: Map of the central portion of the SISZ showing the Beja-Acebuches Metabasites (blue and green colors showing amphibolite and mafic schists of BAM respectively) in shear contact with the Pulo do Lobo metasedimentary rocks (metapelites with interbedded quartzites) (orange). Modified from Díaz-Azpiroz and Fernández (2005).

2.3 Structural framework of the SISZ and fluid flow

The SISZ is located in southwestern Spain through the towns of Aracena and Aroche. It is 50km in length and is 300-500m wide. It strikes 115° on average and dips around 50° to the NNE; although it flattens at depth, resulting in a more listric geometry (Figure 6). The SISZ follows the contact between the BAM and PdL Formation.

Following earlier metamorphic and deformation events in the BAM (high temperature/low pressure) and PdL (low grade folding) related to early stages of the collision, a localization of deformation formed the SISZ that formed mylonitic shear fabrics in the BAM and locally near the boundary in the PdL pelitic schists (Crespo-Blanc and Orozco 1988; Diaz-Azpiroz and Fernandez 2005).

Within the BAM, the first deformation event of high temperature/low pressure (recording peak conditions near the transition between amphibolite and granulite facies) is well-preserved in the coarse-grained banded amphibolites (w/ cpx) and medium-grained banded amphibolites (w/o cpx). Two sets of subparallel foliations oriented NW-SE and dipping steeply NE are formed by banded layering and preferred orientation of amphibole crystals. The amphibole crystals further define the lineations with a high pitch and NE-E plunge (Díaz-Azpiroz and Fernández, 2005; Stephenson, 2018). The transition to the second deformation event of retrograde metamorphism occurs gradually towards the SISZ, first evident by folds within the sheared amphibolites that become increasingly more tight to isoclinal towards the SISZ. Retrograde metamorphism within the BAM produced mylonitic shear fabrics similarly oriented at 115° and dipping 50° NNE with variable lineation orientations formed by elongation of plagioclase aggregates (Díaz-Azpiroz and Fernández, 2005; Stephenson, 2018). Asymmetric shear sense indicators including sheath folds, winged porphyroclasts, and S-C-C’ structures mostly suggest a sinistral sense of displacement

(Díaz-Azpiroz and Fernández, 2005). Based on detailed structural analysis and kinematic modeling within the BAM, the SISZ deformed in sinistral transpression with variable oblique extrusion (Díaz-Azpiroz and Fernández 2005; Fernández et al, 2013).

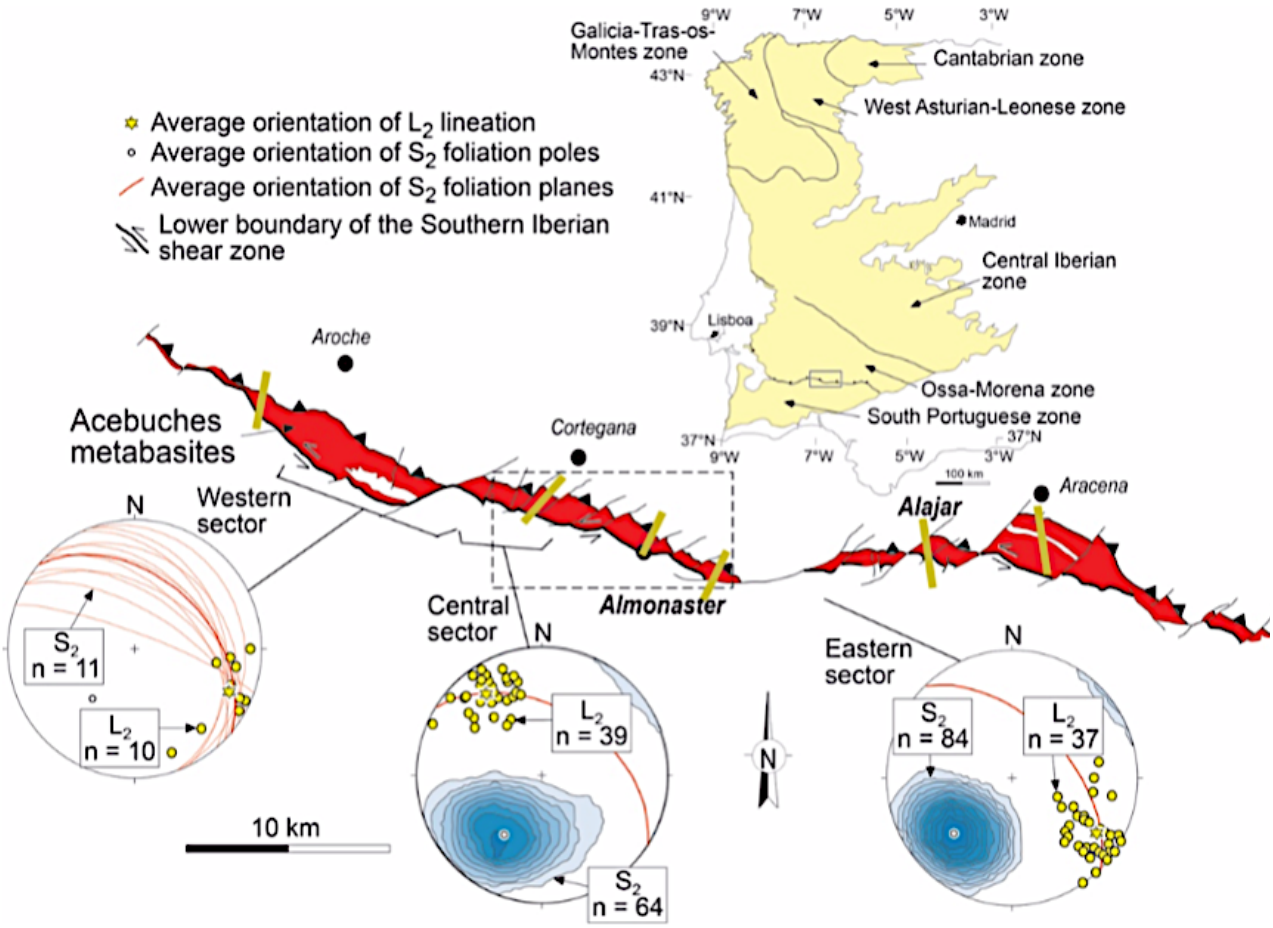

Figure 6: Map of the Iberian massif with the Ossa Morena Zone and South Portuguese Zone indicating the location of the SISZ along their boundary, depicted in the main map below. The main map shows structural data within the BAM along the SISZ. The box on the main map shows the area in Figure 3. From Fernández et al., 2013.

Previous work in the BAM assessed major element geochemical changes using X-Ray Fluorescence (XRF) as a function of distance to the SISZ (Stephenson, 2018; Czeck et al., 2019). Results indicate enrichment in K_2O, CaO, and Al_2O_3 and depletion in SiO_2 with strain and alteration towards the shear zone (Stephenson, 2018). The Al_2O_3 and CaO enrichments and SiO_2 depletion mostly occurred closer to the SISZ where epidote, actinolite, and chlorite were present, suggesting that these elements were contained within their crystal structure. Both minerals required addition of water to the hornblende found further from the SISZ, so the hydrothermal fluid facilitated both the mineral growth and resultant rock weakening (Stephenson, 2018). The mobile element K_2O is not usually enriched in MORB-derived rocks, so it likely that syndeformational fluid moved potassium across the shear zone from the PdL to the BAM, likely being incorporated into the amphibole structures (Stephenson, 2018).

The structural geometry of the PdL related to the SISZ is less well known and its internal strain localization has not been previously been studied. Further, it is unclear why the SISZ is presumably more strongly localized within the PdL, with previous descriptions suggesting it extends only about 50 m away from the boundary into the PdL, in comparison to 300-500 m wide into the BAM (Díaz-Azpiroz & Fernández, 2005).

CHAPTER 3: Methods

3.1 Field Work

I traveled to southwestern Spain from January 8 to January 24, 2020 to collect data in the Pulo do Lobo Formation in Almonaster la Real with research team members Carlos Fernández (Universidad de Huelva), Manuel Díaz-Azpiroz (Universidad Pablo de Olavide), and Dyanna Czeck. Almonaster la Real has a complete transect of the PdL within the village along Road of the Escalada which runs along Rivera de Almonaster. We also observed rocks along the HV-1201 road in Almonaster la Real and a transect in Alájar; some data from those transects are included in the Appendices, but do not comprise a significant part of this work.

In the field, we characterized lithological variations and intensity of deformation fabrics. The shear zone was identified by the contact between the BAM and the PdL, known within approximately 10 meters due to exposure. We placed the contact immediately to the southwest of the last BAM outcrop before the PdL. We made detailed observations of lithology and structures for approximately 1000 m along the road which travels southwest nearly perpendicular to strike (Figure 7a). Structural features including foliation, lineation, shear bands, asymmetric features, and folds were noted when present.

My goal was to sample across the strain gradient, beginning from the shear contact between the PdL and the BAM and ending outside rocks affected by the SISZ. Samples were spaced approximately 10-20 meters apart. At each sampling station, we took samples of each lithology found, typically a paired quartzite and metapelite found in adjacent layers. A total of 39 oriented samples were collected across this transect for microstructural analysis (Figure 7b).

a

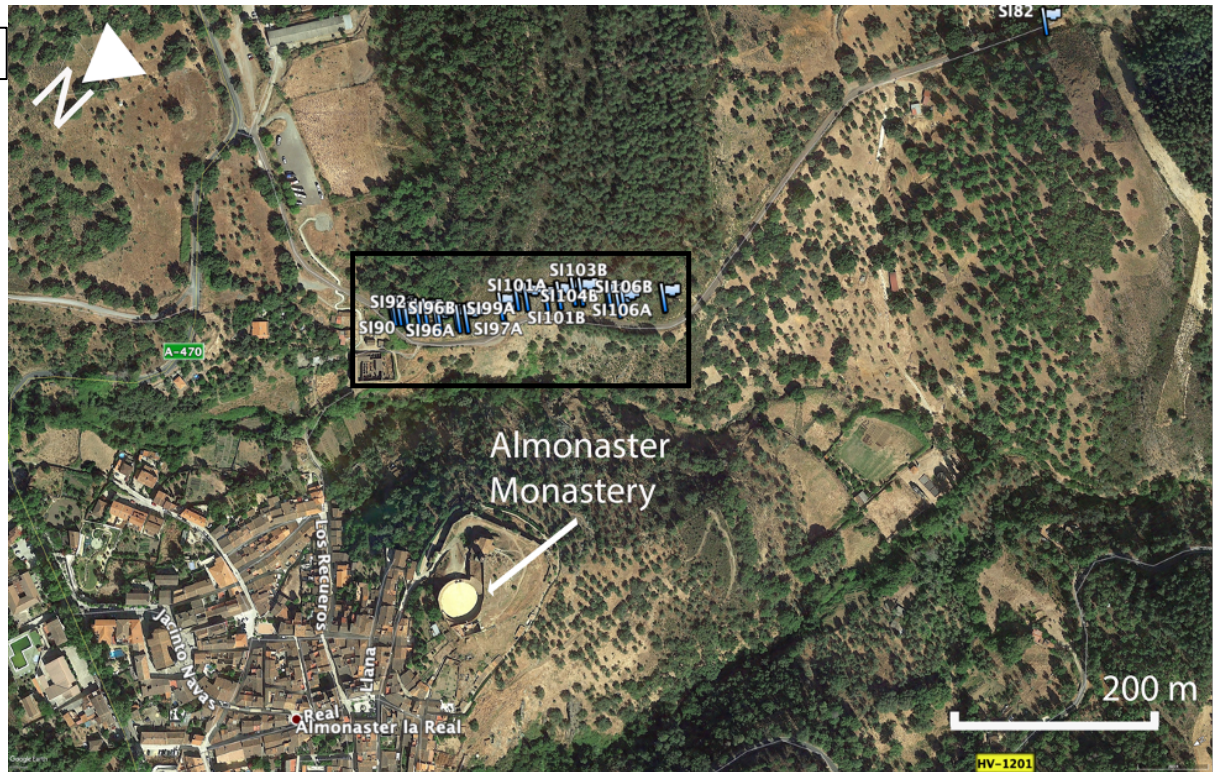

b

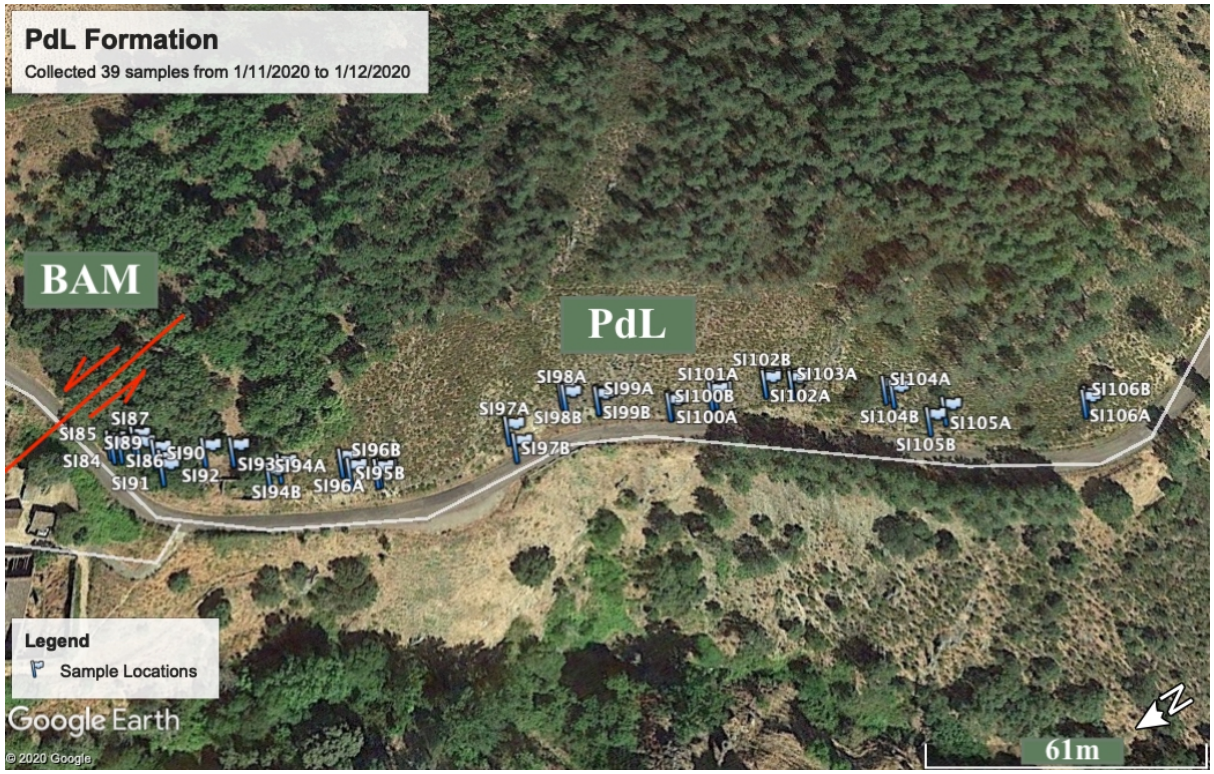

Figure 7: (a) Locations of study locations in Almonaster la Real shown on Google Earth image (b) Closer view of most of the study locations with SISZ shear zone contact shown in red, which divides outcrops of BAM from PdL. GPS locations given in Chapter 9 Appendix 9.1.1.

Since we acquired samples along roadways that cut obliquely across structure, we needed to do a series of calculations to transform roadside distance (D_m) to the distance from the structural top of the Pulo do Lobo at the SISZ contact (d). As described in Stephenson 2018, at each sample location we noted the distance from the previous location using a tape measure along the roadside (d_m), the road azimuth measurement (μ), the azimuth (α) and the dip (β) of the foliation. The angle (η) between the road azimuth (μ) and the normal to foliation (ν) is determined (Eq. 1). We then multiplied the horizontal distance along the road (d_m) times the cosine of η to find the horizontal distance between samples perpendicular to the foliation (d_h) (Eq. 2). To find the true distance between samples perpendicular to foliation (d), d_h is multiplied by the sine of the foliation dip (β) (Eq. 3, see Appendix 9.1.1 Field Data).

(1) $\eta = 180 - (\mu - \nu)$; {if $\mu > 180°$}

$\eta = (\mu - \nu)$; {if $\mu \neq> 180°$}

(2) $d_h = d_m \cos\eta$

(3) $d = d_h \sin\beta$

3.2 Qualitative Determination of Strain

Like most deformed rocks, the PdL lacks strain markers such as deformed pebbles, fossils, or grain shapes that can be used to quantify finite strain, so we will use qualitative deformation fabrics within the rocks as a proxy for strain magnitude (e.g., Marquer et al., 1996; Carreras et al., 2010). Criteria used to discern strength of fabrics were type (slaty, phyllitic, schistose) and spacing of foliations at the meter to decameter scale. We interpreted closely spaced schistose foliation to be a strong fabric formed in high strain and distantly spaced slaty

cleavage to be a weaker fabric formed in low strain. At the cm-m scale, fabric strength is controlled by rheology contrasts and development of anastomosing shear strands of high strain zones surrounding lozenge-shaped lesser deformed rocks (Figure 8; Marquer et al., 1996; Carreras et al., 2010; Ponce et al., 2010).

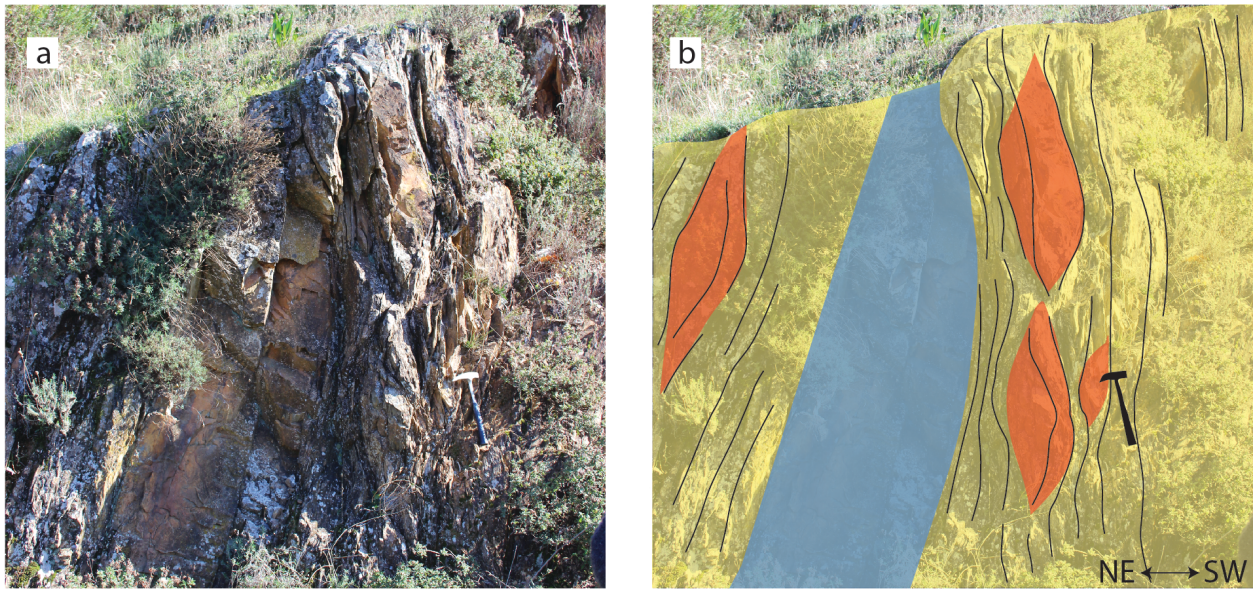

Figure 8: Example of a lozenges (lesser deformed) surrounded by more highly deformed shear bands in PdL at Almonaster la Real. a) Field photograph b) Annotated photo with thin black lines indicating trace of foliations planes; strong undeformed quartzite layer (blue) and semi-strong quartzitic phyllite layers (orange) surrounded by highly deformed weak phyllite layers. Hammer for scale. From Czeck (2020, unpublished).

Based on the m-dm scale observations, we divided outcrops into 3 strain groupings which are color-coded on subsequent graphs: red is high strain (close to the shear zone with primarily schistose fabrics), yellow is intermediate strain (with phyllitic fabrics), and green is low strain (furthest away from the shear zone with slaty cleavage).

3.3 Microstructural Analysis

Active deformation mechanism(s) depends on a variety of factors including type of mineral, grain size, temperature, pressure, stress, strain rate, and presence/composition of a fluid. Several processes may occur simultaneously in the same or coexisting minerals. The dominant processes may vary over space and time. Each has a characteristic array of microstructures. The goals of the microstructural analysis are to: 1) document the mechanisms responsible for the deformation, 2) determine whether they vary with strain accumulation or distance from the shear zone, and 3) interpret the presence of fluids during deformation.

Numerous experiments and natural observations from rocks and minerals that have undergone ductile deformation identify two major groups of deformation mechanisms: crystal-plasticity and diffusional processes.

Crystal-plasticity is caused by the movement of linear defects called dislocations through the lattice during deformation (Vernon, 2004). Microstructural evidence for crystal plasticity includes undulose extinction, subgrains, kink bands, bent crystal shapes, deformation lamellae, and deformation twins (Figure 9). Microstructural evidence of recovery mechanisms includes recrystallization and triple junctions, which are indicative of an advanced stage of crystal plasticity (Figure 10).

Diffusional processes may occur within grains or across many grains, with or without a fluid present. Widespread diffusion requires a fluid and may allow mass transport of soluble elements, known as diffusive mass transfer (DMT). Microstructural evidence of diffusion includes indented grains, overgrowths, selvage seams, and strain shadows around competent grains (Figure 11; Vernon, 2004). Brittle deformation includes processes of fracturing, crushing, and frictional sliding of grains or rock fragments.

Rocks that are ductile at the m scale may have evidence for brittle deformation at the microscopic scale, either in minerals that are stronger than surrounding minerals (example strong plagioclase grain surrounded by relatively weak quartz) or intermittently when deformation conditions change. Microstructural evidence for brittle deformation is that of intragranular fractures, intergranular fractures, veins, and boudinaged grains (Figure 12).

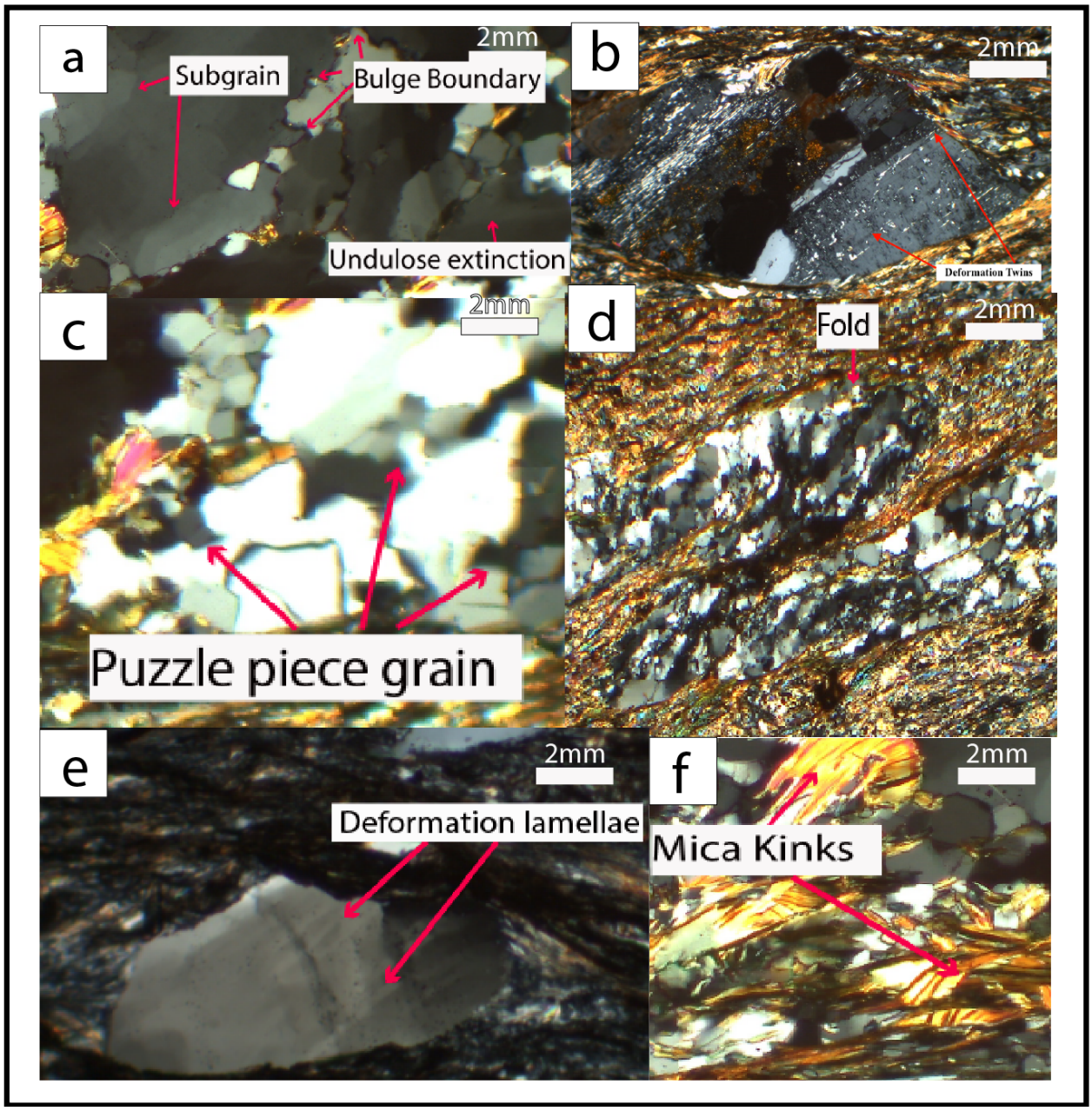

Figure 9: Crystal plasticity microstructures in SI-83-100P such as a) subgrains, bulge boundaries, undulose extinction, (b) deformation twins, (c)puzzle piece grains, (d)folds, (e)deformation lamellae, and (f) mica kinks.

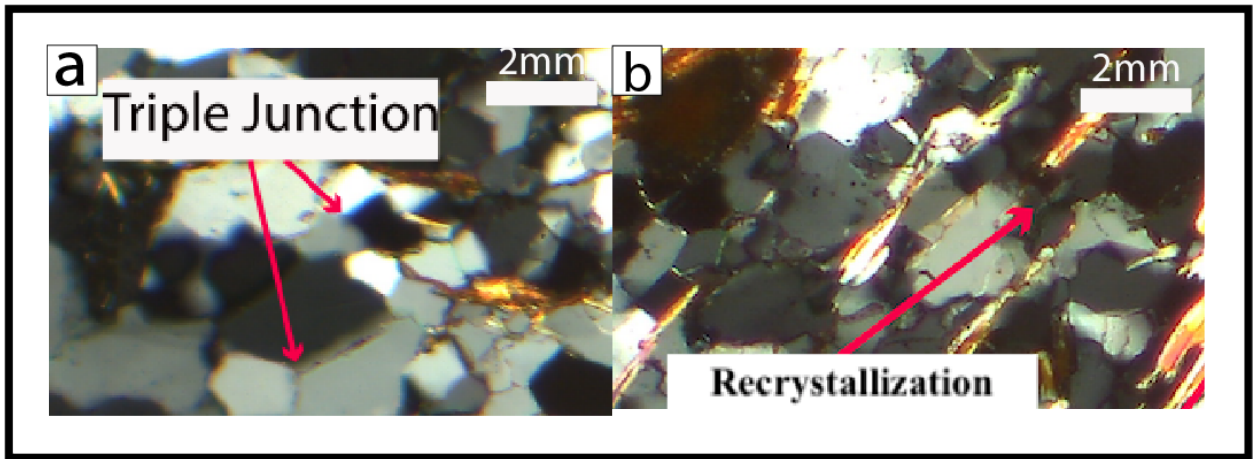

Figure 10: Recovery microstructures in SI-83 such as (a) triple junctions and (b) recrystallization.

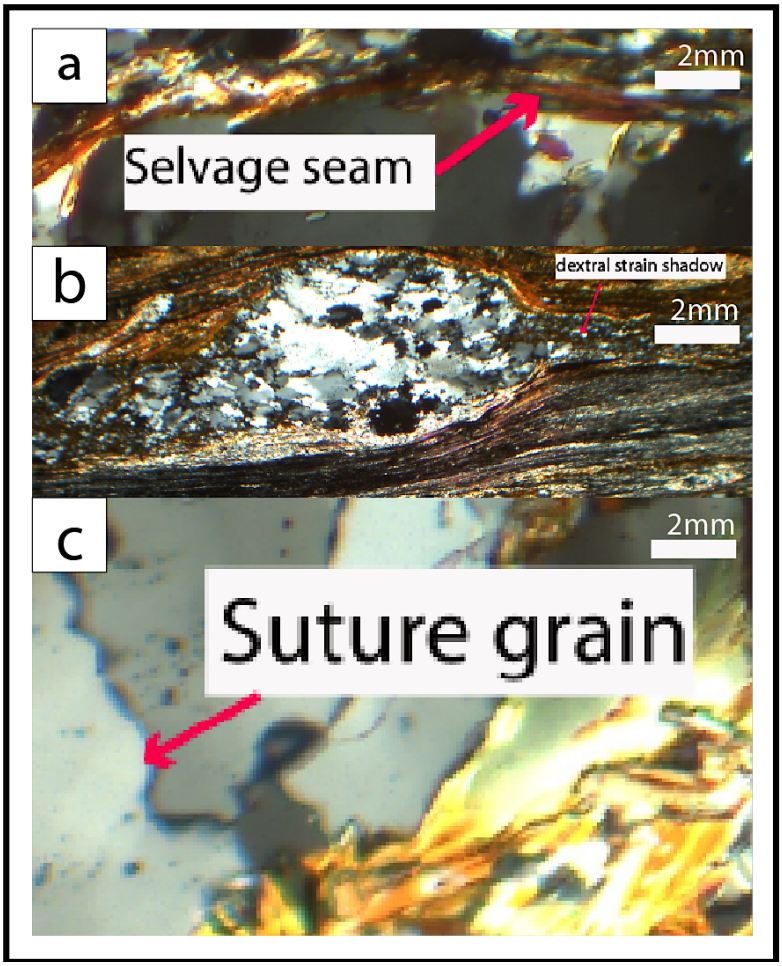

Figure 11: DMT microstructures in SI-83 and SI-94P such as (a)selvage seams, (b) dextral strain shadows, and (c) sutured grains.

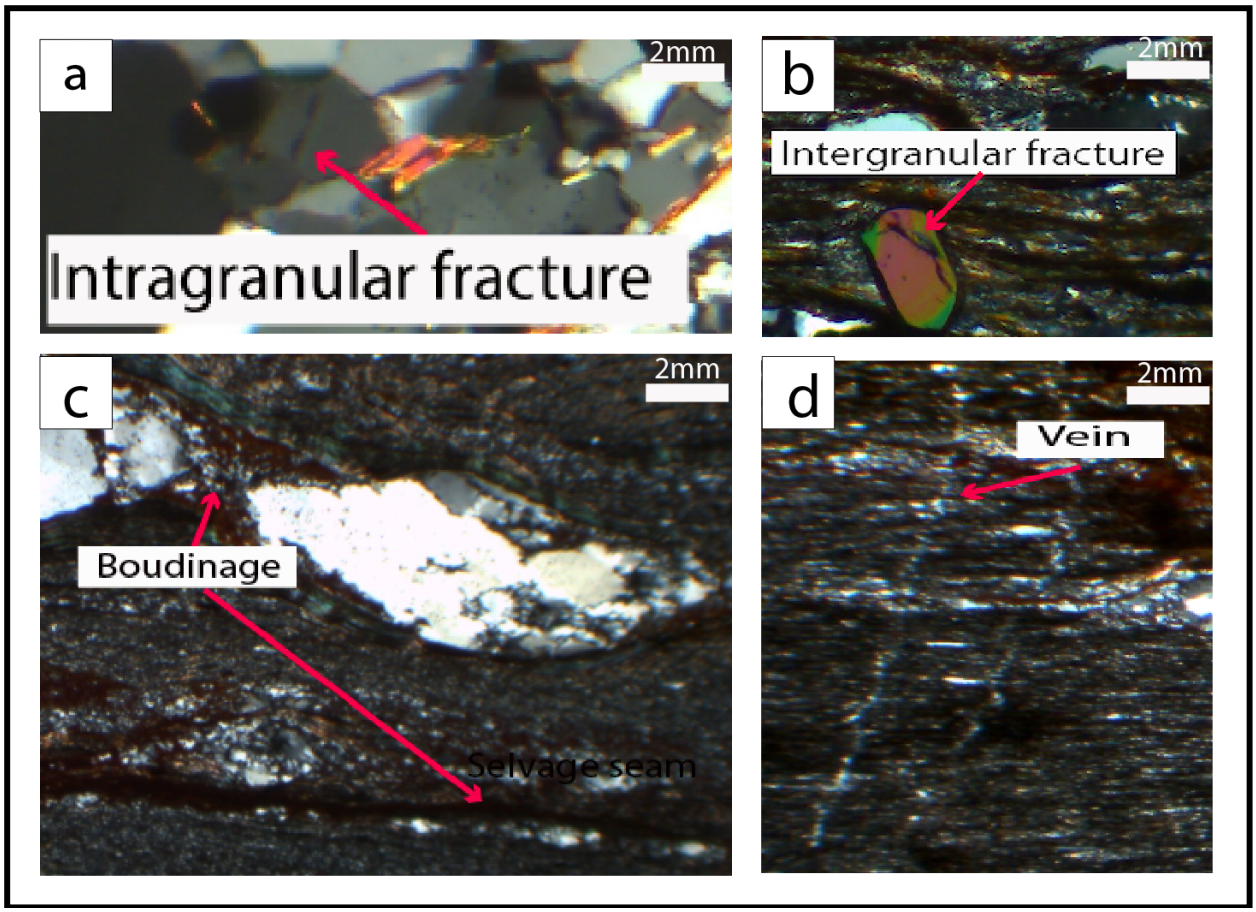

Figure 12: Brittle microstructures in SI-83, SI-101P and SI-105P such as (a)intragranular fractures, (b) intergranular fractures, (c)boudinage, and (d) veins.

Rock samples were cut into oriented billets at the University Pablo de Olavide in Seville, Spain. Of the 39 samples that were collected, 28 billets were prepared for microstructural analysis. Billets were cut parallel to the XZ-plane of strain (perpendicular to foliation and parallel to lineation) with the long axis of the billet cut parallel to lineation. All samples had visible foliation; however, not all had visible lineation. For those with visible lineation, billets were cut using the visible foliation and lineation. For those without visible lineation, billets were cut using the sample foliation and the most common SISZ lineation in the PdL, determined to be down dip of foliation.

A petrographic and microstructural qualitative analysis was completed on the 28 oriented thin sections in which primary mineralogy and microstructures were recorded (e.g., Figure 13). Foliation style (slaty, phyllitic, and schistose) was noted and used to corroborate groupings of low, intermediate, and high strain sites determined in the field.

A quantitative microstructural analysis was conducted on 9 of those thin sections, 3 selected from each of "low," "medium," and "high" strain areas determined in the field and qualitative thin section analysis. Metapelitic samples were the focus of this quantitative analysis because they have the most clear evidence of metamorphic changes across the strain gradient. The quantitative microstructural analysis consisted of point counting minerals and microstructures at 200 points along a grid (Table 1).

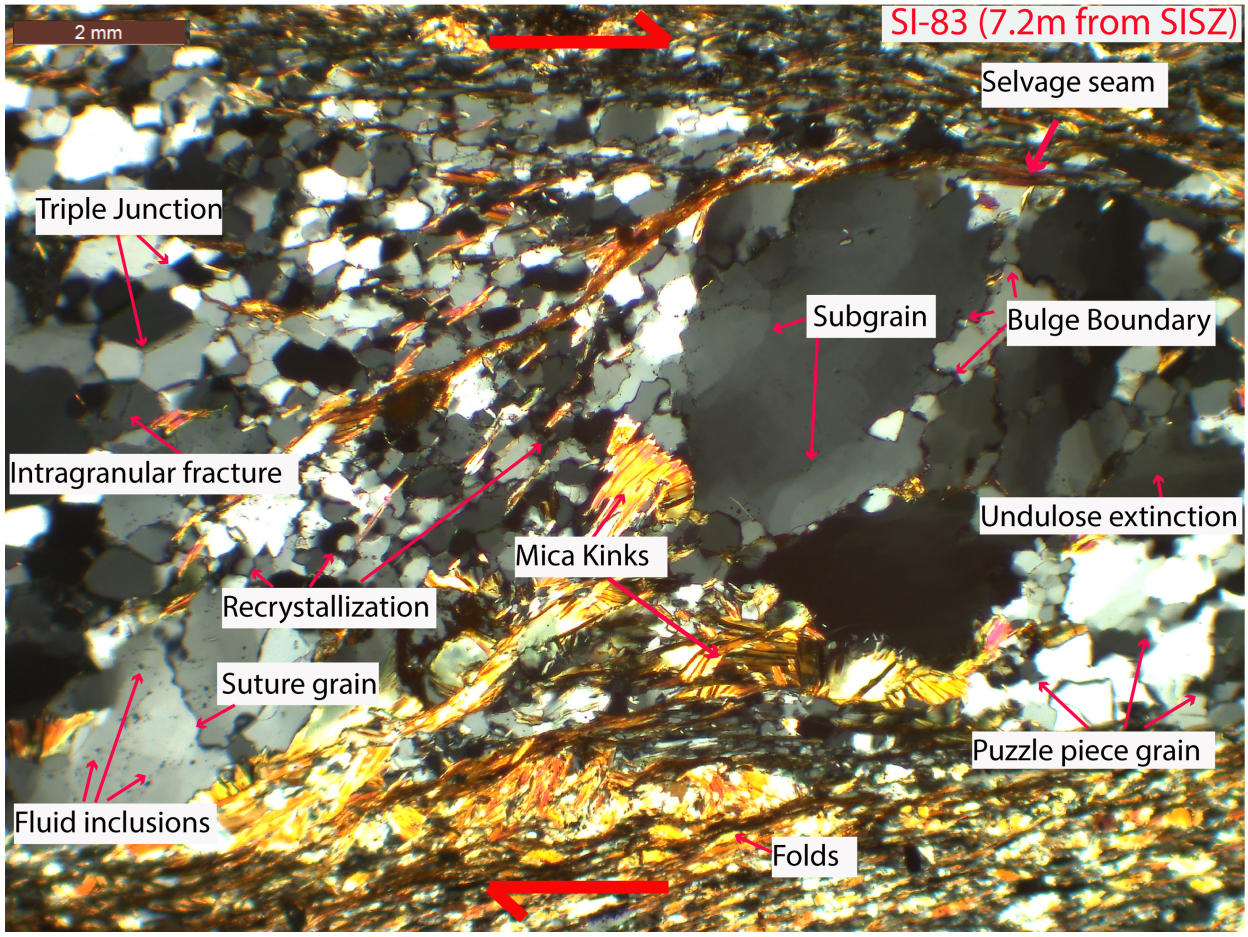

Figure 13: Representative microstructures in SI-83 seen throughout the other thin sections in the PdL.

Table 1: Microstructures recorded in thin section analysis

Brittle	**DMT**	**Crystal Plasticity**	**Crystal Plasticity Recovery**
Intergranular Fractures	Selvage Seams	Undulose extinction	Recrystallization
Intragranular Fractures	Sutured Grains	Subgrains	Triple junctions
Veins	Strain shadows	Puzzle piece grain boundaries	
Fluid inclusion trails		Bulged grain boundaries	
Boudinaged grains		Deformation lamellae	
		Quartz Ribbons	
		Folds	
		Deformation twinning	

The software program PetrogLite was used to automate the point counting to a specified grid to avoid bias (Figure 14). This program uses an automated stage to move to points on the thin section, and the petrographic microscope was used to manually observe mineralogy and microstructures which were recorded on a spreadsheet. These quantitative data are used to find the percentage of each type of grain that contains each microstructure. Microstructures were then separated into deformation mechanism categories of brittle, DMT, and crystal-plasticity. Percentage data are plotted with respect to shear zone distance and reported in Section 4.2.

a

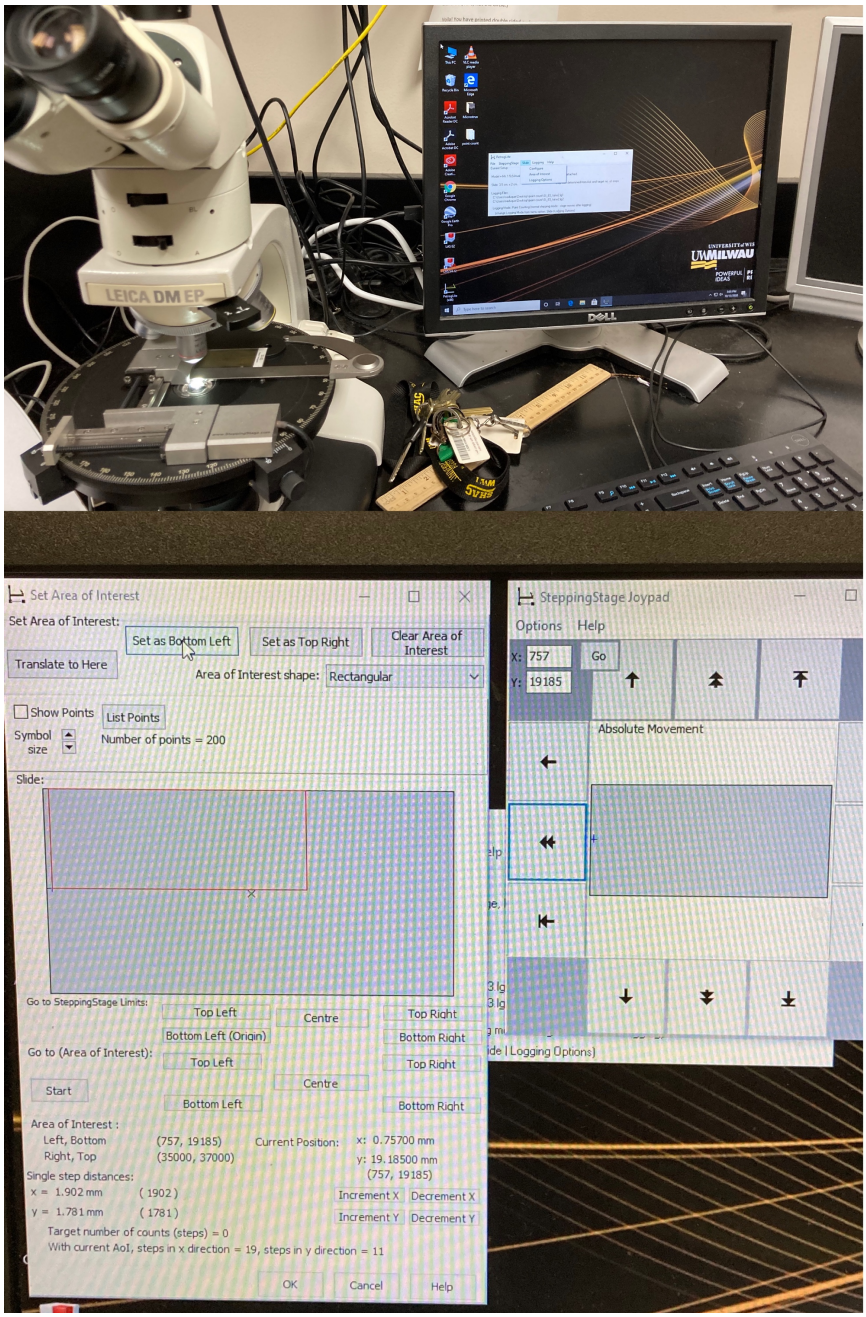

b

Figure 14: (a) Setup of the step-stage and Leica DM EP petrographic microscope, (b) using the PetrogLite software to do the point count analysis

3.4 X-Ray Methods

3.4.1 X-Ray Diffraction (XRD)

A Bruker D8 X-Ray Diffractometer was used to qualitatively determine the mineral assemblages for the 2020 sample (SI-82) from Almonaster (methods of McHenry et al., 2017). The other fifteen samples from Almonaster y La Escalada and Alajar were analyzed (Table 10), but will not be included for this discussion.

The powdered sample was poured into a cavity mount and the surface was gently smoothed. Each sample was analyzed using a Cu tube, operating at 40kV and 40mA, with a scintillation detector and divergence slit of 0.6°. The 2θ angle range was from 2° to 60° with a 1 second step size of 0.02° and a total of 2900 steps. The resulting diffraction patterns were compared against ICDD PDF-2 to identify the minerals present.

3.4.2 X-Ray Fluorescence (XRF) Analysis

Twenty-one samples across the strain gradient in Almonaster la Real were analyzed for major element concentrations using X-Ray Fluorescence (XRF). Of these, the 2018 research team collected twenty (Stephenson, Czeck, Díaz-Azpiroz, Fernández), and I helped collect the other one in 2020. In 2020, we collected an additional eight and seven samples from the Alajar and Almonaster la Real y La Escalada (along road HV1201) transects respectively. These data are included in the appendix, but not considered here in the discussion because they seem to have different initial (unaltered) chemistry compared to the Almonaster la Real transect.

Samples from 2018 were crushed by hand. Samples from 2020 were crushed using the Vibratory Disc Mill RS100 at the University of Huelva in Spain. Gritty samples were powdered using Dr. Lindsay McHenry's Rocklabs shatterbox. The powdered samples were placed in glass

vials and dried in a low temperature oven (105°C) overnight. A subsample of each dried powder was then used to calculate Loss on Ignition (LOI).

To calculate LOI, we placed four crucibles in the high temperature oven (1050°C) for 5 minutes to burn off any residual material. Then the crucibles were removed and placed in the desiccator for 5 minutes to cool. Each of the crucibles was weighed, and 1g of each sample was added. The measurement for the weight of the samples and samples with the crucibles was recorded. Each of the crucibles with the samples was placed in the high temperature oven for 15 minutes. Then, each of the crucibles was placed in the desiccator to cool for 5 minutes. The sample and crucible were then weighed and recorded. The weight of the sample and crucible after heating was subtracted by the weight of the sample and crucible before heating to calculate the mass lost. This mass lost was then divided by the original mass of the sample in the crucible and multiplied by 100 to get an LOI percentage. That LOI percentage was entered into the XRF machine before analysis of the disks, to help correct for dilution.

One gram (+/- 0.003 g) of each dried, powdered rock sample was mixed with ~1 g of ammonium nitrate, and 10 g (+/- 0.003 g) of Claisse 50:50 LiT:LiM flux with an integrated LiBr non-wetting agent. The mixture was transferred to a platinum crucible and fused at ~1050°C for 21 minutes using a Claisse M4 fluxer (methods of Byers et al., 2016).

Major and minor element concentrations were determined by XRF, measured using the Bruker S4 Pioneer WD-XRF spectrometer at the Department of Geosciences at the University of Wisconsin-Milwaukee. These were compared against a calibration based on eleven USGS igneous and sedimentary rock standards that were prepared the same way, described by McHenry (2009) and Byers et al. (2016). For data processing and reporting data, standards were applied through statistical error and lower limit of detection (LLD) analysis. These standards to

the geochemical data were as follows: (1) if the statistical error for the major element values was greater than 2%, then they would be listed as Not Detected (ND) and (2) if the calculated concentration was not at least two times the LLD, then they would also be listed as ND. None of the data failed the above standards, and thus no major elements were listed as ND in this study.

Three different types of plots are used to interpret the data: 1) Harker diagrams, 2) geochemistry vs. distance from the shear zone, and 3) isocon plots. The objective of the Harker diagrams is to display variations in major or minor oxide concentrations with respect to SiO_2. In this case, Harker diagrams plotted from the 2018 samples were used to discriminate samples to use for further plotting and analysis. Samples plotted in three distinct groups: high, intermediate, and low silica. For further analysis, we chose to evaluate the intermediate group as these samples are most likely to show evidence of chemical variation in the PdL with regards to strain. The low silica group are most likely contaminated with the BAM rocks, which can be found as small thrust slices within the PdL in some places. The high silica group consists of quartzites, which limits the possibility of much chemical variation as they are almost entirely SiO_2.

The second set of plots are used to demonstrate major element changes with distance from the SISZ. Major element compositions of intermediate silica samples were plotted versus distance from the shear zone boundary and color coded by qualitative strain determined from field observations and petrography, where high strain is denoted as red (close to the shear zone), intermediate strain is denoted as yellow, and low strain (furthest away from the shear zone) is denoted as green. This visualization allows interpretation of changes in chemistry with strain and metamorphic patterns within the PdL along the SISZ.

Isocon plots are commonly used for comparison between altered samples and their unaltered protolith to see which elements were enriched (gained) or depleted (lost) during

alteration (Webb and Golding, 1998). Plotting shear zone samples compared to their protoliths can help reveal the effects of fluid interaction in shear zones (O'Hara, 1990; Newman and Mitra, 1993; Yonkee et al., 2013: Stephenson, 2018). Two potential protoliths were chosen to compare to altered samples from the intermediate silica group. First, the intermediate samples were compared to the unaltered protolith that was furthest away from shear zone (PL 18). For the second method, we took the average of three samples collected far from the shear zone as the designated protolith (PL 15-18). For these isocon plots, mass-balance calculations were not considered, and we assumed a 1:1 slope. This approach was reasonable because elements generally considered immobile such as Al_2O_3 and TiO_2 plot along the 1:1 line, so an adjustment to the 1:1 line using the method of Grant (1986) was not necessary. Further justification for this approach is the relatively constant concentration of SiO_2 in PdL samples, because SiO_2 depletion is often key evidence for volume loss in shear zones (O'Hara, 1990; Newman and Mitra, 1993; Yonkee et al., 2013). The weight percent of each element was arbitrarily adjusted so that all major elements fit on the plot without overlap (Mukherjee et al., 2008).

3.5 Vorticity Analysis

Using the subset of nine thin sections selected for further analysis, kinematic vorticity numbers were estimated from the angle between C and C' shear band structures based on one of the methods outlined in Kurz and Northrup (2008).

Kinematic vorticity is internal rotation during deformation. We use a normalized dimensionless kinematic vorticity number, W_n, such that simple shear has $W_n = 1$ and pure shear has $W_n = 0$ regardless of strain magnitude (Means et al., 1980; Bobyarchick, 1986). If plate motion stays constant, kinematic vorticity must vary if the shear zone boundary is curved (e.g.,

Giorgis et al., 2017). Additionally, when strain magnitude partitions, high strain zones are often simple shear dominated and low strain zones are often pure shear dominated (Jones and Tanner, 1995; Zhang et al., 2009).

Within shear zones, schistosity planes (S-planes) are caused by the alignment of micas or platy minerals; S planes are initially parallel to the XY plane of the strain ellipse (containing the maximum and intermediate principal finite strain axes). S planes gradually rotate towards the shear zone boundary, forming C-planes (Figure 15). With the formation of C planes, new S planes may form. The acute angle between C and S planes allows the shear sense to be determined (Berthé et al., 1979; Lister and Snoke, 1984; Xypolias, 2010).

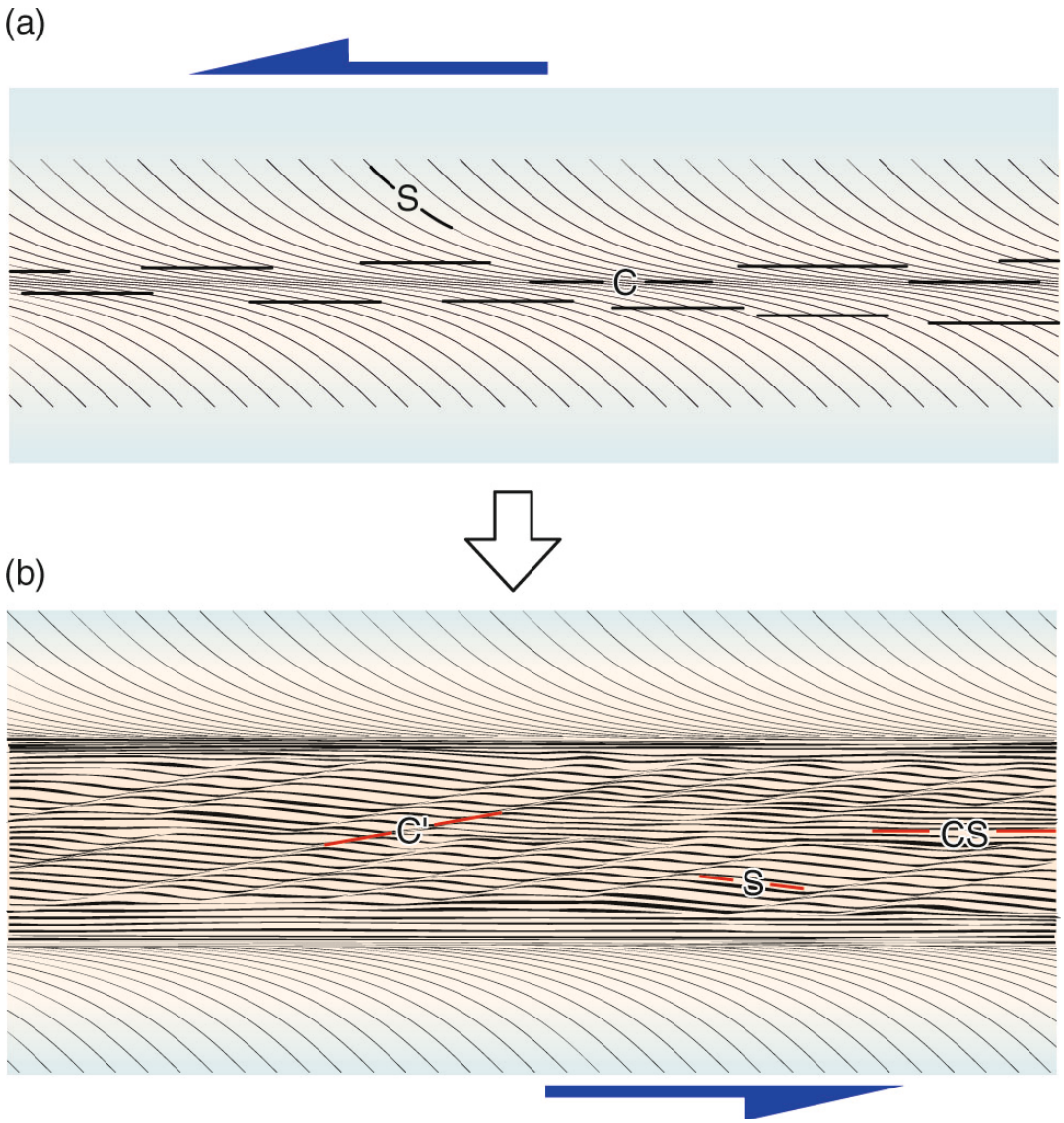

Figure 15: Illustration of S-C structure and synthetic oblique C' shear bands. (a) Early stages of S-C fabrics prior to C' initiation. (b) Later stages of fabric development when original S planes have rotated into parallelism with C planes, new S planes formed, and synthetic C' planes originate. From Fossen (2016).

The angle between C' and the C planes is used to determine the vorticity using the following equation:

$$W_n = \cos\alpha \qquad (4)$$

According to Kurz and Northrup (2008), C' planes are metastable, but likely rotate towards the shear zone so therefore the angle selected for vorticity analysis should be the maximum angle found between C and C' planes within a sample (Figure 16). However, recent work (Finch et al., 2020) demonstrates that these C' are ephemeral features so for each individual band their orientations are stable, making the utility of this technique even more appealing.

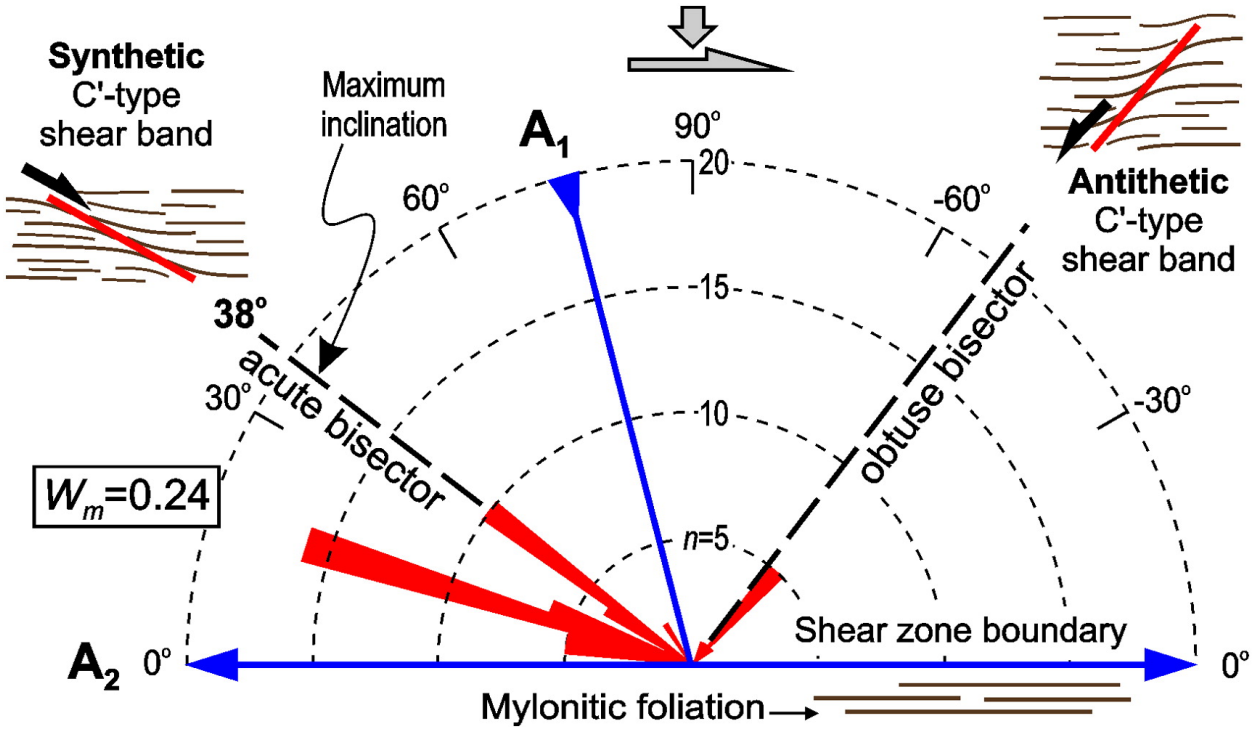

Figure 16: Using the C'-C angle to estimate the vorticity flow. A_1 and A_2 are flow apophyses such that C fabrics are parallel to the shear zone boundary which is coincident with A_2. Angles of C' shear bands are the acute (synthetic C' band) and obtuse (antithetic C' band) bisectors between the flow apophyses. From Xypolias, 2010.

All vorticity techniques have assumptions and limitations that need to be considered. All standard methods only focus on the 2D component of flow in the XZ plane (Xypolias, 2010). In the C-C' method, similar to most methods and applications previously published, we assume monoclinic symmetry and no volume loss during the development of the fabrics (Kurz and Northrup, 2008; Xypolias, 2010).

In monoclinic kinematic models, homogeneous deformation has orthogonal components of simple shear and pure shear with a constant volume. This type of model is commonly used to describe strain in deep ductile shear zones during oblique convergence (Fossen and Tikoff, 1993; Passchier, 1998). Some structural features indicative of monoclinic transpression in vertically bounded shear zones include vertical foliations, vertical or horizontal lineations, flattening fabrics, and asymmetric shear sense indictors on the horizontal plane (Fossen and Tikoff, 1993). The kinematics within the BAM along the SISZ have been extensively modeled and are best described as triclinic transpression, a model that can explain obliquely plunging lineations in a transpressional zone (Díaz Azpiroz and Fernández, 2007; Fernández et al., 2013). Triclinic transpression models can have an oblique simple shear component (Lin et al., 1998), an oblique extrusion direction (Czeck and Hudleston, 2003), or both (Fernández et al., 2013). In the SISZ, D2 deformation in the BAM matches a triclinic model with about 60° inclined shear zone boundaries, horizontal simple shear, and nearly vertical or slightly inclined (20° from vertical) extrusion direction that varies somewhat along different segments of the SISZ (Díaz Azpiroz and Fernández, 2007; Fernández et al., 2013).

Although the precise kinematic model of the PdL along the SISZ is unlikely to fit the assumptions of the vorticity analysis techniques, the discrepancy between the idealized model and the actual kinematics is likely to be relatively minor and consistent throughout the zone.

Therefore we anticipate that the exact values of the kinematic vorticity numbers that we determine here are not accurate, but the relative differences should allow us to separate different types of kinematics across the strain gradient (Table 2).

Table 2: The different types of strain that a deformed body can experience and corresponding kinematic vorticity number.

Type of Strain	**Value of W_n**
Pure Shear	0
General Shear	$0 < W_n < 1$
Simple Shear	$W_n = 1$
Rigid-body rotation	$W_n = \infty$

CHAPTER 4: Results

4.1 Field observations and Qualitative determination of strain

The predominantly quartz rich PdL formation is comprised of slates, phyllites, quartzites and mica schists. Close to the SISZ, massive quartzites are interbedded with schists, while further away thinner quartzites are interbedded with phyllites. Complex geometries within these quartzite-phyllite layers include shear bands, S-C structures, and lozenges of lesser deformed rocks surrounded by small shear zones. Furthest away from the SISZ, only minor quartzite layers are interbedded with slates (Figure 21).

The foliation of the PdL formation is subparallel to bedding with an average orientation of 129°/64°NE (Figure 17). The PdL foliation orientation matches the orientation of the SISZ (115°/50°NE).

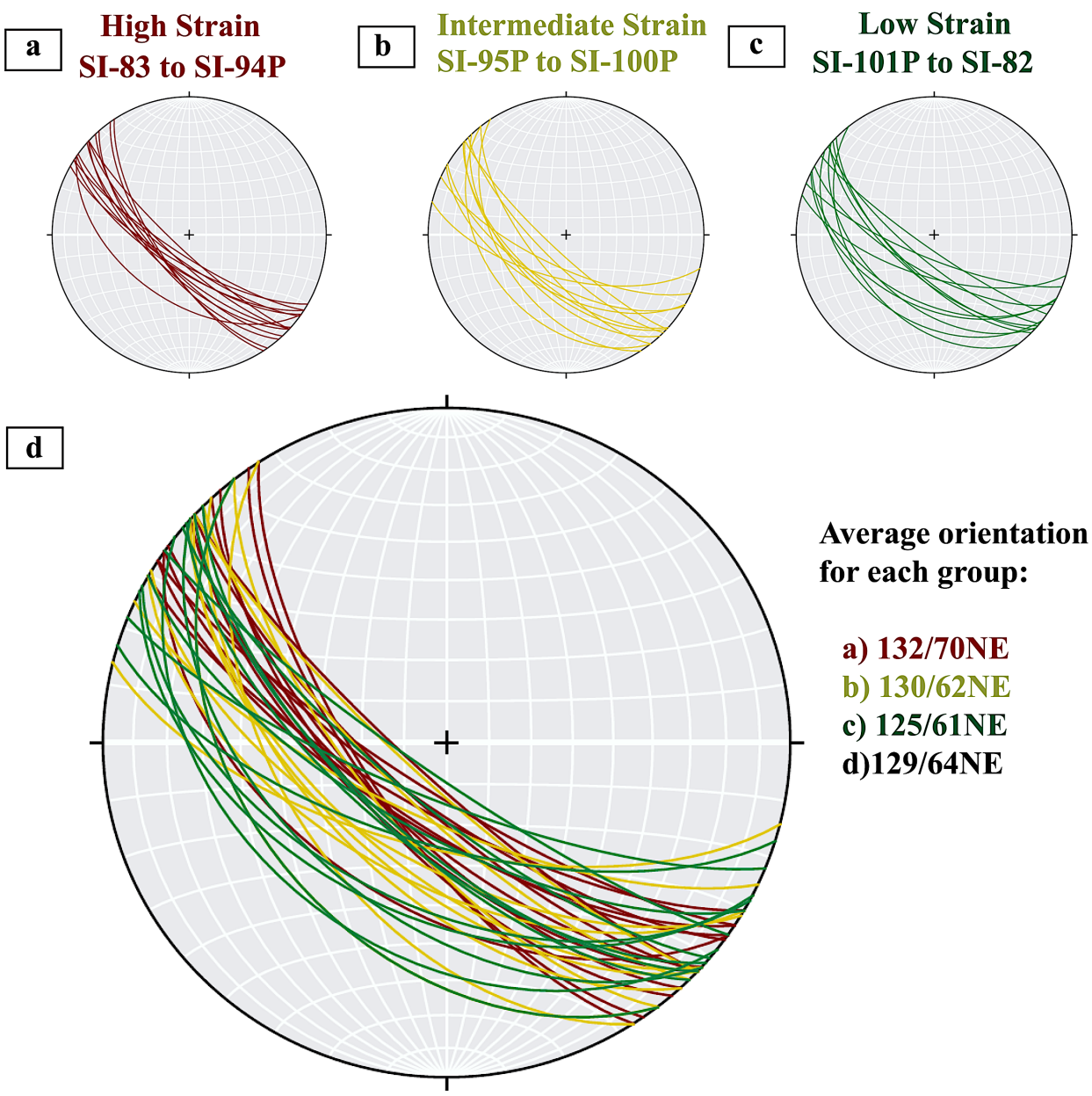

Figure 17: (a) Foliation data from SI-83-SI-94P, high strain, strong fabric; (b) foliation data from SI-95Q-SI-100Q, intermediate strain, intermediate fabric; (c) foliation data from SI-101P-SI-82, low strain, weak fabric; (d) foliation of all samples color-coded by strain groupings.

Fabric strength and metamorphic grade decrease from the shear zone contact. Close to the SISZ (0-65 m), we interpret a high strain region of PdL containing interbedded quartzites and schists that are strongly foliated (Figure 18). The schists have a greenish hue, appear highly altered, and are friable. Their fabric is formed by alignment of mica minerals with shiny, wavy, and closely spaced subplanar schistose foliation. The quartzites are massive without strong foliation.

Further from the shear zone (65-171 m), we interpret an intermediate strained region with interbedded quartzites and phyllites (Figure 19). The phyllites are gray and semi-shiny. Their wavy phyllitic foliation is formed by alignment of micas. Quartzite layers have weak-absent foliation. This region has the most complex geometries including S-C structures mostly indicating thrust motion, shallowly dipping shear bands cutting foliation at high angles, folds, and lozenges of quartzite surrounded by highly deformed phyllite. We avoided sampling in the most complex areas where local shear bands alter fabric orientations, between SI-94P and SI-95Q.

Furthest away from the shear zone (172-250 m), minor amounts of quartzite layers are interbedded with slates. This part of the outcrop is presumably unaffected by the SISZ and has relatively low strain indicated by weak fabric that matches the regional pervasive fabric (Figure 20).

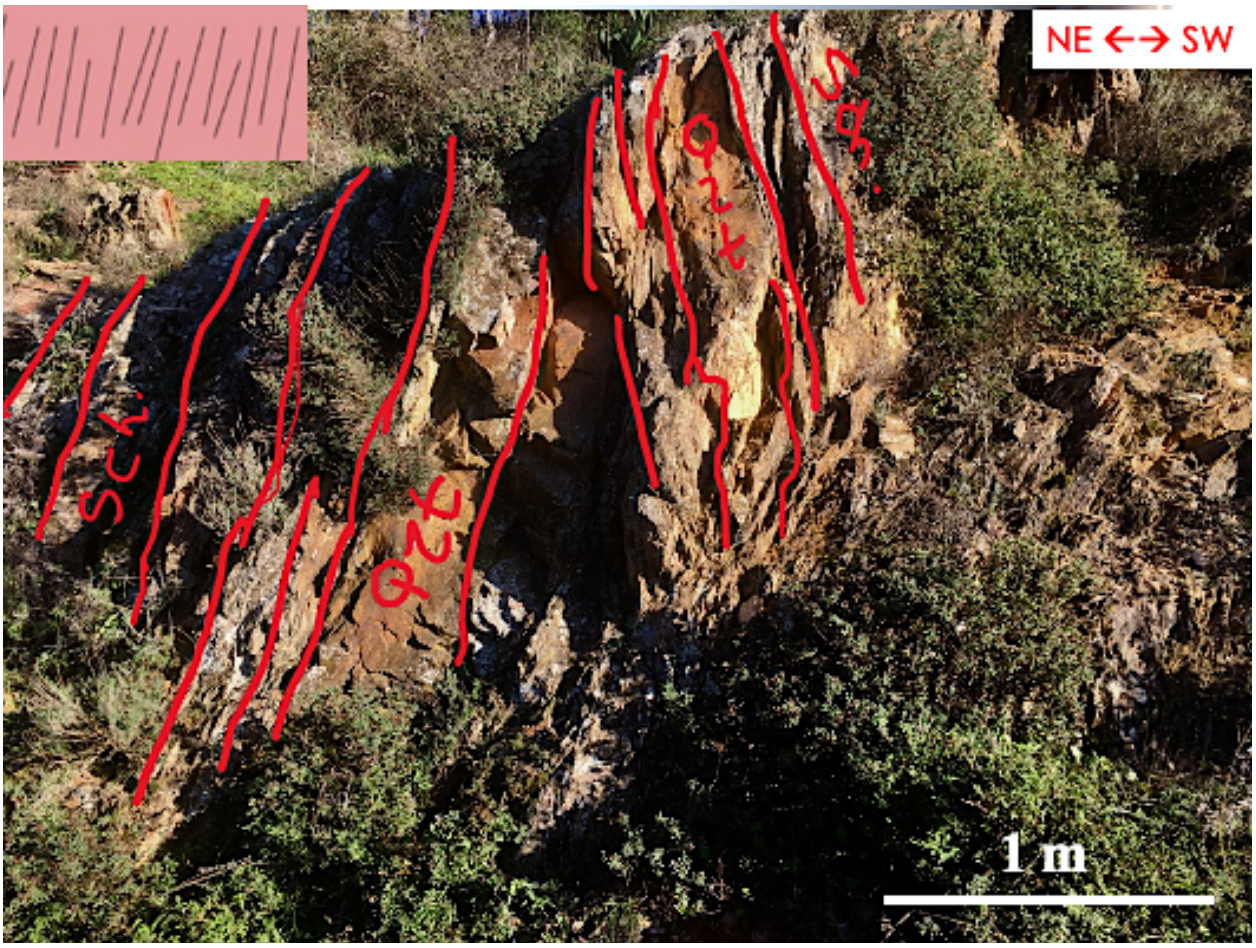

Figure 18: Quartzites and highly altered schists that are close to the shear zone contact (0-65 m). Interpreted to have the highest strain and metamorphic grade.

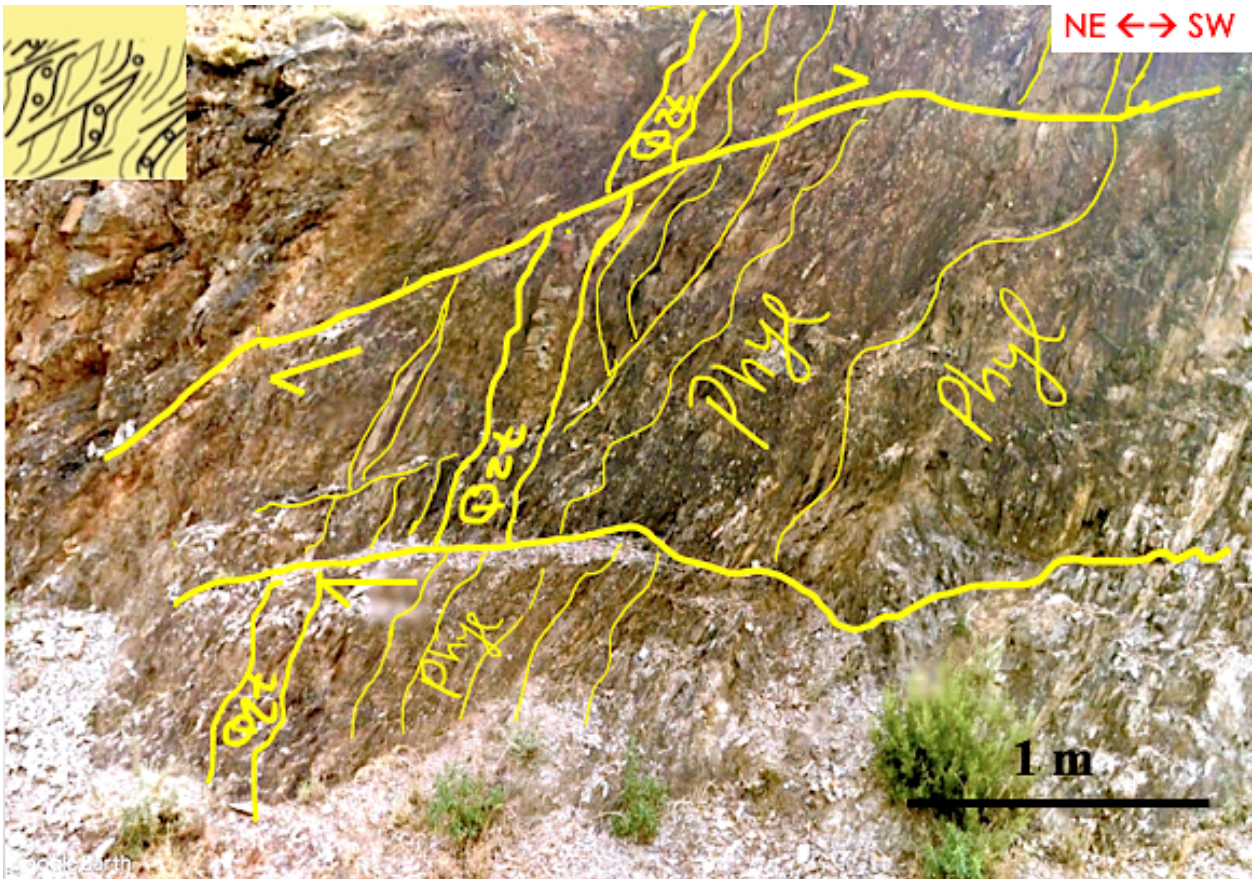

Figure 19: Quartzites and phyllites that are further away from the shear zone contact (65-171 m) interpreted to have intermediate strain and metamorphic grade. They are heterogeneously deformed with complex geometries (e.g. lozenges, S-C structures, shear bands, etc.). Here, shallowly dipping shear bands cut steep foliation planes.

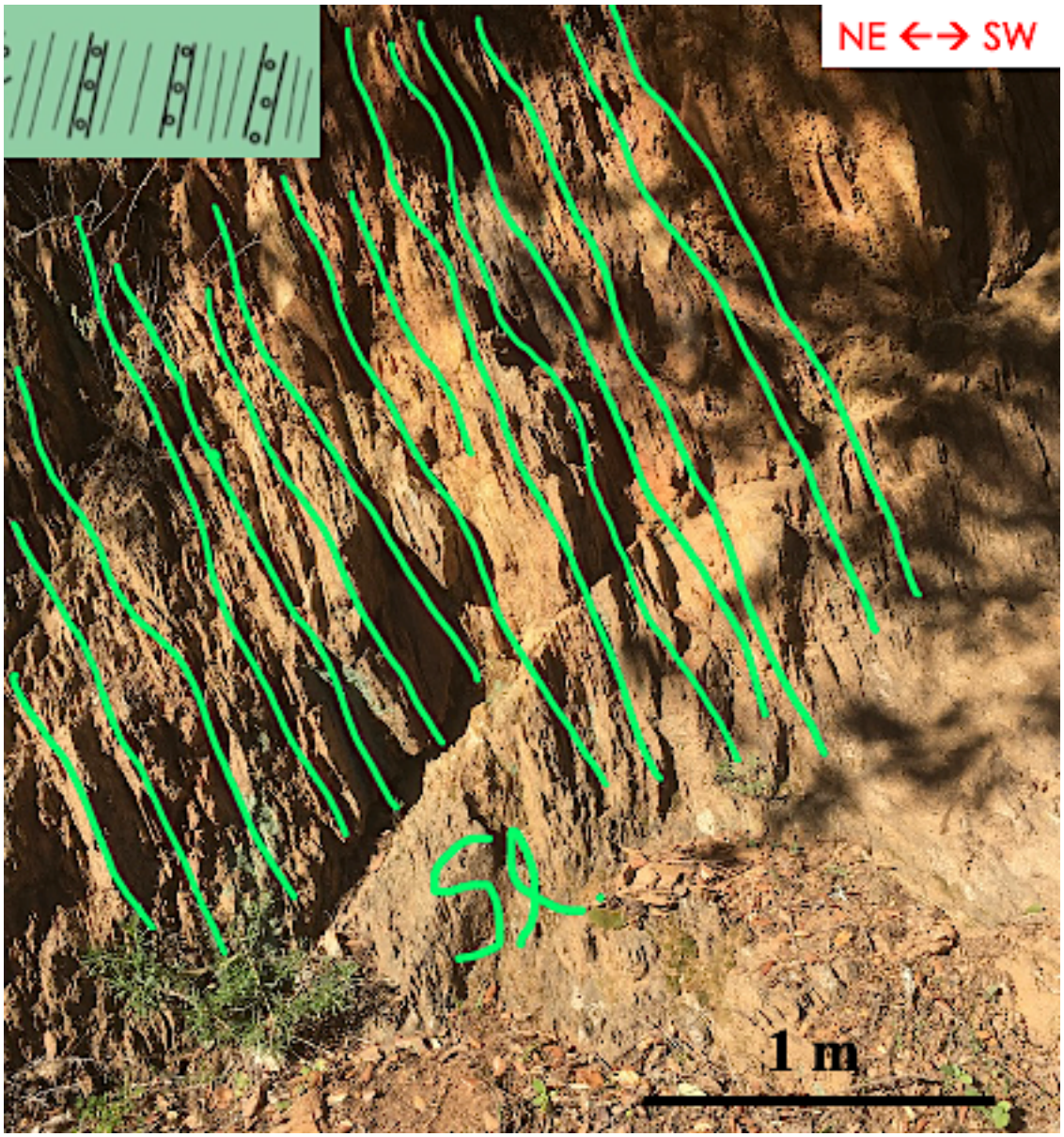

Figure 20: Slate that is the furthest away from the shear zone contact (172-300 m). They are presumably unaffected by the SISZ. Interpreted to have lowest strain and metamorphic grade.

Figure 21: Schematic diagram showing three strain groupings along Almonaster la Real transect: red is high strain (mostly schistose fabrics), yellow is intermediate strain (phyllitic fabrics with heterogeneous strain, lozenges, and oblique shear bands), and green is low strain (slaty cleavage). Modified from Fernández (unpublished figure).

4.2 Qualitative Microstructural Analysis

Twenty-eight thin sections were analyzed under the petrographic microscope to document the minerals and microstructures present across the strain gradient (Appendix 9.2.1 Tables 6-8). The three groupings of strain and metamorphic grade that were identified in the field were confirmed in thin section. Thin sections SI-83 to SI-94P (0-56 m from the shear zone) were grouped in the high strain zone, SI-95P to SI-100P (71- 155 m from the shear zone) were grouped in the intermediate strain zone, and SI-101P to SI-82 (174- >400 m from the shear zone) were grouped in the low strain zone of the PdL. The exact location for boundaries between high, intermediate, and low strain zones were based on a combination of field and microstructural evidence. Of the twenty-eight thin sections, nine were chosen to represent the high, intermediate, and low strain groups within the PdL for more detailed study (Figure 22).

Figure 22: Nine thin sections were chosen to represent the high (top row), intermediate (middle row), and low (bottom row) strain groups for quantitative microstructural analysis.

4.2.1 High Strain Zone (0-65m, SI-83 to SI-94P):

The minerals present include quartz, muscovite, biotite, plagioclase, chlorite, and garnet. The rocks are classified as schists or, in some cases, phyllites. The alignment of micas, alignment of elongated quartz grains, and segregation of mica and quartz layers form a strong fabric. Many quartz grains have sigma-type asymmetric strain shadows indicating top-to-the southwest (thrusting) sense of shear. Quartz grains in the high strain zone show a bimodal grain size; one group has grains approximately 6 mm in diameter and the other group has grains approximately 100 microns in diameter. Plagioclase grains are present in trace amounts, and are generally larger than the quartz grains (7 mm in diameter). Small-scale asymmetric folds and S-C fabrics also indicate top-to-the-southwest shear sense (Figure 24).

Many quartz grains contain microstructures consistent with crystal-plasticity including undulose extinction, subgrains, “puzzle piece” grain shapes and bulged boundaries, which are typical of grain boundary migration; very small grains, sometimes with triple junctions, which are typical of dynamic recrystallization; and rare deformation lamellae (Figure 23-25). Micas are often bent around the quartz grains indicating internal deformation of the crystal. Several microstructures are consistent with fluid enhanced diffusive mass transfer (DMT). Selvage seams formed by concentrations of micas and other minerals nucleate around the foliation-parallel edges of large quartz grains and propagate across the rock (Figure 23a). Newly crystallized grains within the strain shadows surrounding these large quartz grains are a mixture of quartz, mica, and chlorite.

Several types of grains also display evidence of fluid-assisted brittle deformation. Intragranular microcracks are present in quartz, feldspar, and garnet grains. Some large quartz and feldspar grains include fluid inclusion trails.

Near the high to intermediate strain boundary (SI-94P), the mineralogy and microstructures begin to transition. The minerals present are reduced to primarily quartz, muscovite, and biotite. The asymmetric sigma-type strain shadow tails surrounding the large quartz grains are more ambiguous, but still overall dextral. Evidence for dislocation creep, DMT, and fluid enhanced embrittlement all remain. A cryptocrystalline orange-red material coats some of the sample, often along mica-rich planes, suggesting deposition by a fluid which took advantage of planes of weakness (Figure 25).

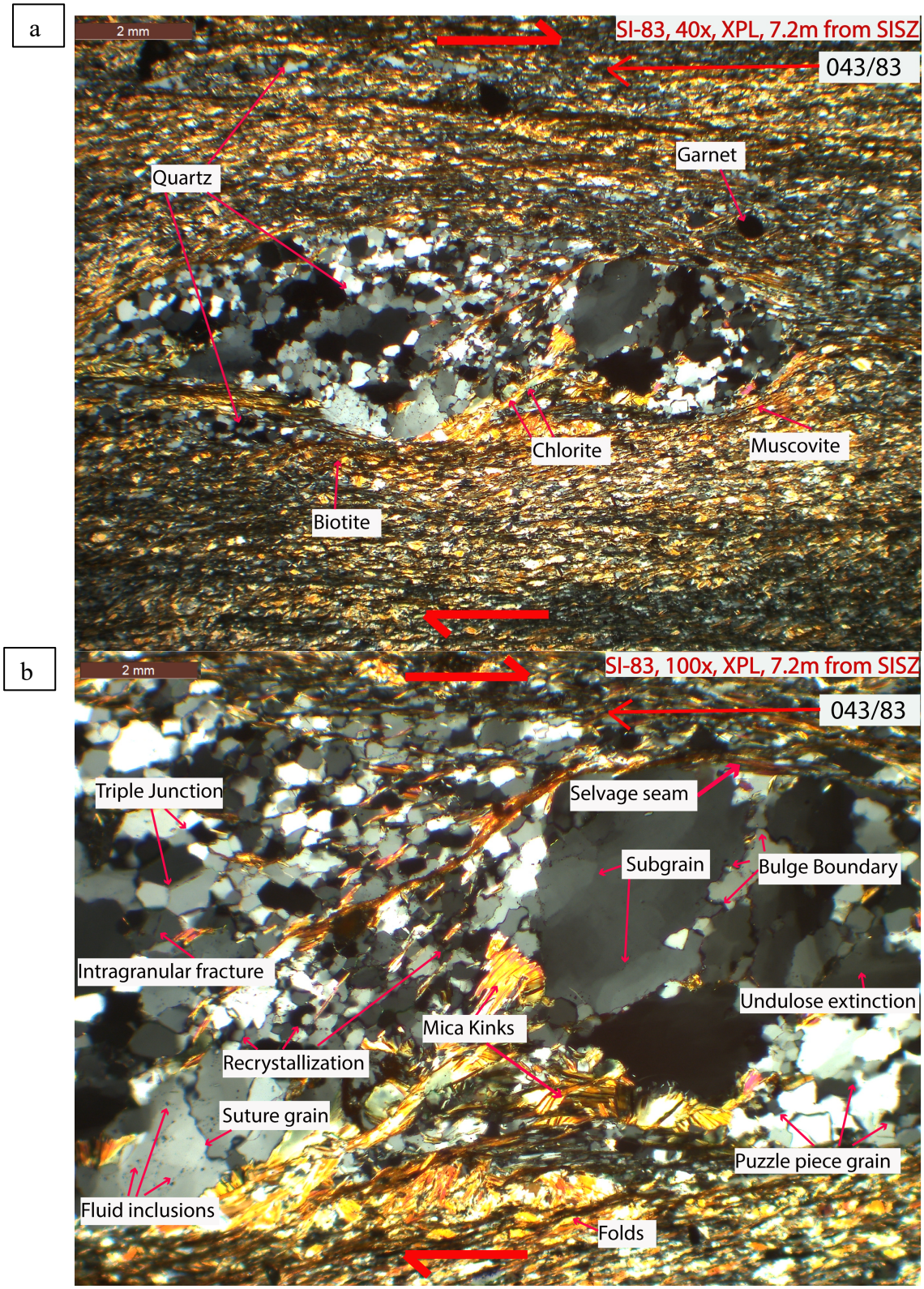

Figure 23: Selected areas of SI-83 (high strain) thin section with orientation of the long axis show in upper right (trend/plunge) and shear sense indicated. **(**a) Minerals present in the SI-83 thin section, (b) microstructures present in SI-83.

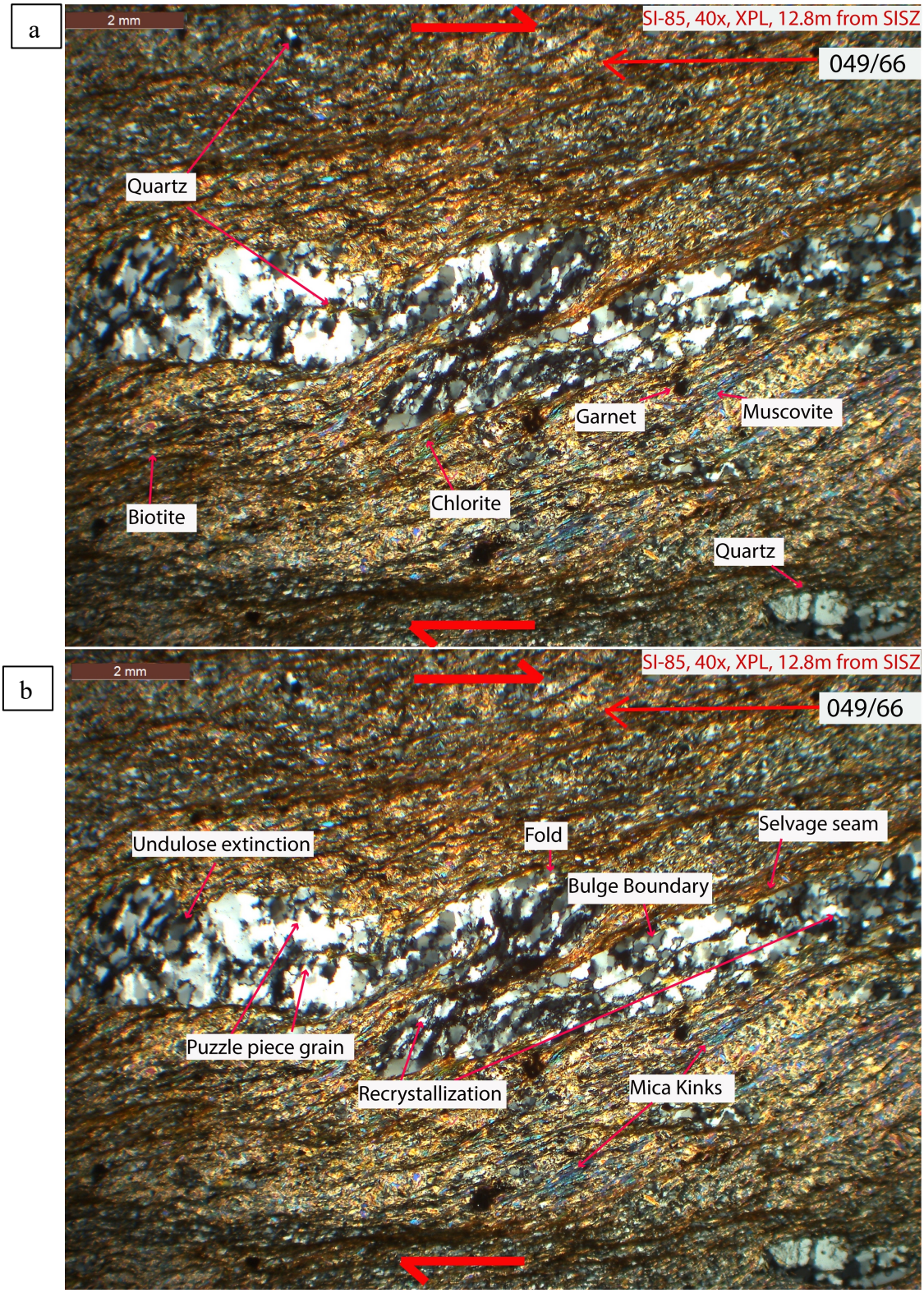

Figure 24: Selected areas of SI-85 (high strain) thin section with orientation of the long axis show in upper right (trend/plunge) and shear sense indicated. **(**a) Minerals present in the SI-85 thin section, (b) microstructures present in SI-85.

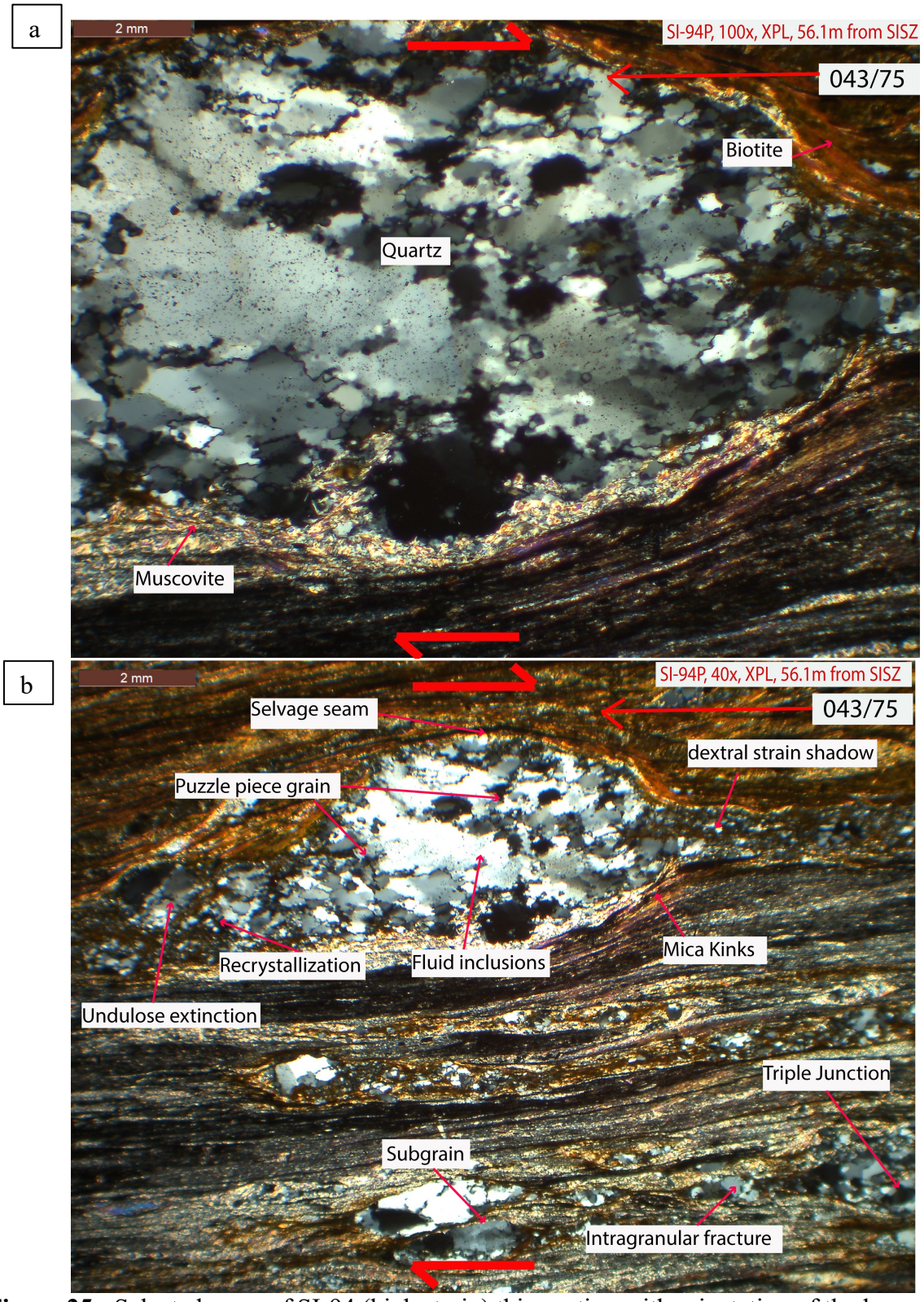

Figure 25: Selected areas of SI-94 (high strain) thin section with orientation of the long axis show in upper right (trend/plunge) and shear sense indicated. (a) Minerals present in the SI-94P thin section, (b) microstructures present in SI-94P.

4.2.2 Intermediate Strain Zone (65-171m, SI-95P to SI-100P):

The minerals present include quartz, muscovite, biotite and minor amounts of chlorite, and the rocks are classified as phyllites. Aligned micas, elongated quartz crystals, and segregated bands on minerals create a moderate fabric. Quartz has sigma-type strain shadows with a top-to-the-southwest (thrust) shear sense (Figure 27). Quartz grains in the intermediate strain zone are dispersed widely and have a bimodal grain size; one group has grains approximately 7 mm in diameter and the other group has grains approximately 150 microns in diameter. Rare small-scale asymmetric folds are present only near the high-intermediate transition.

Quartz grains have microstructures that are consistent with crystal-plasticity such as undulose extinction, subgrains; “puzzle piece” grain shapes and bulged boundaries, which are typical of grain boundary migration; very small grains, sometimes with triple junctions, which are typical of dynamic recrystallization; and rare deformation lamellae (Figure 28). Micas are often bent around the quartz grains indicating internal deformation of the crystal.

Microstructures that are consistent with fluid-enhanced diffusive mass transfer (DMT) such as selvages seams that nucleate around the foliation parallel edges of large quartz grains. Newly crystallized grains within the strain shadows surrounding these quartz grains are a mixture of quartz and micas.

Brittle deformation is evident in many of the grains. Intragranular microcracks are present in many quartz grains. Only a few large quartz grains include fluid inclusion trails.

Near the intermediate to low strain boundary (SI-100P), the minerals present are still primarily quartz, muscovite, and biotite. The prevalence of microstructures steadily diminishes. Asymmetric sigma-type strain shadow tails surrounding the large quartz grains still indicate thrust motion. Evidence of dislocation creep, DMT, and fluid enhanced embrittlement all remain

to a lesser degree compared to the high strain zone. Cryptocrystalline red material along mica-rich planes suggests that there was deposition by a fluid that took advantage of planes of weakness (Figure 26 & 27).

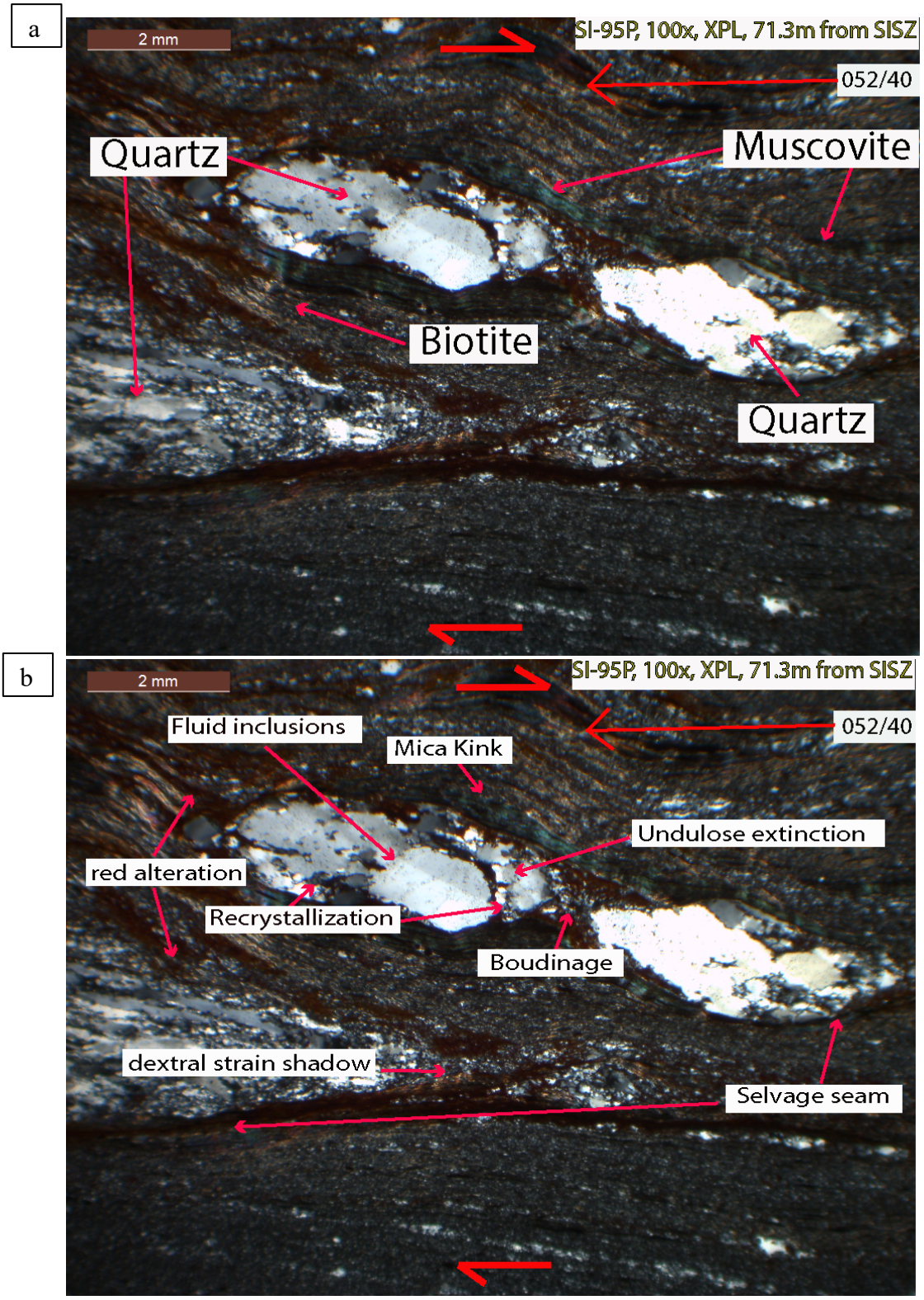

Figure 26: Selected areas of SI-95 (intermediate strain) thin section with orientation of the long axis show in upper right (trend/plunge) and shear sense indicated. (a) Minerals present in the SI-95P thin section, (b) microstructures present in SI-95P.

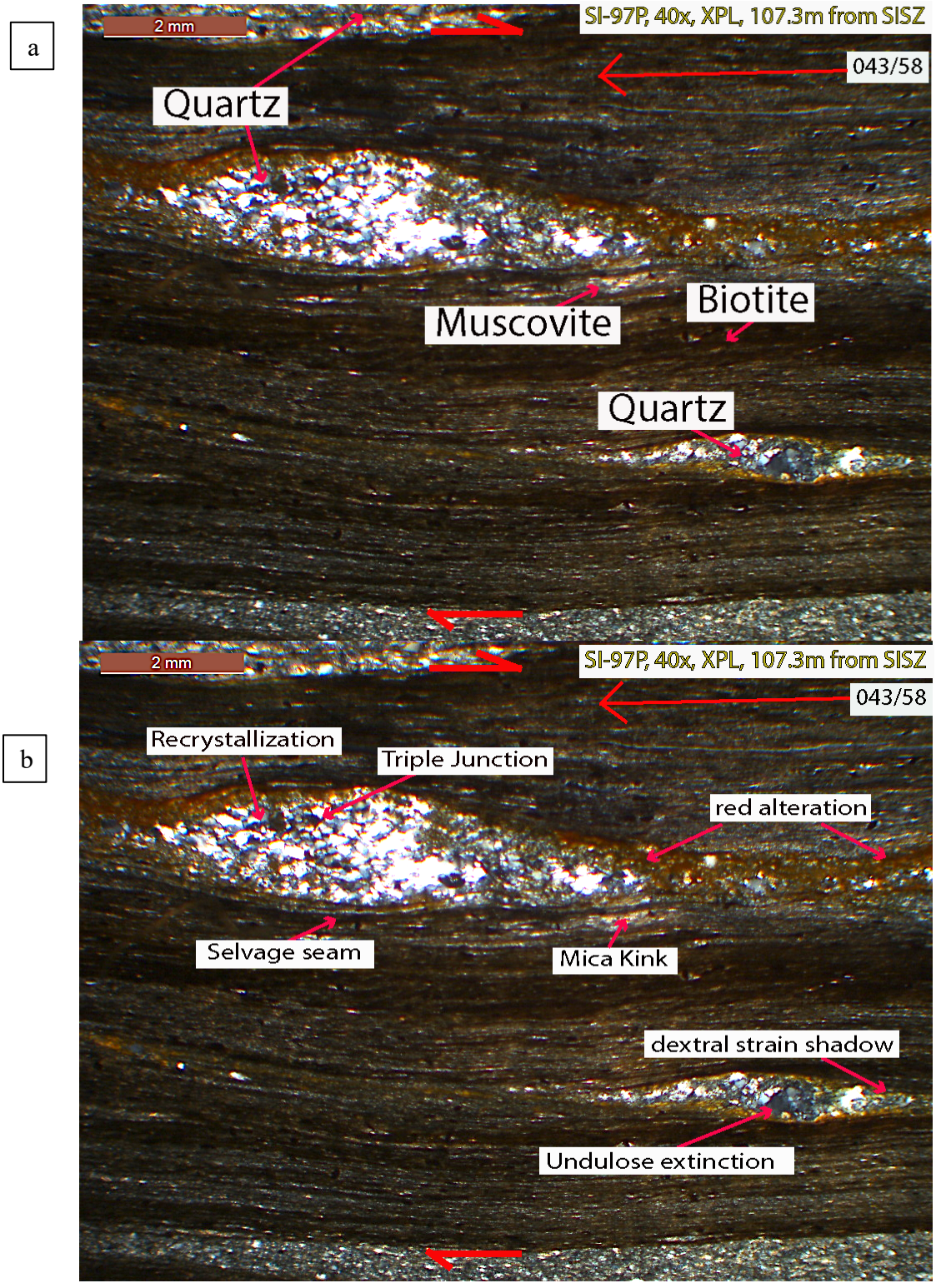

Figure 27: Selected areas of SI-97P (intermediate strain) thin section with orientation of the long axis show in upper right (trend/plunge) and shear sense indicated. (a) Minerals present in the SI-97P thin section, (b) microstructures present in SI-97P.

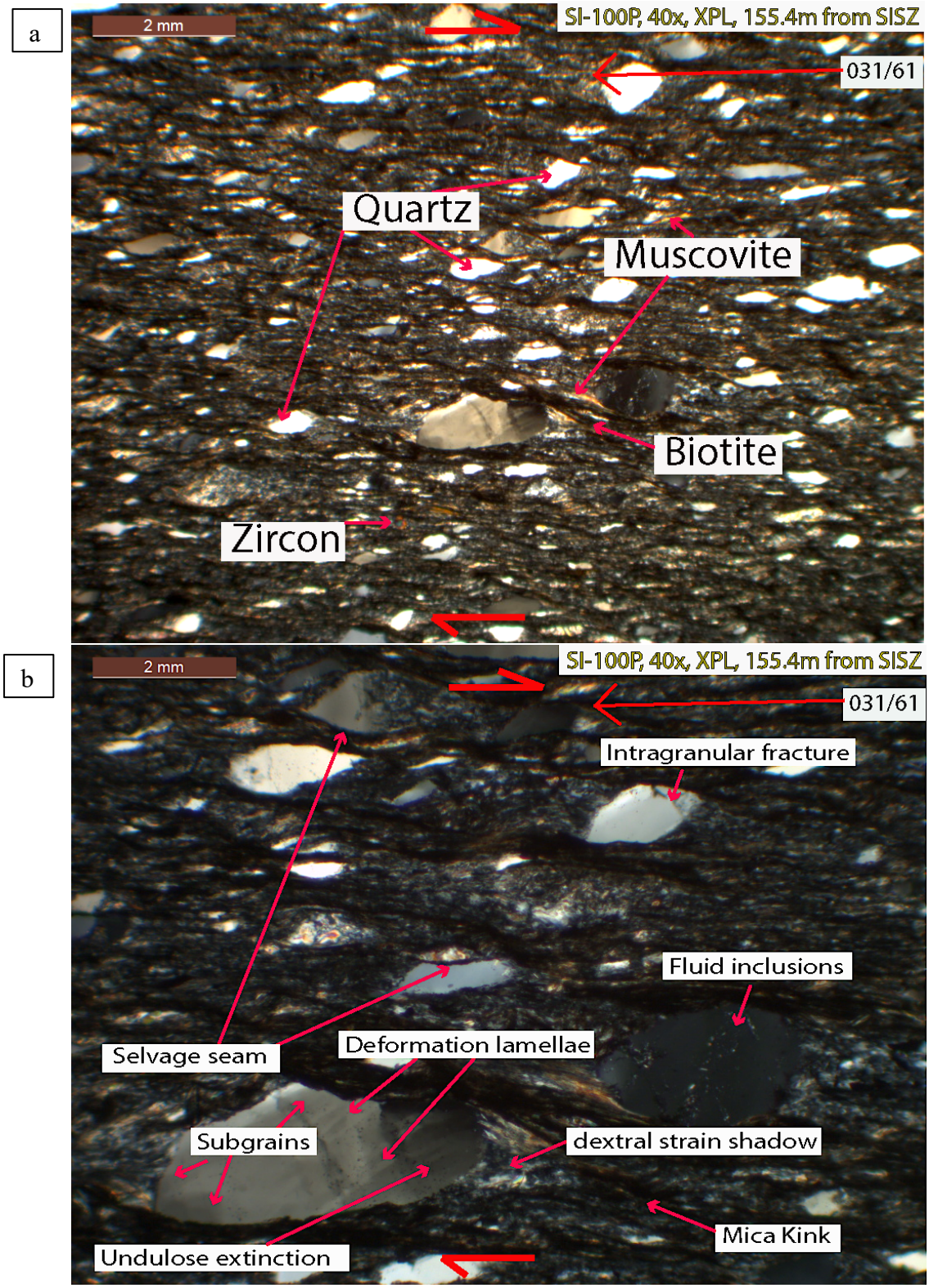

Figure 28: Selected areas of SI-100P (intermediate strain) thin section with orientation of the long axis show in upper right (trend/plunge) and shear sense indicated. (a) Minerals present in the SI-100P thin section, (b) microstructures present in SI-100P.

4.2.3 Low Strain Zone (172-250m, SI101P to SI-106P):

The minerals present include quartz, muscovite, biotite, and trace zircons. The rocks are slates, with some phyllites present. The most prominent feature are the foliations created by biotite mica layers that wrap around larger quartz grains creating a weak to moderate fabric. Many quartz grains have sigma-type strain shadows with a top-to-the-southwest shear sense (Figure 29). A majority of quartz grains in the low strain zone have a bimodal grain size near the intermediate zone contact (large grain group with diameter 4.5 mm and small grain group with diameter 250 microns) or a uniform fine-grained size further from the SISZ (diameter 150 microns. The small-scale asymmetric folds are not common in the low strain zone.

Quartz grains have microstructures that are consistent with crystal-plasticity such as undulose extinction, subgrains; “puzzle piece” grain shapes and bulged boundaries, which are typical of grain boundary migration; very small grains, sometimes with triple junctions, which are typical of dynamic recrystallization (Figure 30). Micas often bend around quartz grains indicating internal deformation of the crystal. Many microstructures are consistent with fluid-enhanced diffusive mass transfer (DMT). Prominent selvage seams nucleate around the foliation parallel edges of large quartz grains. Newly crystallized grains within the strain shadows surrounding these quartz grains are a mixture of quartz and micas.

Brittle deformation including intragranular microcracks are present in a few of the quartz grains. Only a few large quartz grains include fluid inclusion trails.

The quantity of microstructures steadily diminishes within the low strain zone with distance from the SISZ. Evidence of dislocation creep, DMT, and brittle deformation all remain; however, they diminish with increasing distance from the SISZ contact. Asymmetric sigma-type strain shadows surround the large quartz grains indicating thrust motion. Cryptocrystalline orange-red material is seen along the mica-rich planes, which suggests deposition by a fluid that took advantage of planes of weakness (Figure 31).

a

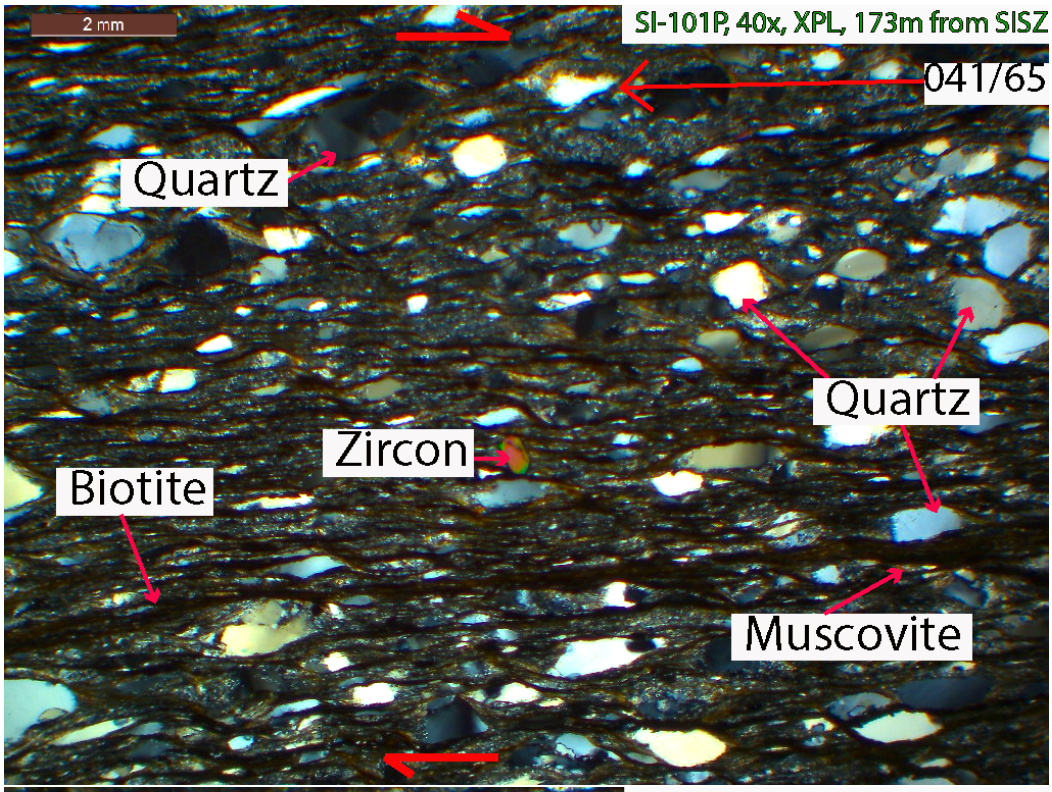

b

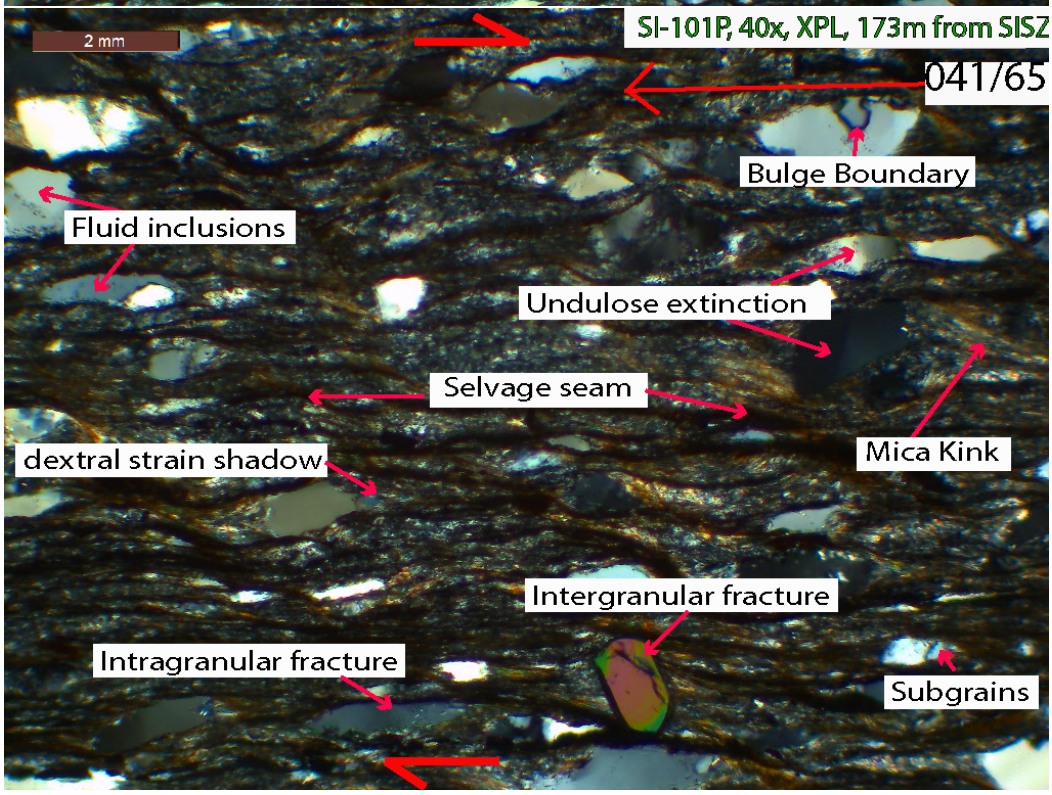

Figure 29: Selected areas of SI-101P (low strain) thin section with orientation of the long axis show in upper right (trend/plunge) and shear sense indicated. (a) Minerals present in the SI-101P thin section, (b) microstructures present in SI-101P.

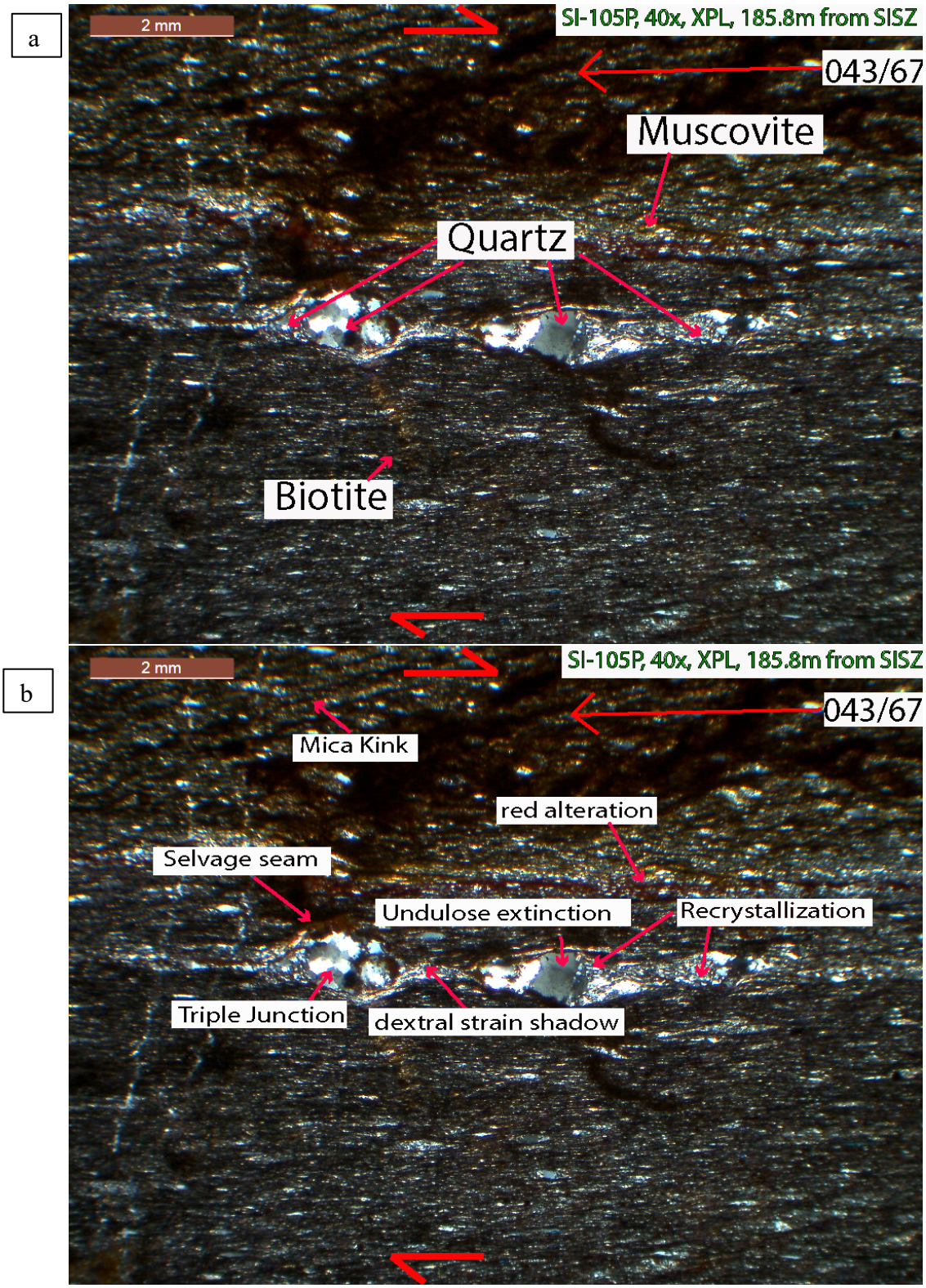

Figure 30: Selected areas of SI-105P (low strain) thin section with orientation of the long axis show in upper right (trend/plunge) and shear sense indicated. (a) Minerals present in the SI-105P thin section, (b) microstructures present in SI-105P.

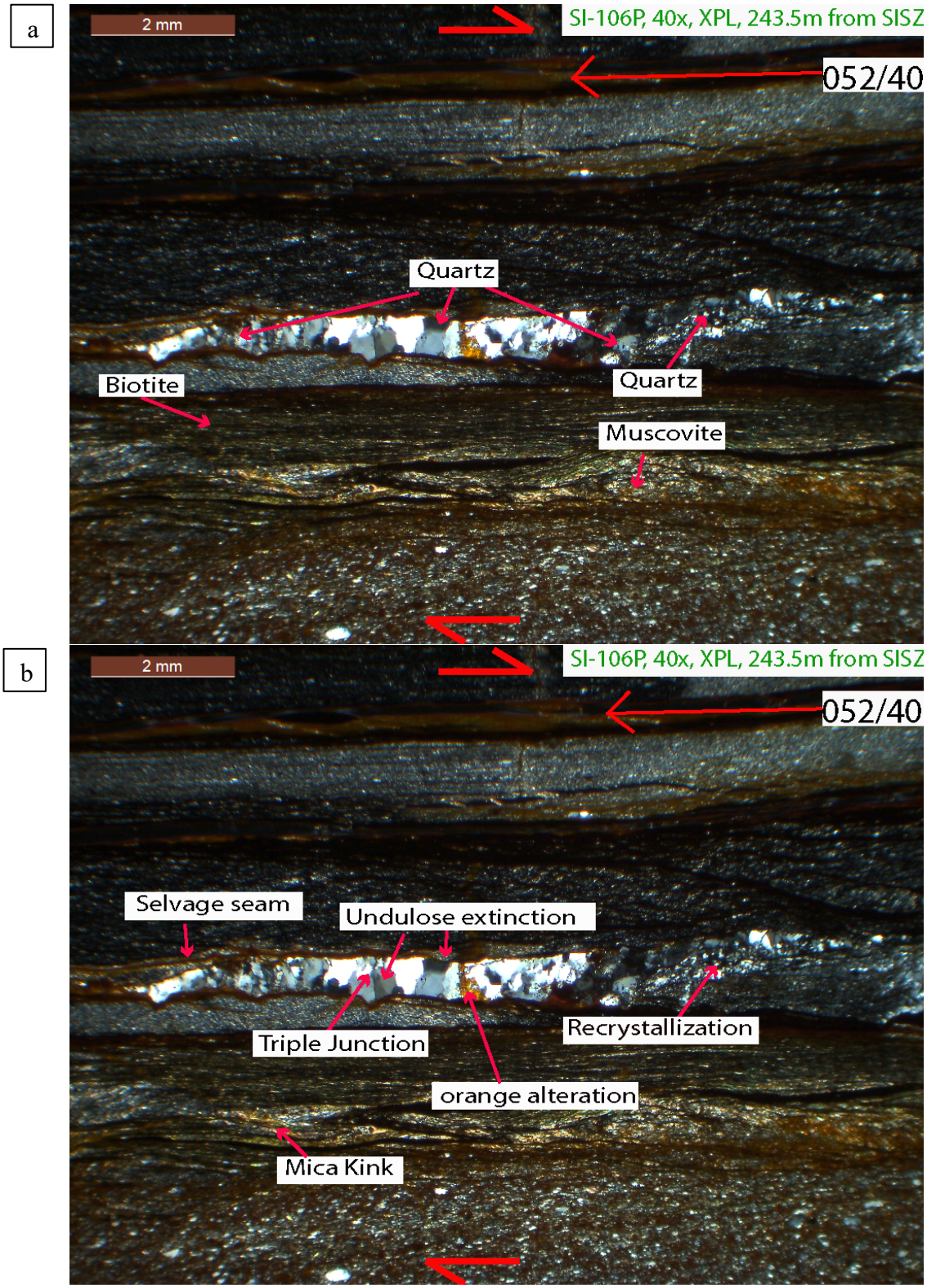

Figure 31: Selected areas of SI-106P (low strain) thin section with orientation of the long axis show in upper right (trend/plunge) and shear sense indicated. (a) Minerals present in the SI-106P thin section, (b) microstructures present in SI-106P.

4.3 Quantitative Microstructure Point Count Analysis:

Results from the microstructure point count analysis are reported in Appendix 9.2.2. While all studied thin sections show evidence of brittle, DMT, and crystal-plastic deformation processes, the detailed microstructural assemblages differ based upon rock type, strain magnitude, and distance from the shear zone.

4.3.1 High Strain Zone (SI-83, SI-85, SI-94P):

The samples in this groups are schists (SI-83, SI-85) and a phyllite (SI-94P) from the high strain group. Average mineral concentrations are quartz 42%, biotite 26%, and muscovite 30% with trace abundances of plagioclase, K-feldspar, garnet, and chlorite (Figure 35).

Average microstructural data were plotted for quartz, feldspars (if present), and micas (Figure 35). In this group, crystal-plastic microstructures in quartz such as undulose extinction, bulged boundaries, subgrains, and puzzle piece grains and mica kinks gradually increase toward the shear zone. Microstructures indicative of recovery including triple junctions and recrystallized grains similarly increase toward the shear zone. DMT microstructures including selvage seams, and sutured grain boundaries also gradually increase towards the shear zone, but there is no pattern with strain shadows. Brittle microstructures such as intragranular fractures, intergranular fractures, veins, and fluid inclusions also increase toward the shear zone (Figure 32).

The highest density of microstructures exist immediately adjacent to the SISZ. At 7.2 m from the SISZ contact, SI-83 shows a dominance in crystal plasticity and recovery microstructures, like the other high strain samples, but also has a pronounced increase in DMT and brittle microstructures.

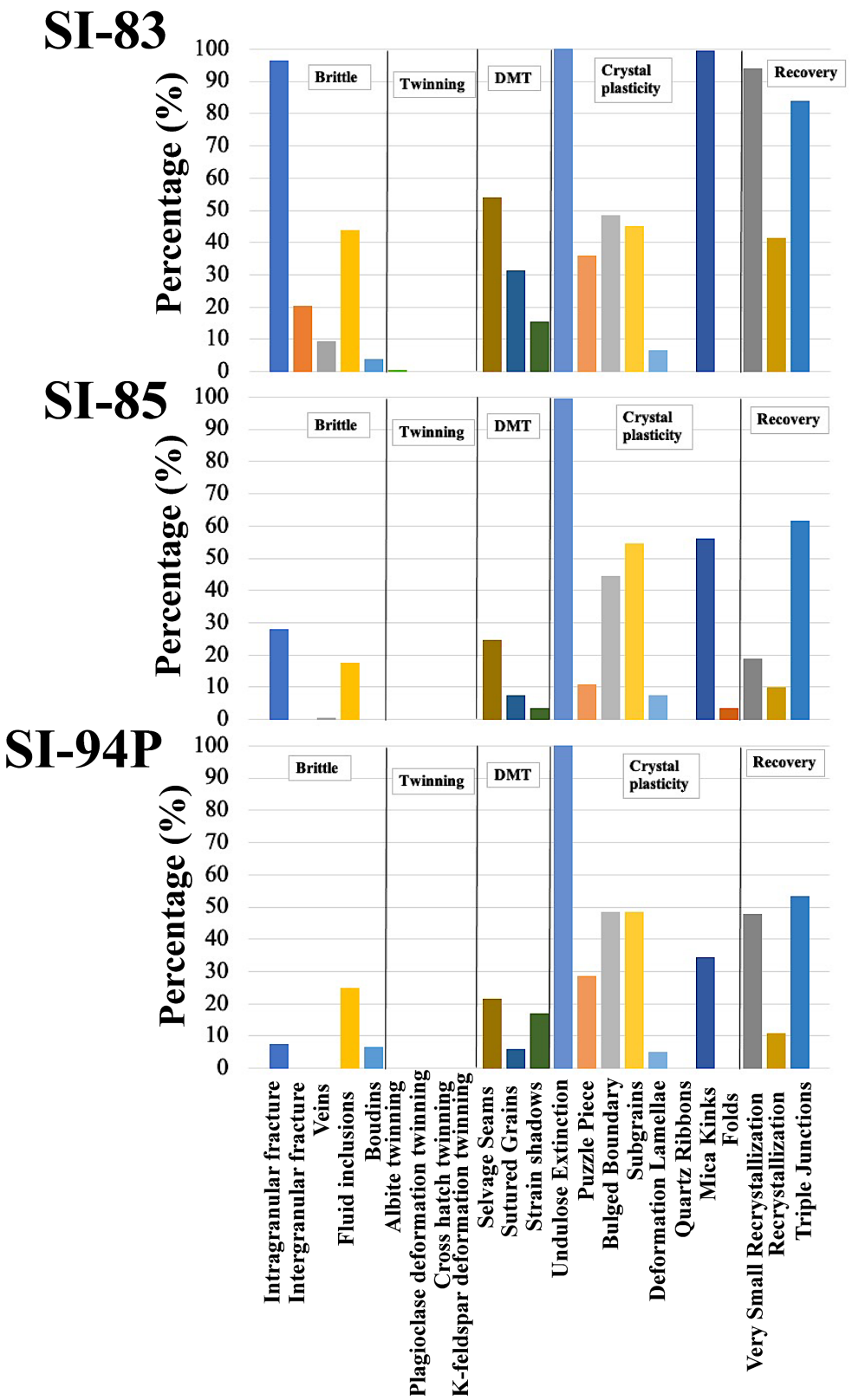

Figure 32: Point count analysis of SI-83 to SI-94P, which are in the high strain zone in the PdL. All microstructures were observed in quartz, unless otherwise indicated.

4.3.2 Intermediate Strain Zone (SI-95P, SI-97P, SI-100P):

Most samples in this group are phyllites. Average mineral concentrations are quartz 25%, biotite 25%, and muscovite 49%. Chlorite, K-feldspar, plagioclase, and garnet were not observed (Figure 35).

In this group, microstructures in quartz such as undulose extinction, bulged boundaries, subgrains, and puzzle piece grains and mica kinks gradually decrease with distance from the shear zone. Recovery microstructures also gradually decrease. DMT microstructures such as selvage seams and sutured grains gradually decreases, while strain shadows have no pattern. The prevalence of brittle microstructures such as intragranular fractures, intergranular fractures, veins, and fluid inclusions remain stable in this zone (Figure 33).

Intensity of fabric at the outcrop and thin section scale show that a shear band is present at the transition between the intermediate to low strain zone (SI-100P at 155 m from the SISZ). At this location, there is an apparent increase in microstructures related to crystal plasticity, DMT and brittle processes; however, the trend of the recovery microstructures is ambiguous.

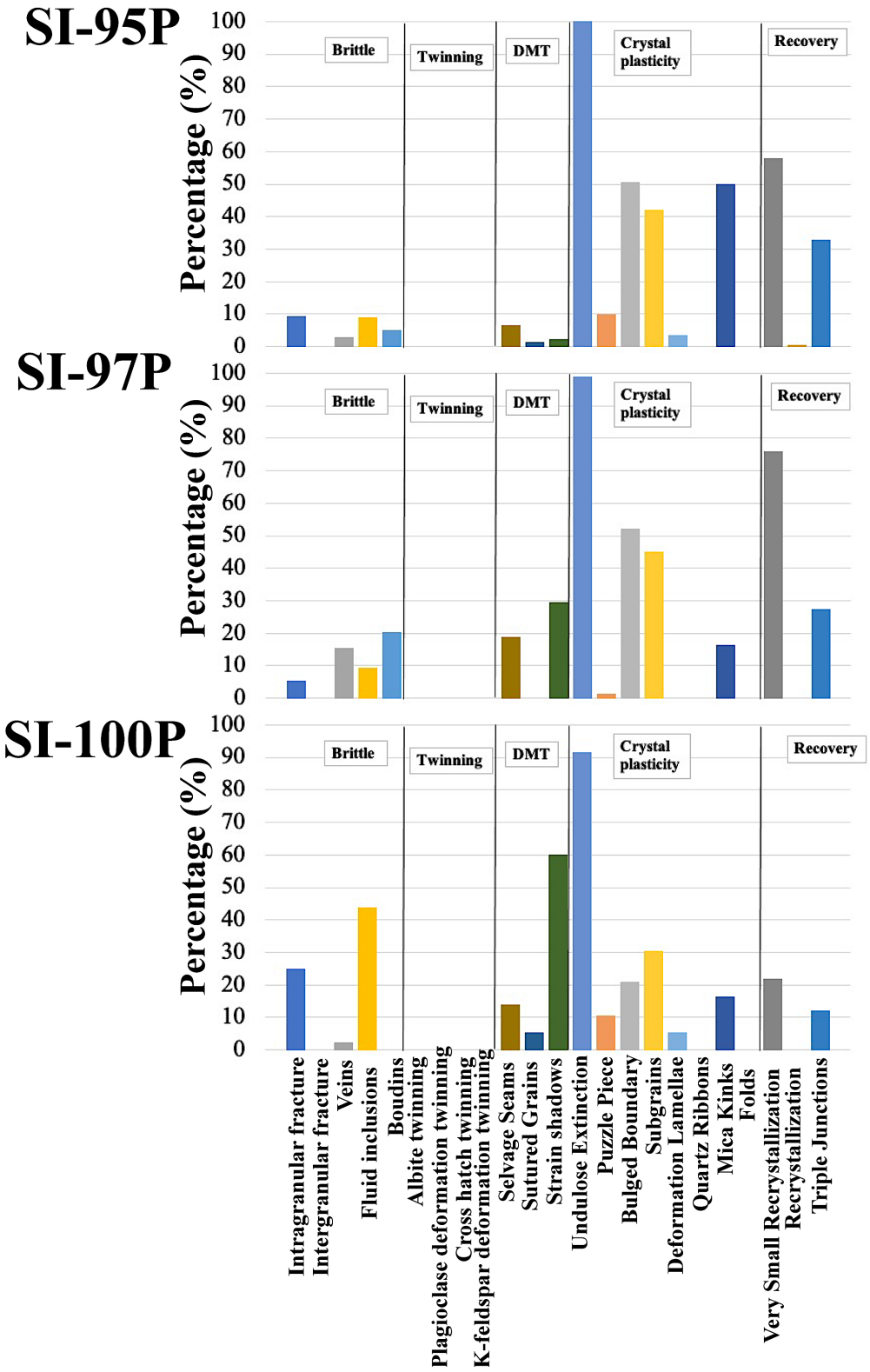

Figure 33: Point count analysis of SI-95P to SI-100P, which are in the high strain zone in the PdL. All microstructures were observed in quartz, unless otherwise indicated.

4.3.3 Low Strain Zone (SI-101P, SI-105P, SI-106P):

The samples in this groups are phyllite (SI-101P, SI-85) and slates (SI-105P, SI-106P). Average mineral concentrations are quartz 26%, biotite 30%, and muscovite 44% with trace abundances of albite (Figure 35). In this group, microstructures in quartz such as undulose extinction, bulged boundaries, subgrains, and puzzle piece grains and mica kinks gradually decrease with distance from the shear zone. Recovery microstructures also decrease significantly. DMT microstructures such as selvage seams, strain shadows, and sutured grains and brittle microstructures such as intragranular fractures, intergranular fractures, veins, and fluid inclusions are relatively sparse (Figure 34).

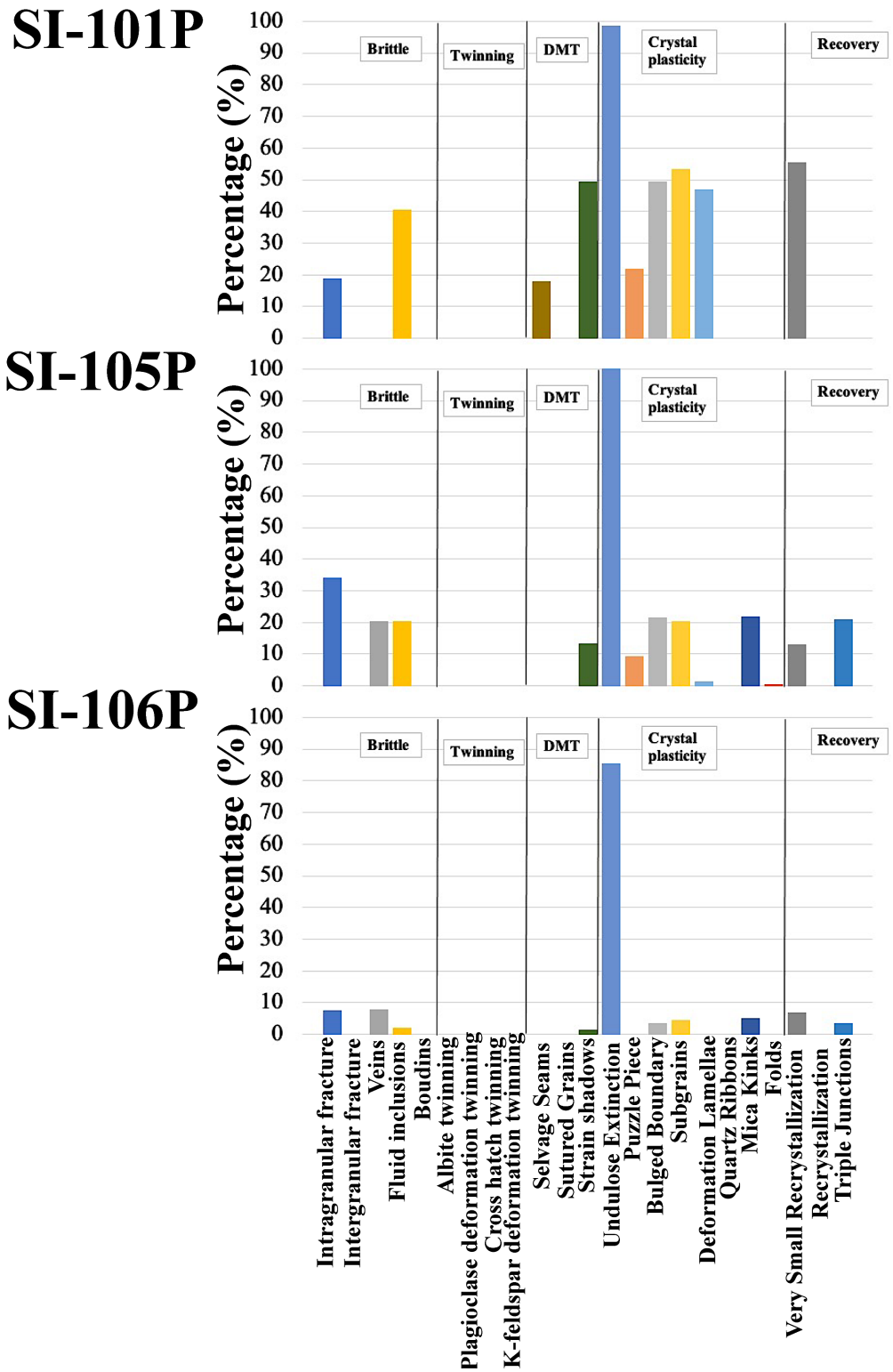

Figure 34: Point count analysis of SI-101P to SI-106P, which are in the high strain zone in the PdL. All microstructures were observed in quartz, unless otherwise indicated.

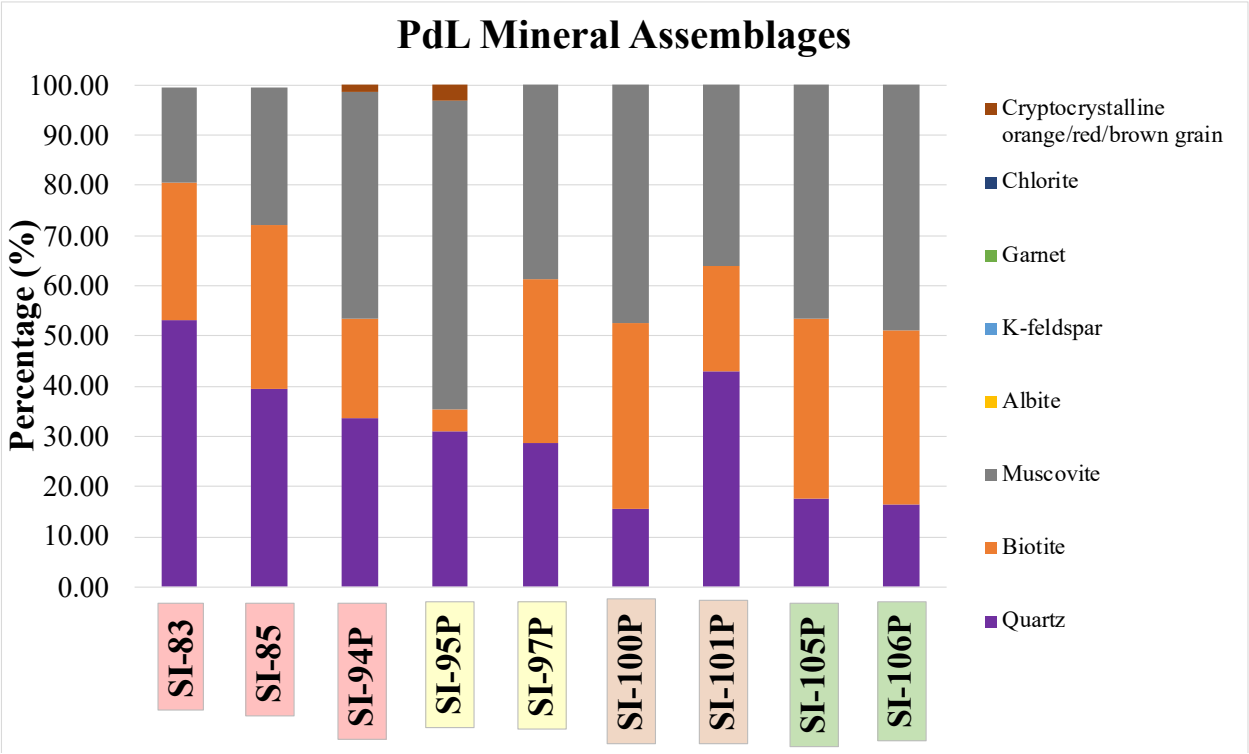

Figure 35: PdL mineral assemblage percentages from point counting data of the 9 thin sections.

4.3.4 Microstructures Present vs Shear Zone Distance Plots:

The microstructures present were plotted against the distance from the shear zone to visualize the variations across the strain gradient.

Microstructures formed by crystal plasticity and recovery can be found across the entire strain gradient, but gradually decrease away from the shear zone (Figure 38 & 39). Microstructures formed by DMT existed throughout the strain gradient, but substantially increase close to the shear zone, especially within 50 m (Figure 37). Brittle microstructures such as intragranular fractures, fluid inclusions, and veins are found throughout the strain gradient, but are significantly more abundant within 10 m of the SISZ (Figure 36).

The dextral and sinistral asymmetric indicators as seen in the thin section view can be converted to a geographic reference frame so that shear sense is top to the SW vs top (thrust) to

the NE (normal). These grain scale asymmetric indicators of sigma-type clasts, S-C fabrics, and cm scale asymmetric folds indicate dominant thrust motion (top to the southwest) (Figure 40).

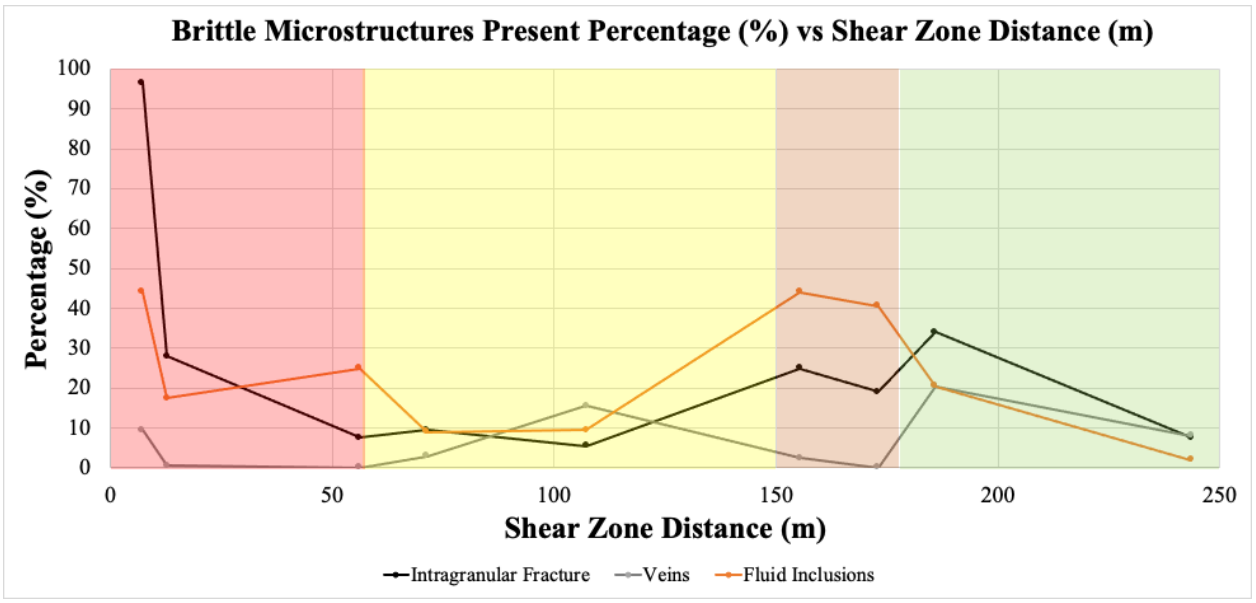

Figure 36: Brittle Microstructures in the PdL vs. Distance (m) from the SISZ; plot of SI-83 to SI-106P.

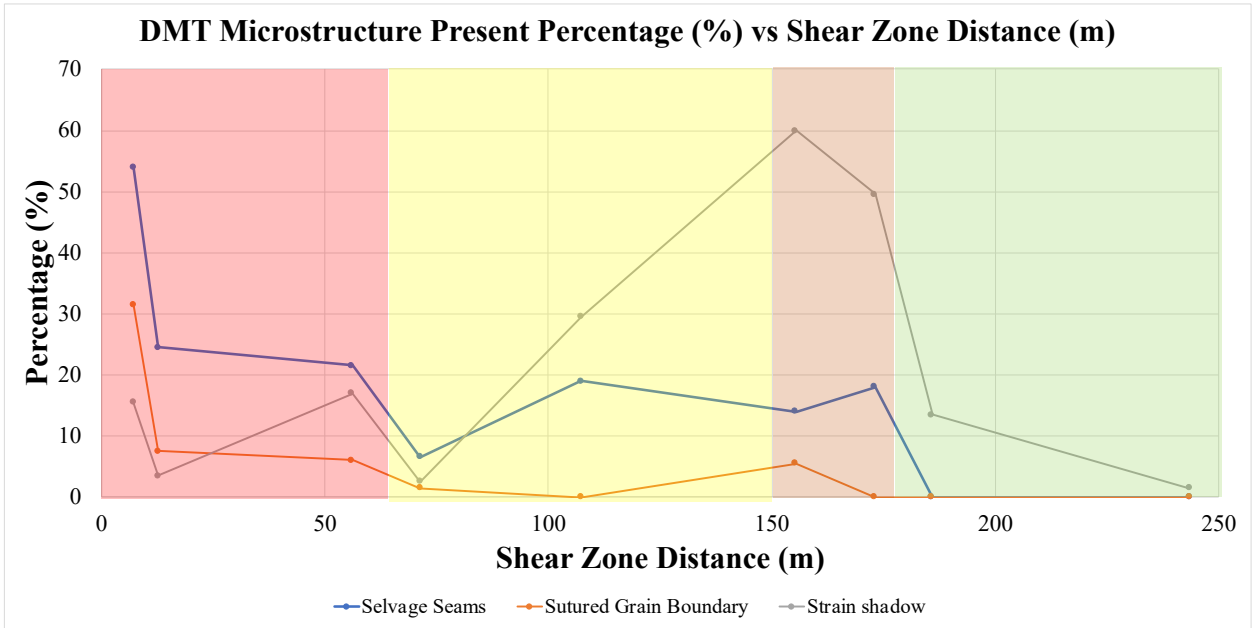

Figure 37: DMT Microstructures in the PdL vs. Distance (m) from the SISZ; plot of SI-83 to SI-106P.

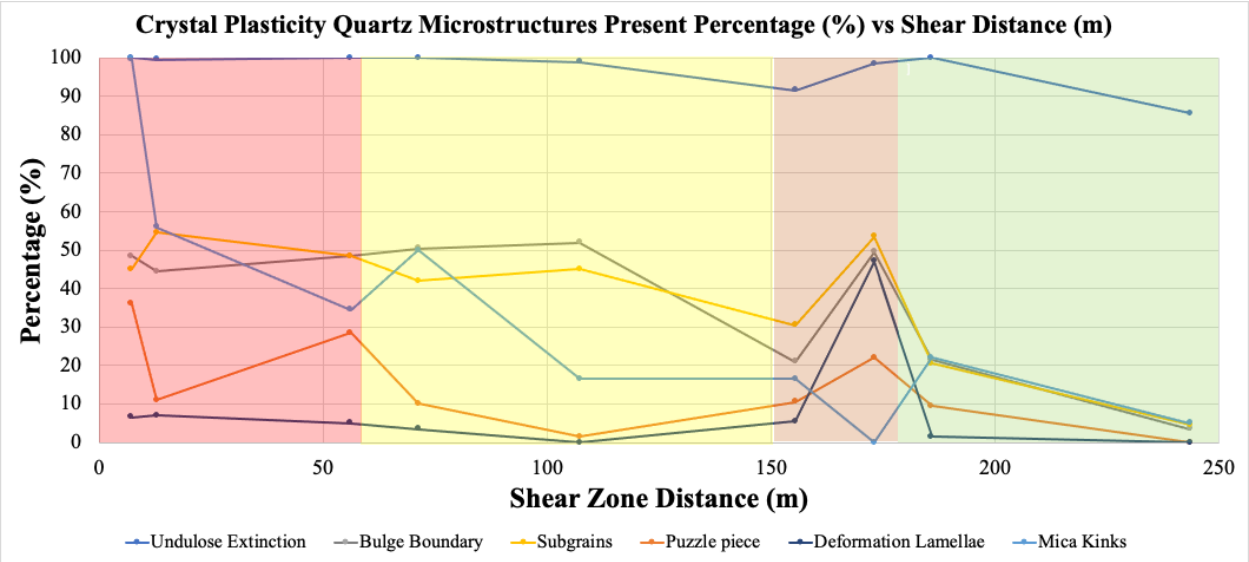

Figure 38: Crystal Plasticity Microstructures in the PdL vs. Distance (m) from the SISZ; plot of SI-83 to SI-106P.

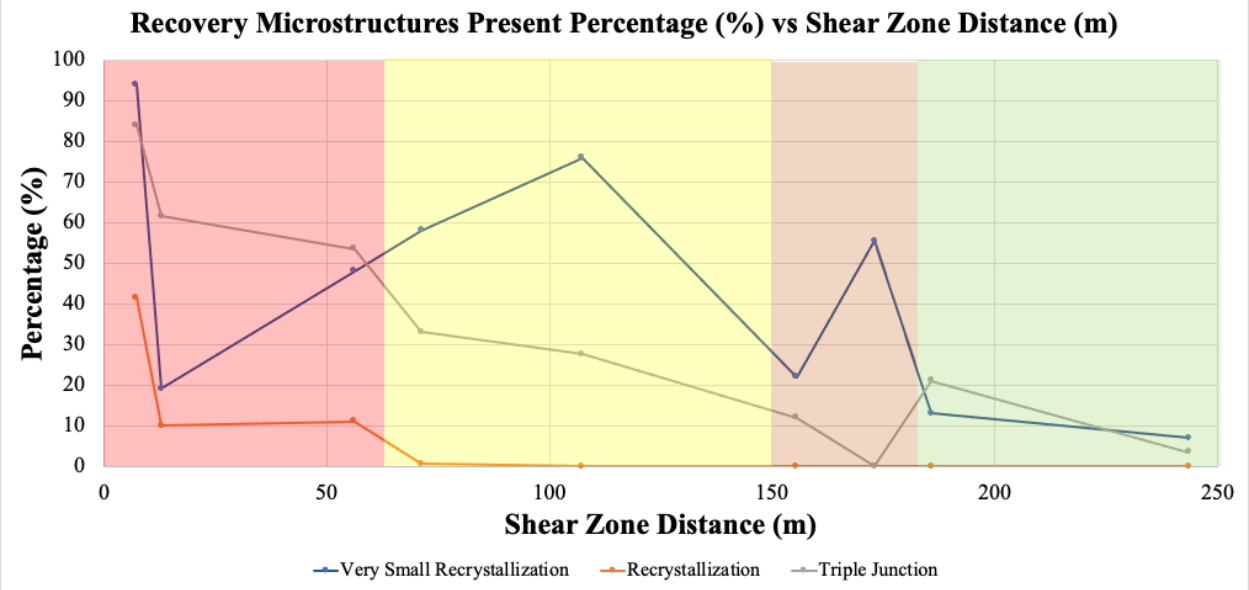

Figure 39: Recovery Microstructures in the PdL vs. Distance (m) from the SISZ; plot of SI-83 to SI-106P.

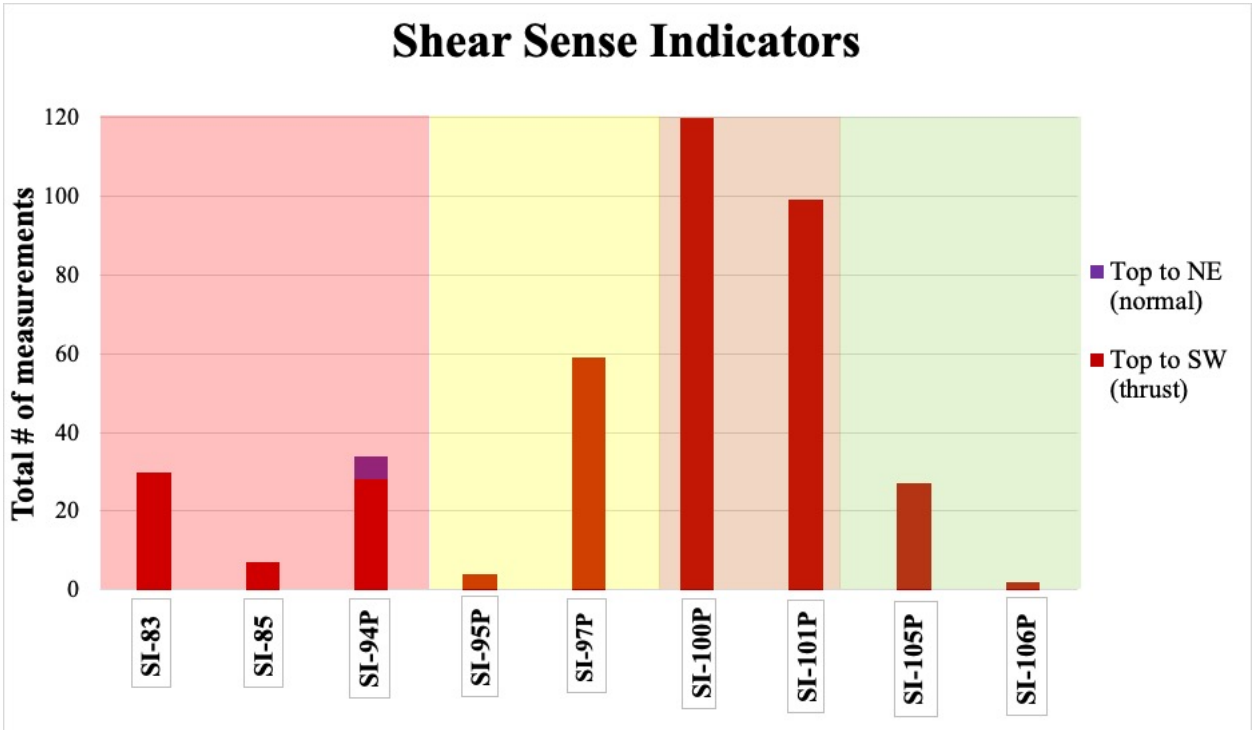

Figure 40: Top to SW (thrust) vs Top to NE (normal) sense of shear indicators for SI-83 to SI-106P.

4.4 Major element analysis

The mineral assemblage of the PdL metapelites are dominated by quartz, muscovite, and biotite along with some chlorite, albite and garnets throughout the range of metamorphism. Figure 41 shows an XRD plot of SI-82 which is a representative pattern indicating sample mineral assemblage.

The first suite of twenty samples from the 2018 field campaign and one sample from the 2020 field campaign were plotted on Harker diagrams to distinguish samples suitable for further geochemical analysis (Figure 42, Table 3). Three distinct groups were identified in the results: low, intermediate, and high silica (Figure 43-45). The intermediate silica group are best for further analysis. This is because in the low silica group, the rocks may have been contaminated with rocks from the metabasites. The high silica group are not useful because they are primarily quartzite without significant changes in geochemistry throughout the unit.

Ten samples plotted within the intermediate group, and these were plotted versus distance from the SISZ and compared to qualitative strain magnitude, determined by the degree of fabric formation. There is no data in the tan and green zones for the intermediate samples. Several of the major elements show a pattern with strain. Na_2O and Ti_2O increase with increased distance from the shear zone. K_2O and CaO decrease with increased distance from the shear zone. In particular the K_2O and CaO decrease appears to localize at the high to intermediate strain boundary (Figure 46).

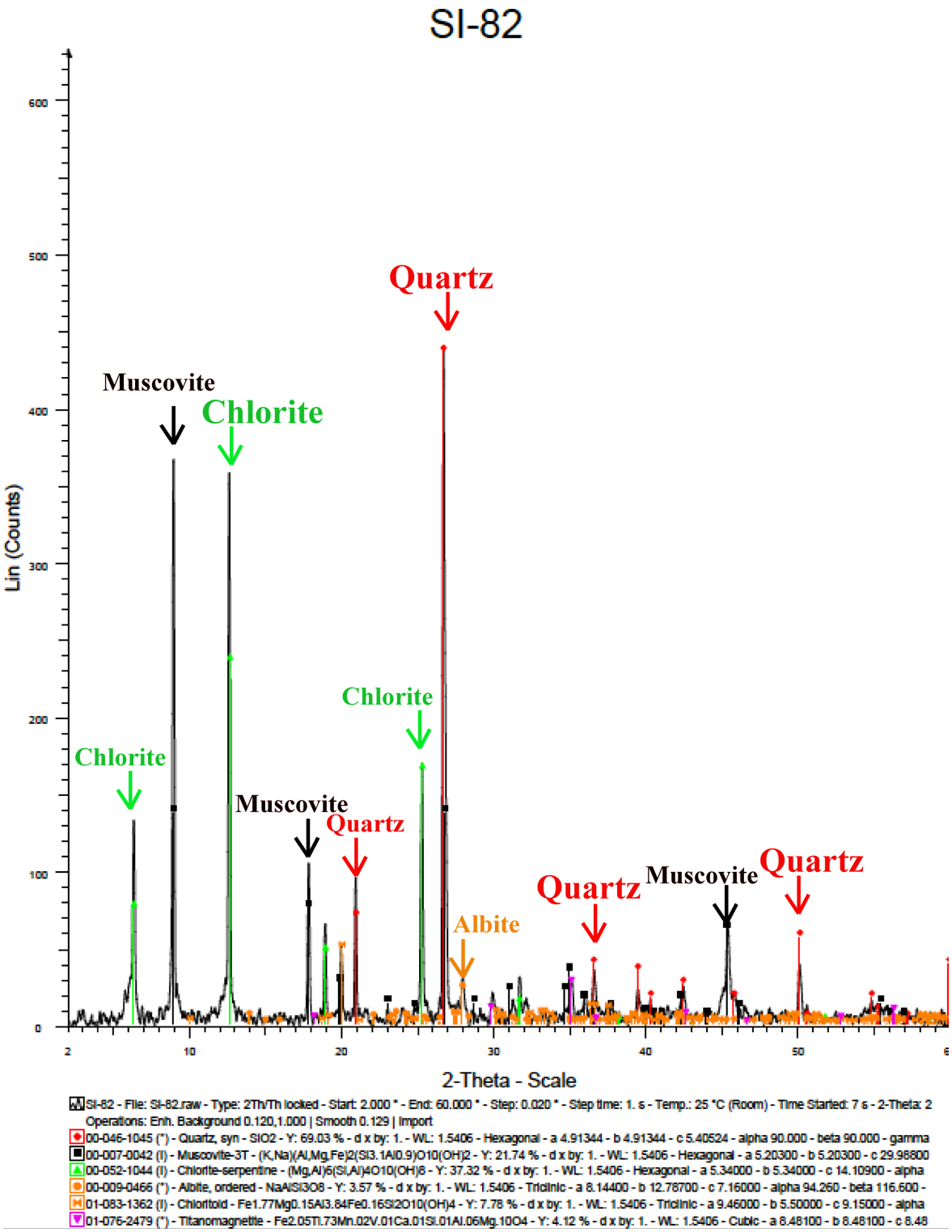

Figure 41: XRD pattern of SI-82 generated using the Bruker EVA software, showing representative mineralogy. This shows quartz (red), muscovite (black), chlorite (green), and albite (orange).

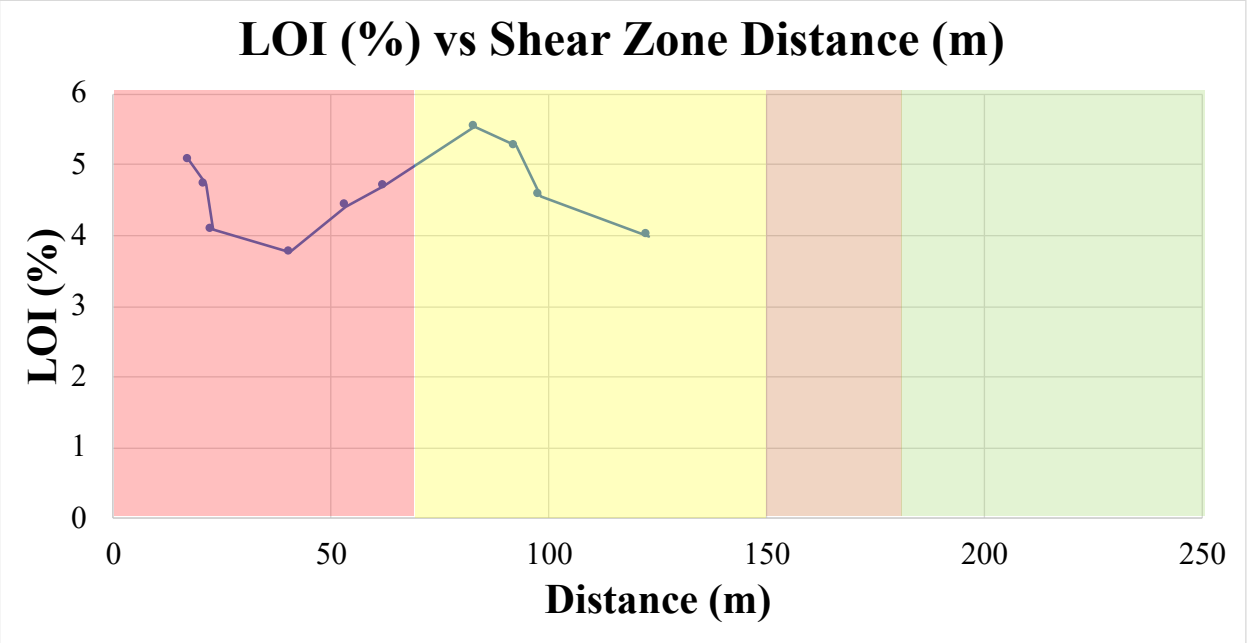

Figure 42: Showing variations in LOI (%) of the 2018 samples with respect to shear zone distance (m).

Table 3: X-Ray Fluorescence table of twenty-one PdL samples from Almonaster (2018 and 2020).

Sample ID	D'(m)	SiO2	TiO2	Al2O3	Fe2O3	MnO	MgO	CaO	Na2O	K2O	P2O5	LOI	Sum
PL-1	17.30	60.69	0.91	18.69	7.88	0.15	1.62	0.20	0.43	4.02	0.14	5.07	94.73
PL-2	21.20	61.04	0.87	18.02	6.84	0.21	1.43	0.31	0.50	3.90	0.10	4.72	93.22
PL-3	22.70	61.33	0.88	18.52	6.85	0.22	1.57	0.43	0.58	4.34	0.16	4.08	94.88
PL-4	26.60	65.12	0.76	16.30	6.08	0.15	1.62	2.04	2.55	2.24	0.14	2.72	97
PL-5	40.60	61.88	0.88	18.66	6.94	0.22	1.83	0.25	0.32	4.49	0.14	3.76	95.61
PL-6	51.50	51.84	0.93	18.63	12.29	0.22	5.49	0.04	0.05	3.08	0.06	6.17	92.63
PL-7	53.40	61.41	1.01	21.59	4.62	0.10	0.57	0.03	0.41	4.83	0.08	4.41	94.65
PL-8	55.20	68.84	0.83	14.23	7.22	0.11	0.83	0.03	0.24	2.83	0.16	4.10	95.32
PL-9	55.70	54.98	0.95	19.39	7.25	0.20	1.73	0.03	0.32	4.02	0.08	4.64	88.95
PL-10	57.70	71.77	0.72	14.14	5.08	0.12	0.92	0.03	0.19	2.94	0.07	3.29	95.98
PL-11	62.20	59.82	0.86	19.49	6.93	0.17	0.88	0.05	0.57	3.46	0.07	4.70	92.30
PL-12	65.50	67.02	0.78	15.85	6.48	0.12	1.13	0.04	0.35	2.85	0.07	4.56	94.69
PL-13	68.10	51.98	1.14	26.42	6.51	0.06	0.17	0.13	0.92	4.95	0.09	5.72	92.37
PL-14	76.40	68.84	0.70	15.37	4.80	0.08	0.46	0.09	0.41	2.34	0.05	4.87	93.14
PL-15	82.90	61.44	0.95	17.03	8.13	0.07	1.84	0.04	0.20	2.82	0.17	5.54	92.69
PL-16	92.40	60.21	1.02	17.52	7.88	0.15	2.38	0.10	0.40	2.68	0.13	5.26	92.47
PL-17	98.00	61.70	1.17	19.56	5.32	0.04	0.55	0.06	0.73	3.45	0.07	4.56	92.65
PL-18	122.80	61.31	1.03	20.34	6.58	0.09	0.62	0.24	0.88	2.15	0.09	4	93.33
PL-19	171.10	57.00	0.99	18.80	6.77	0.04	1.08	0.03	0.38	3.94	0.10	4.29	89.13
PL-20	192.60	54.21	1.08	24.17	6.62	0.07	1.10	0.08	0.70	4.55	0.08	4.44	92.66
SI-82	>400	55.53	0.97	21.74	8.02	0.06	1.28	0.23	0.55	3.46	0.05	4.91	91.94

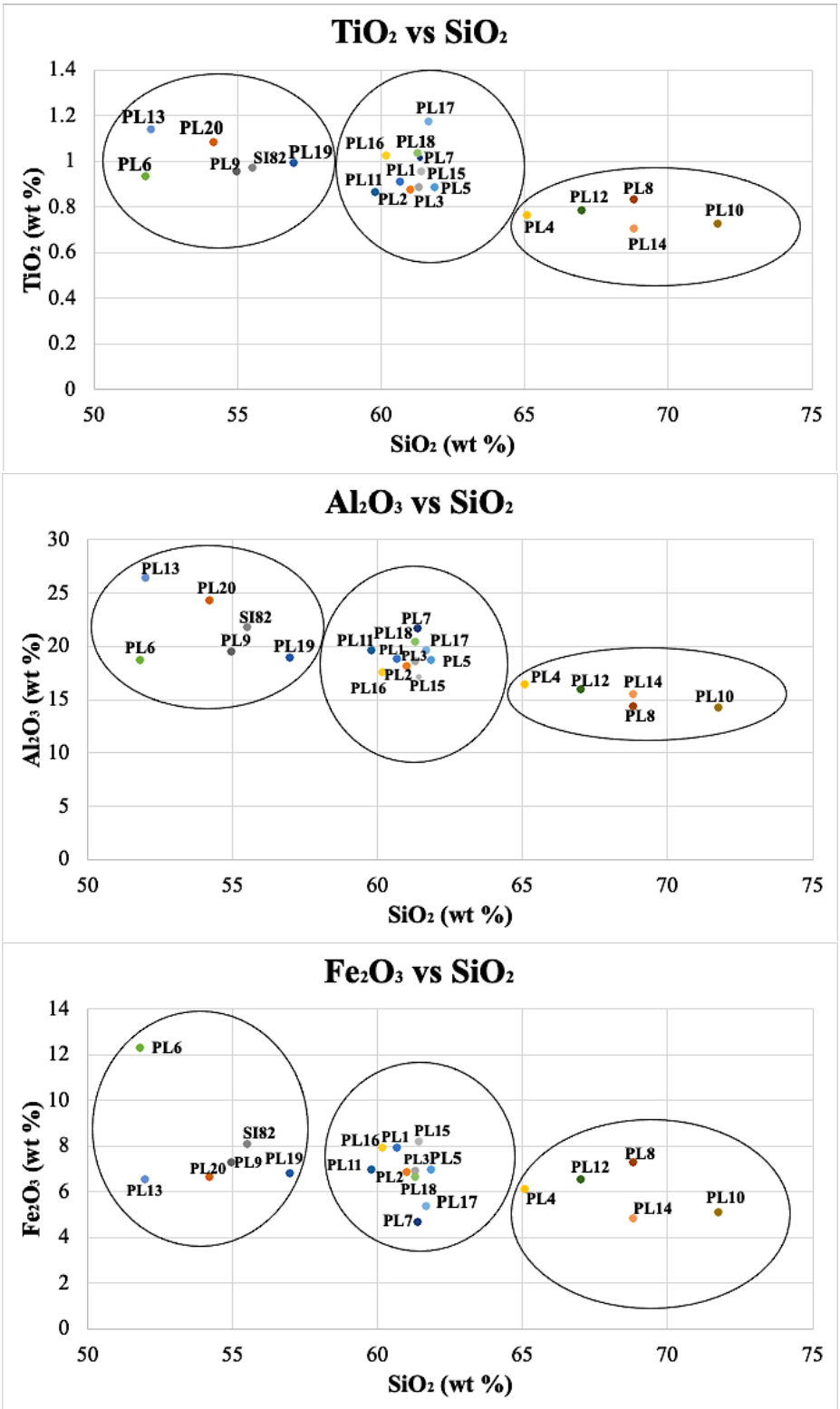

Figure 43: Harker diagrams of PdL samples in Almonaster showing variations of TiO_2, Al_2O_3, and Fe_2O_3.

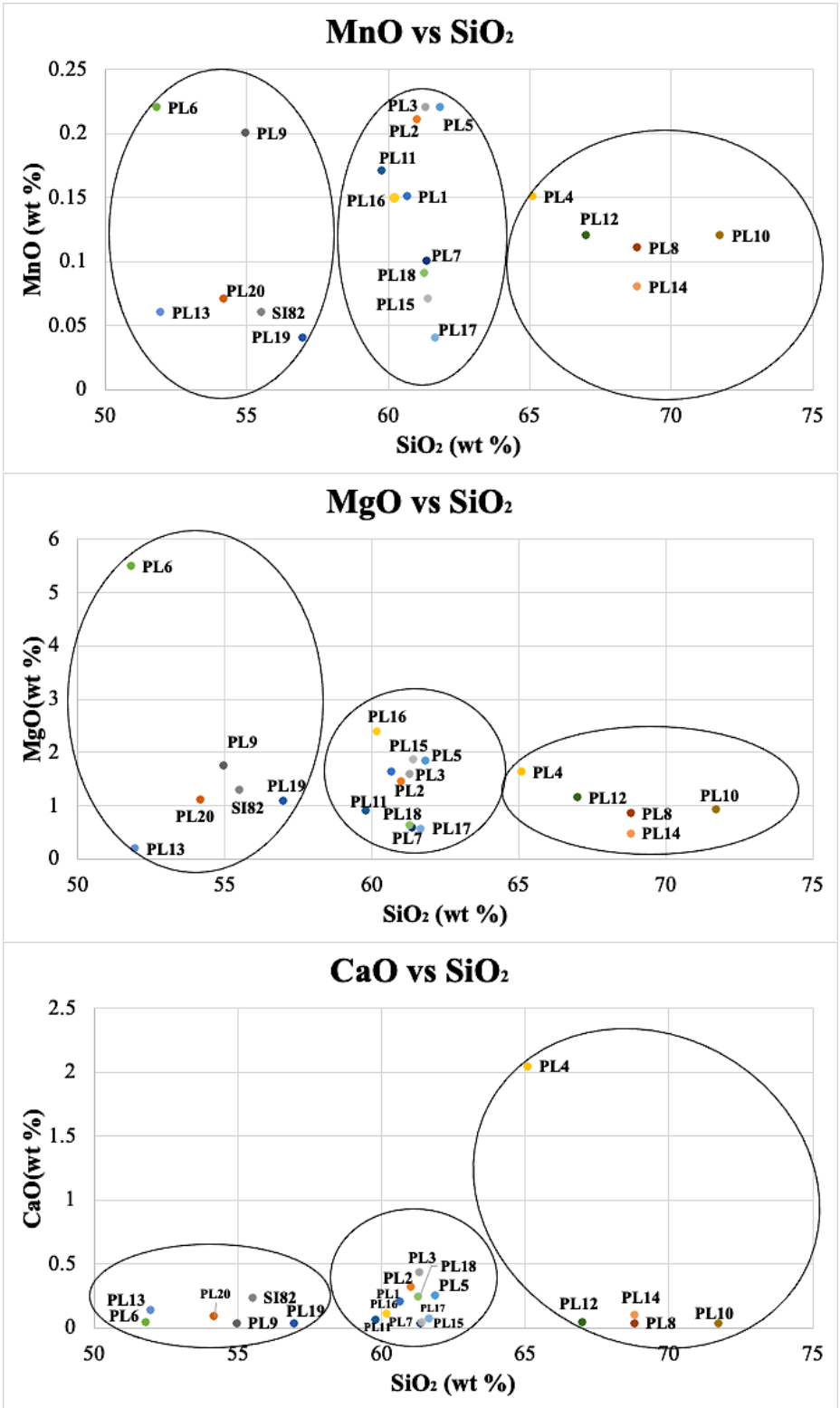

Figure 44: Harker diagrams of PdL samples in Almonaster showing variations of MnO, MgO, and CaO.

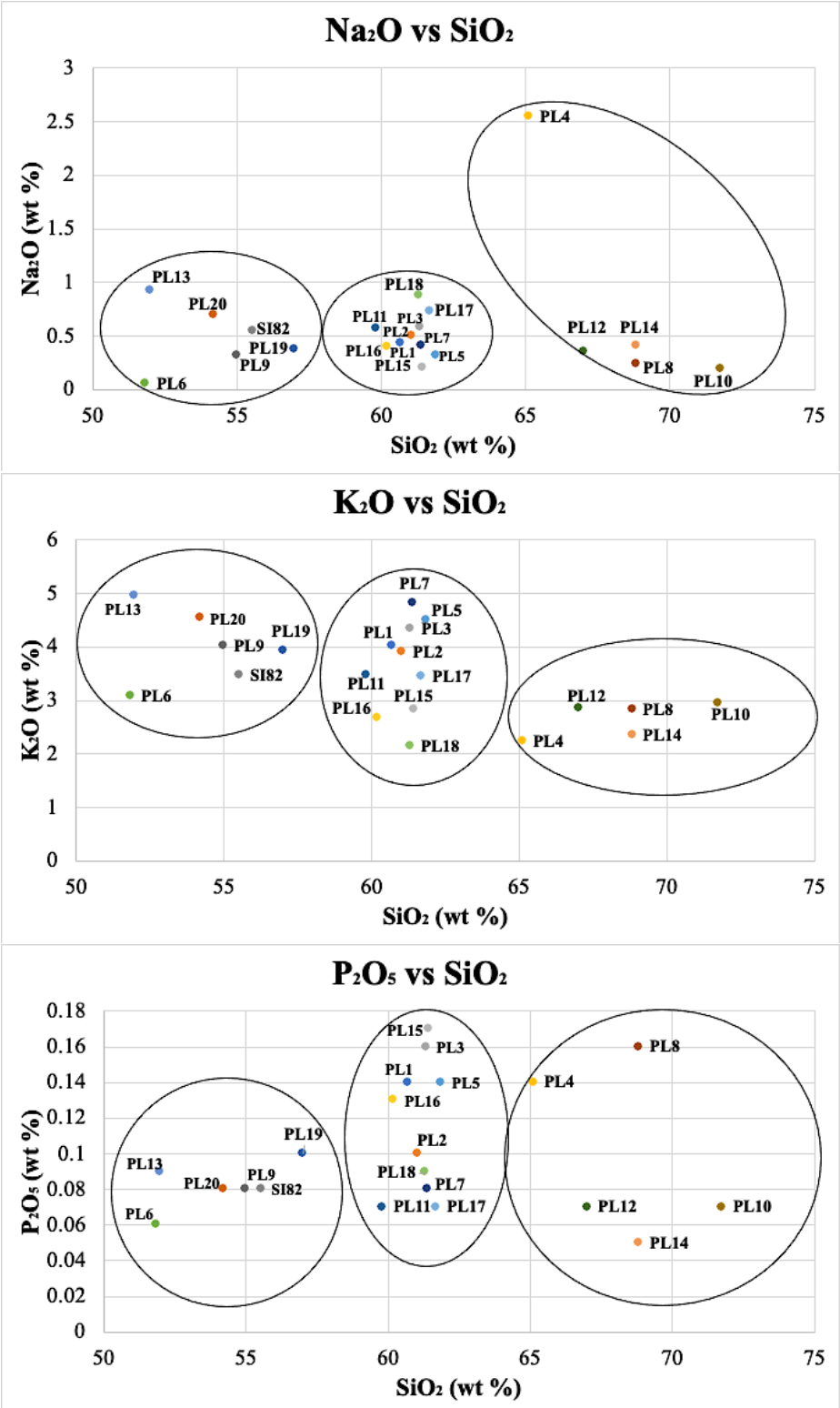

Figure 45: Harker diagrams of PdL samples in Almonaster showing variations of Na_2O, K_2O, and P_2O_5.

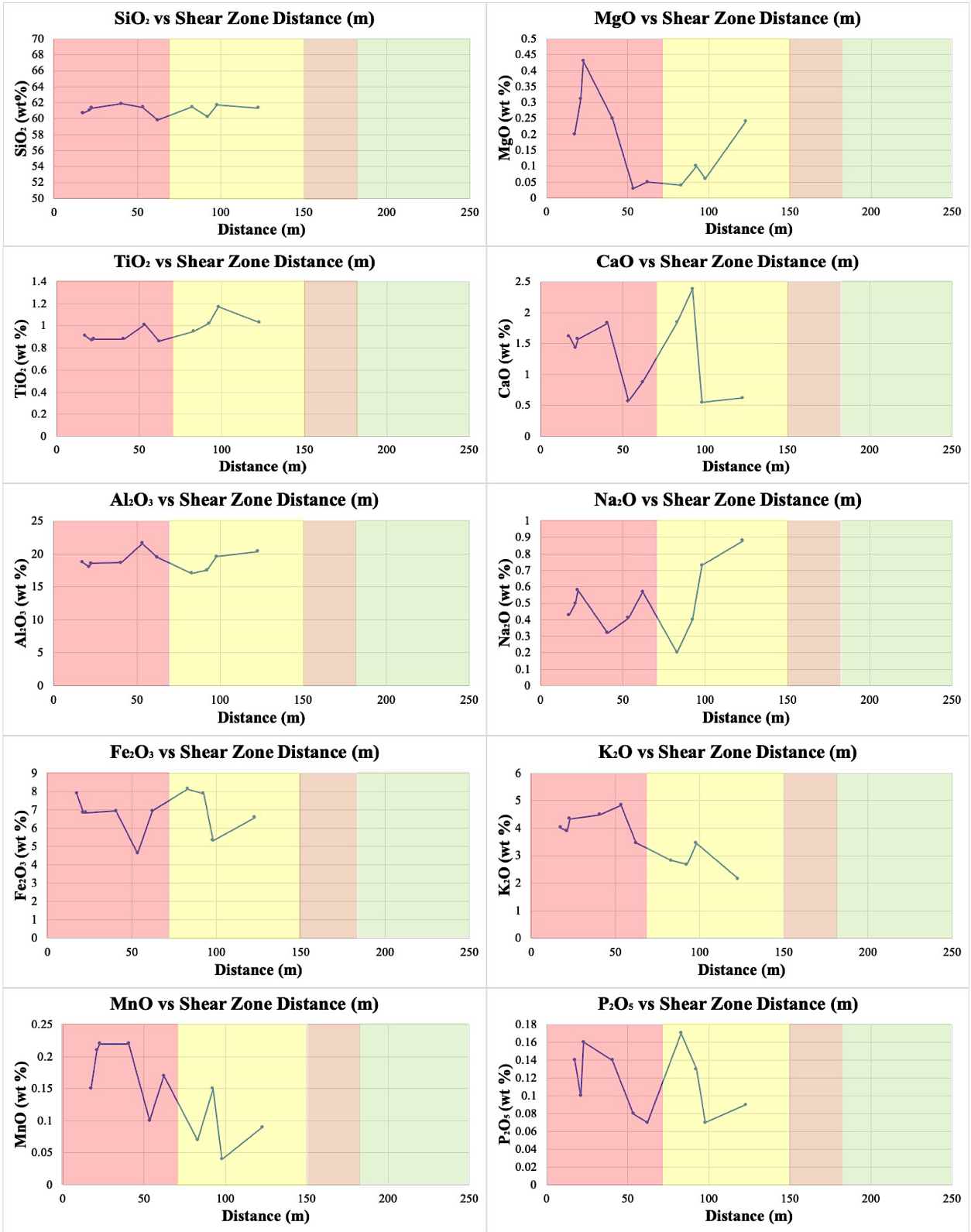

Figure 46: Major and minor elemental concentrations of the intermediate SiO_2 group of PdL samples from Almonaster plotted with respect to distance from shear zone.

Using the intermediate silica samples, we used two methods for isocon plots, the difference being in selection of the best protolith. In method 1, PL18 is designated the unaltered sample and compared to the rest of the intermediate silica samples. Using this method, we see enrichment of MgO and K_2O, depletion of Al_2O_3, and Na_2O, and no change in SiO_2, Fe_2O_3, MnO, CaO, TiO_2, and P_2O_5 (Table 4, Figure 47).

Table 4: Enrichment and depletion of elements for the Isocon method 1 & method 2

	Method 1	**Method 2**
Element	**Almonaster La Real**	**Almonaster La Real**
SiO2	N/A	N/A
TiO2	N/A	N/A
Al2O3	N/A	N/A
Fe2O3	N/A	E
MnO	N/A	E
MgO	E	E
CaO	N/A	E
Na2O	D	D
K2O	E	E
P2O5	N/A	N/A

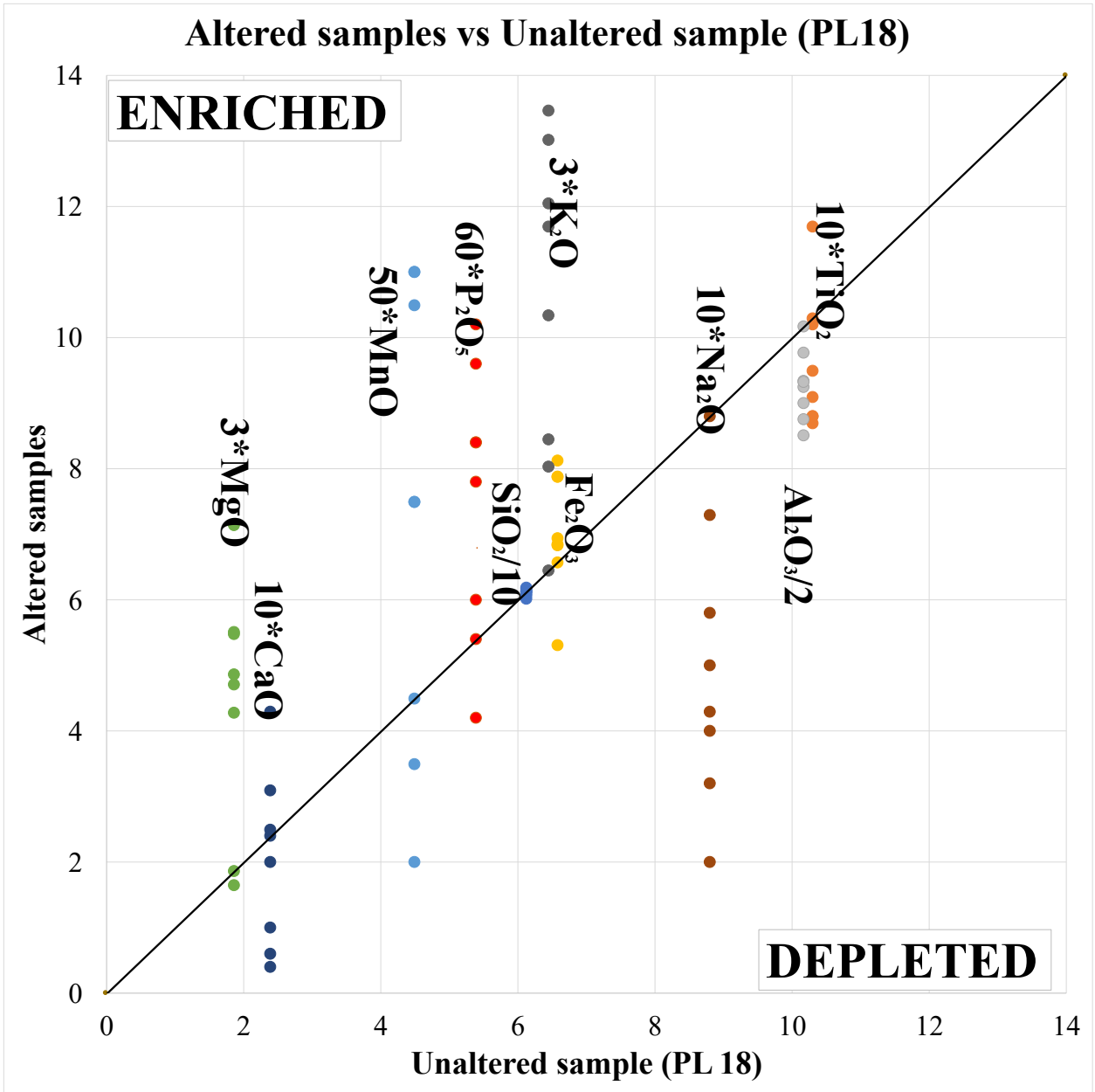

Figure 47: Isocon plot of the intermediate SiO_2 group of PdL samples from Almonaster. Method 1: PL-18 (furthest from shear zone) assigned as the unaltered (best protolith) sample.

In method 2, we used the average of PL15, PL16, PL17, and PL18 as the unaltered sample and compared this average to the rest of the intermediate silica samples. In method 2, this yielded apparent enrichment in MnO, MgO, CaO and K_2O, depletion of TiO_2 and Na_2O, and no trends in SiO_2, Al_2O_3, Fe_2O_3, and P_2O_5 (Table 4, Figure 48).

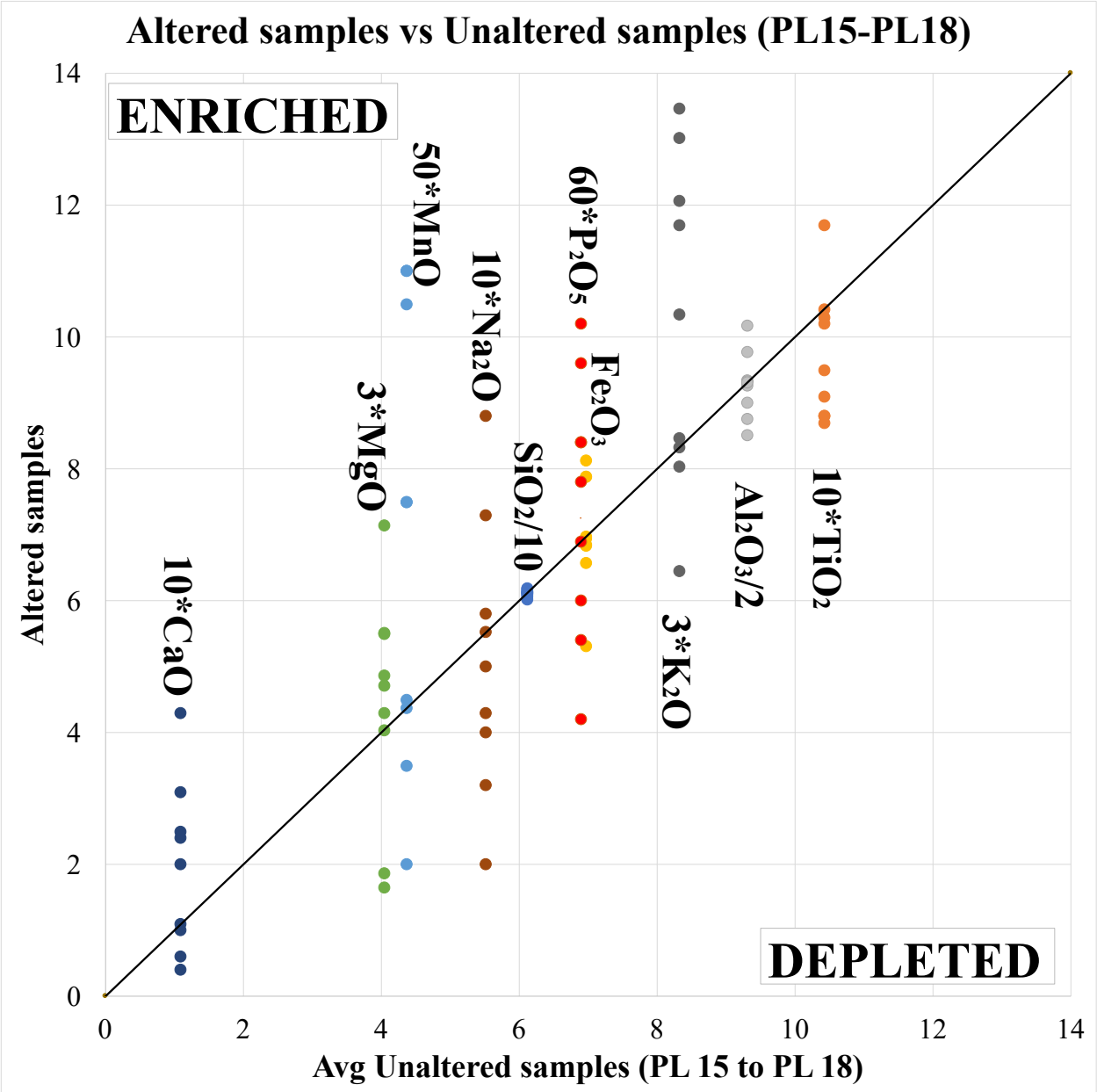

Figure 48: Isocon plot of the intermediate SiO_2 group of PdL samples from Almonaster. Method 2: assigned the average of four samples (PL-15, PL-16, PL-17, and PL-18) as a representative protolith to compare against all samples.

4.5 Vorticity Analysis

The same nine thin sections were used for vorticity analysis. The S-C-C' fabric orientations were determined for each thin section, being careful to observe these fabrics away from large porphyroclasts as they may locally deflect fabrics. We measured a total of ten C-C' angles, distributed throughout the thin section to determine the average vorticity (Appendix 9.4).

Average vorticities for the nine thin sections are plotted versus distance from the SISZ. In the high strain zone, the average vorticity ranges from 0.78 to 0.98 (Figures 49-51). In the intermediate strain zone, the average vorticity ranges from 0.68 to 0.90 (Figures 52-54). In the low strain zone, the average vorticity ranges from 0.86 to 0.97 (Figures 55-57). Vorticity does not vary across the transect (Table 5, Figure 58). Overall, seven of the nine values are consistent with simple shear dominated transpression (W_n>0.81), and the others are close.

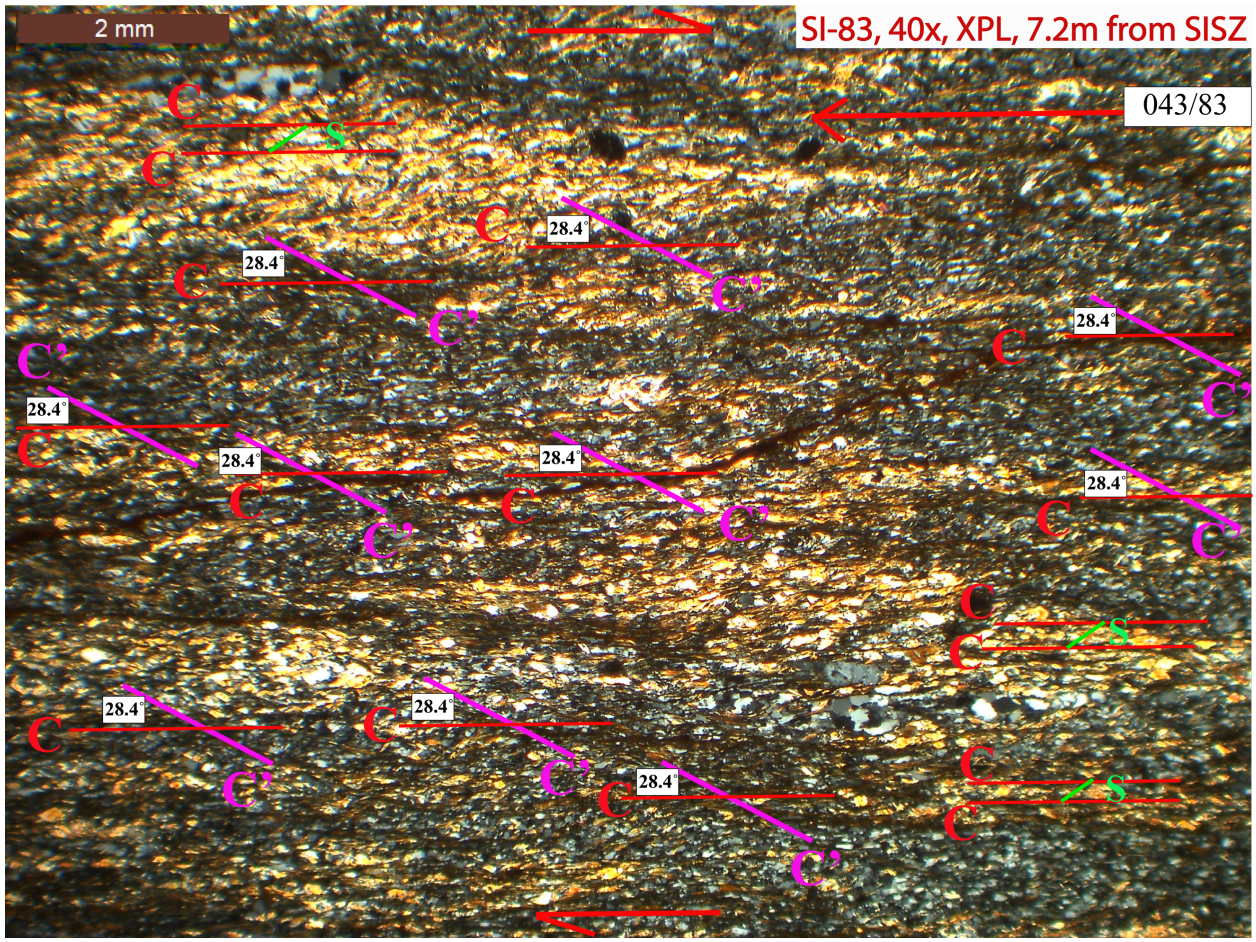

Figure 49: Observed SC fabric and measured angle between C'& C to estimate the vorticity of SI-83.

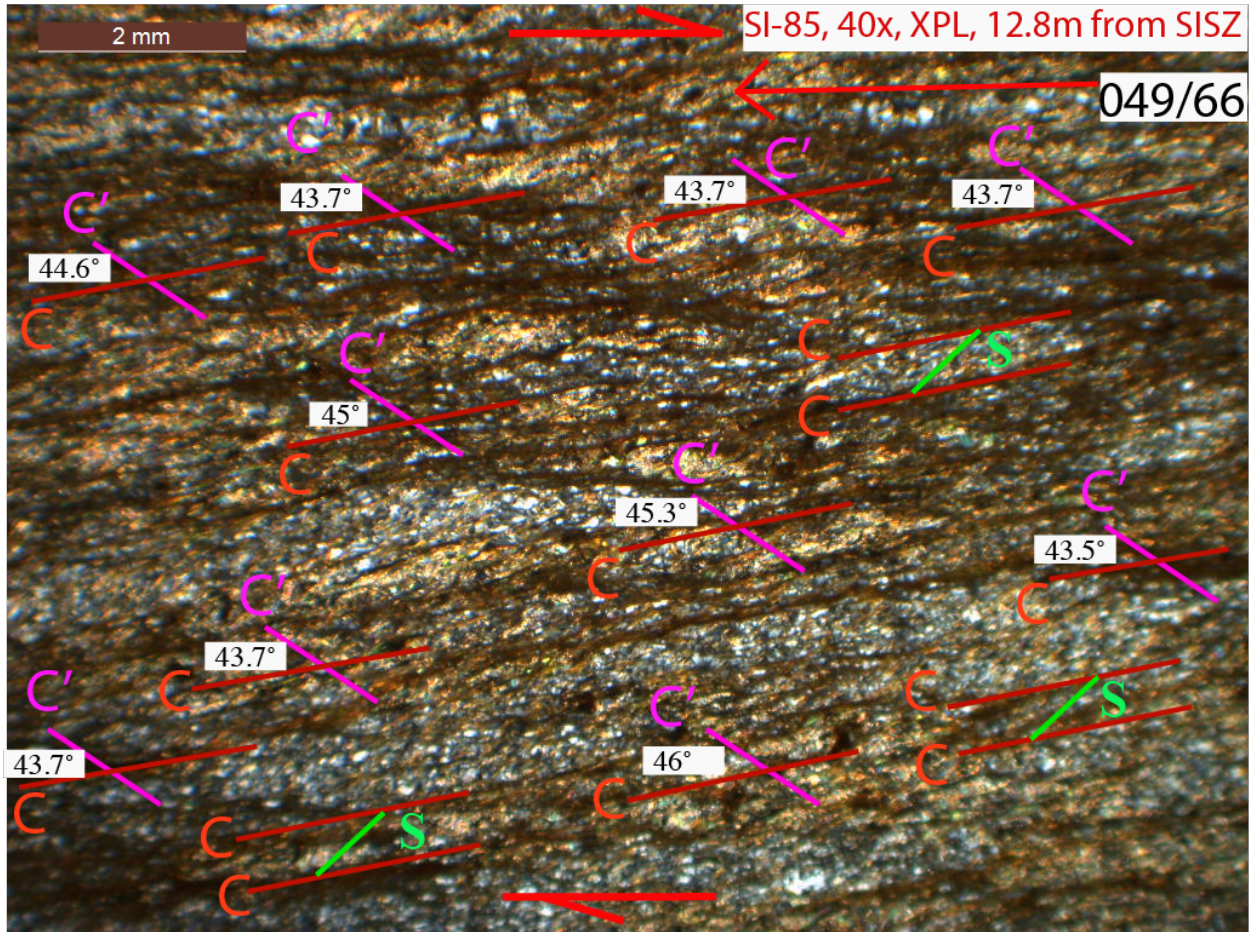

Figure 50: Observed SC fabric and measured angle between C'& C to estimate the vorticity of SI-85.

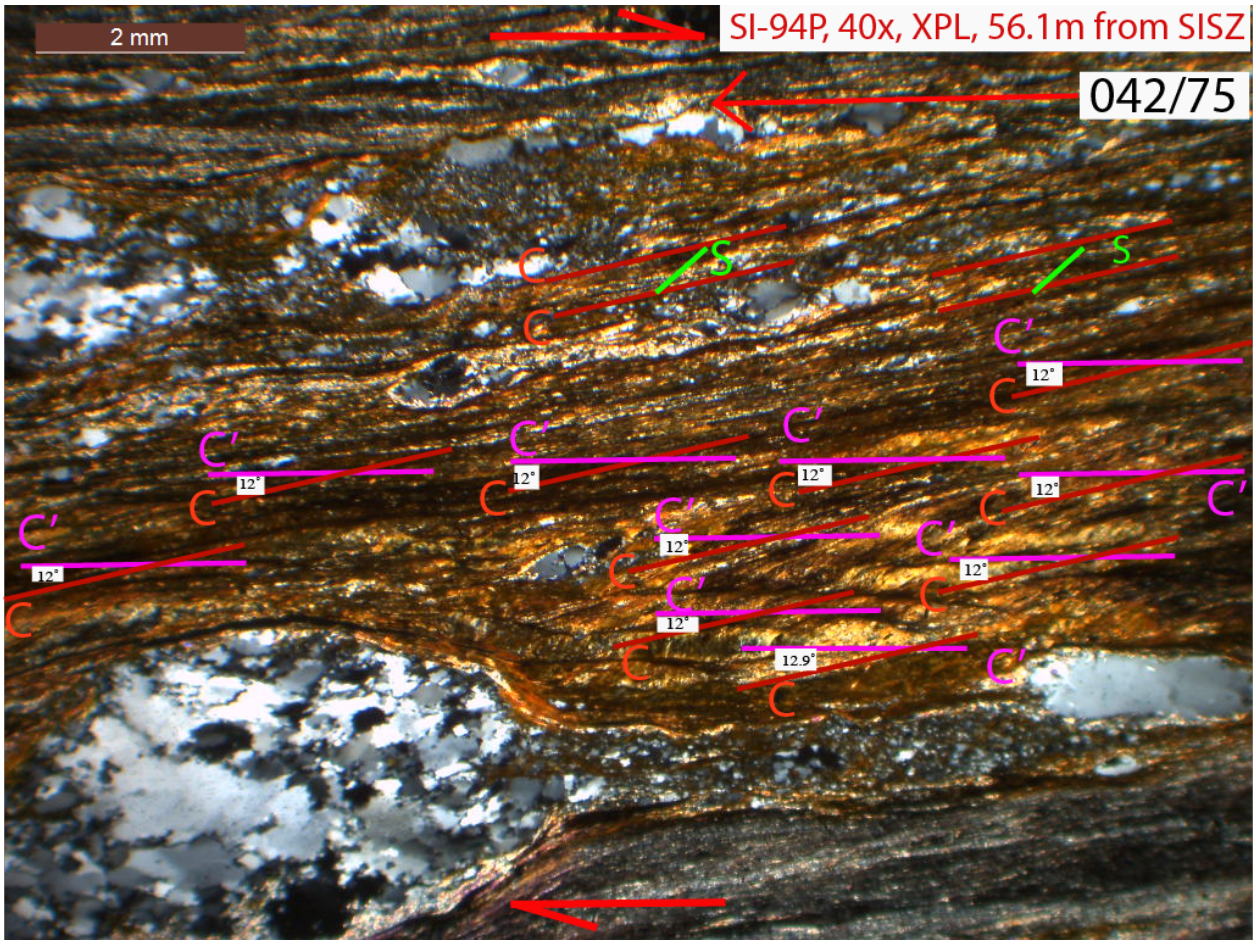

Figure 51: Observed SC fabric and measured angle between C'& C to estimate the vorticity of SI-94P.

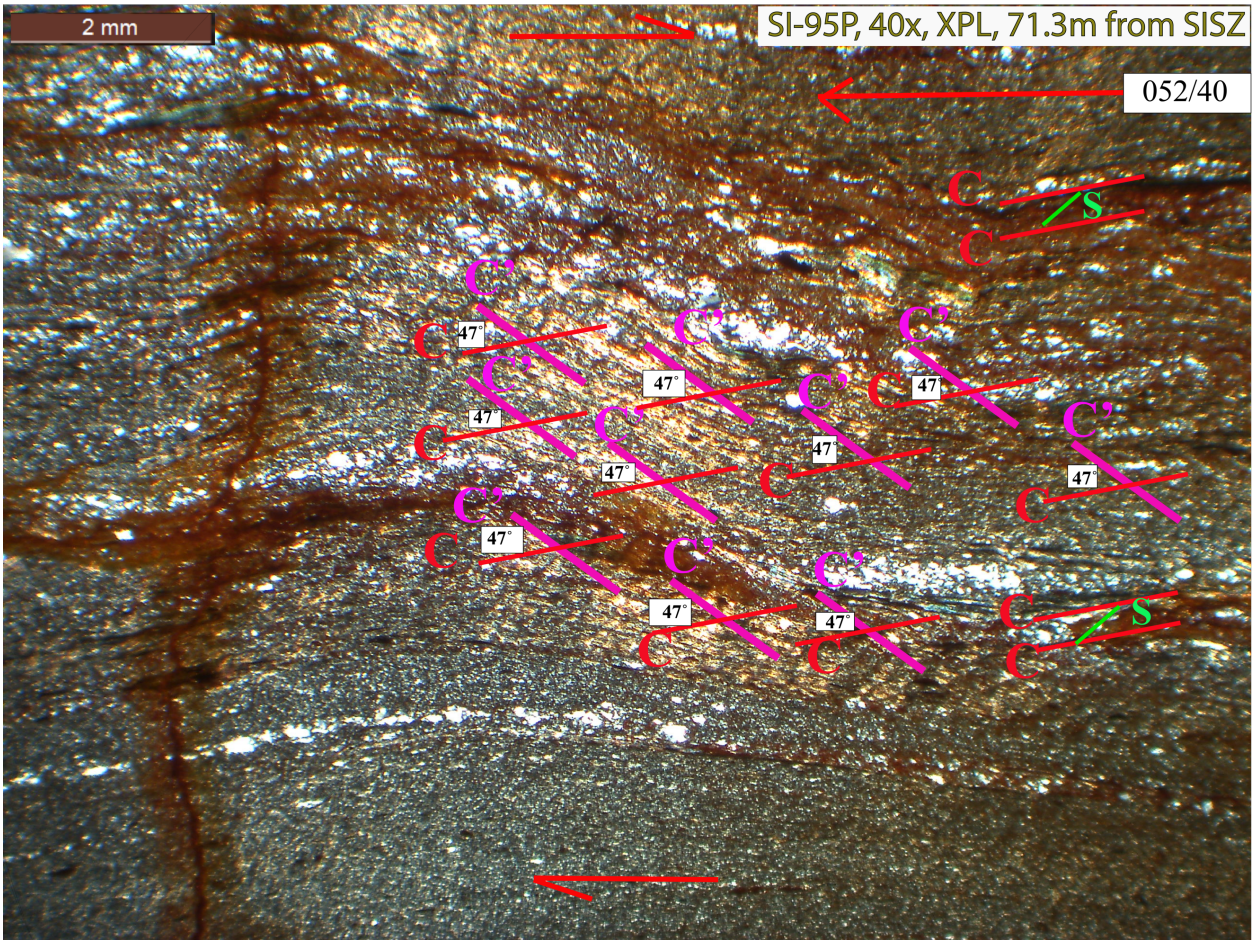

Figure 52: Observed SC fabric and measured angle between C'& C to estimate the vorticity of SI-95P.

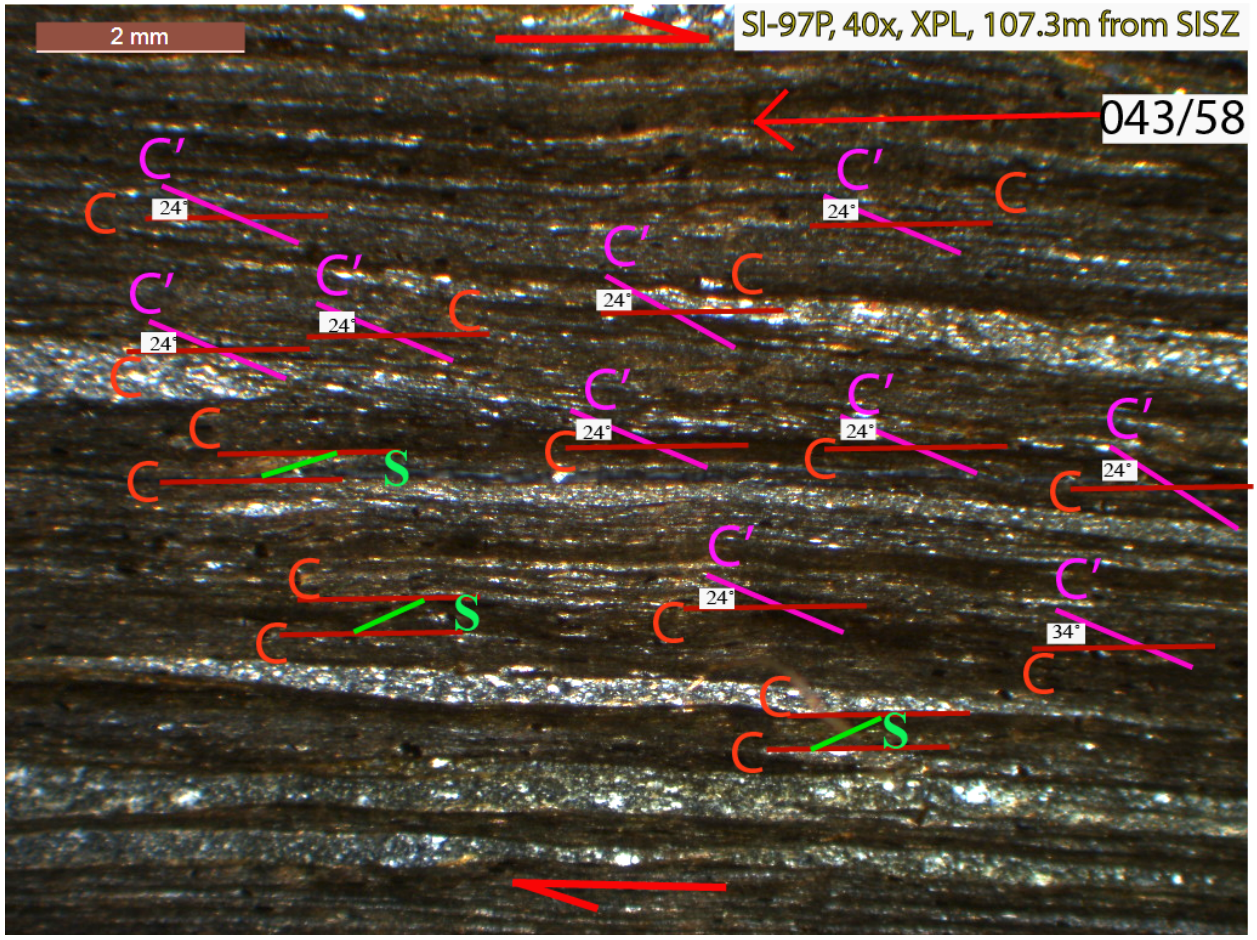

Figure 53: Observed SC fabric and measured angle between C'& C to estimate the vorticity of SI-97P.

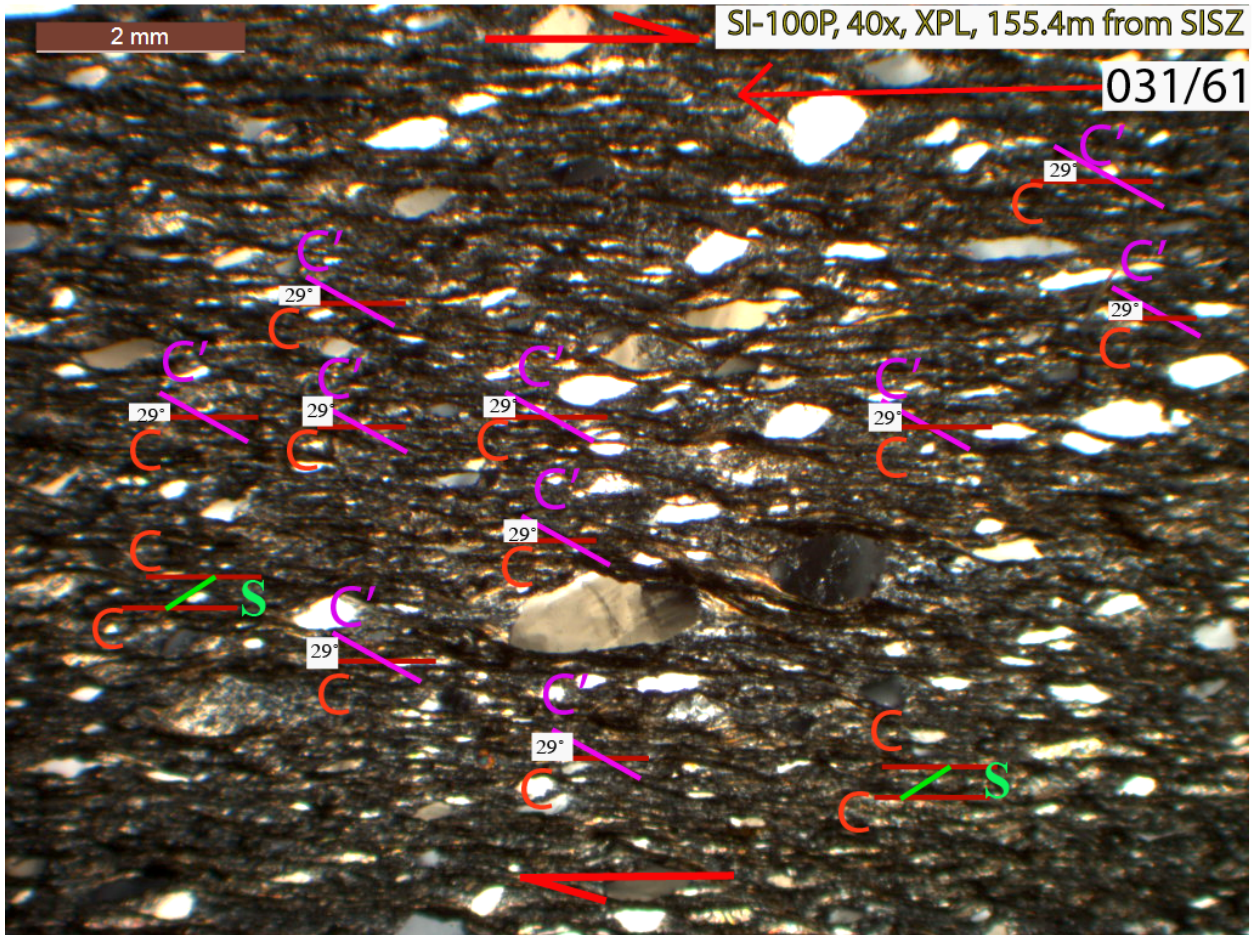

Figure 54: Observed SC fabric and measured angle between C'& C to estimate the vorticity of SI-100P.

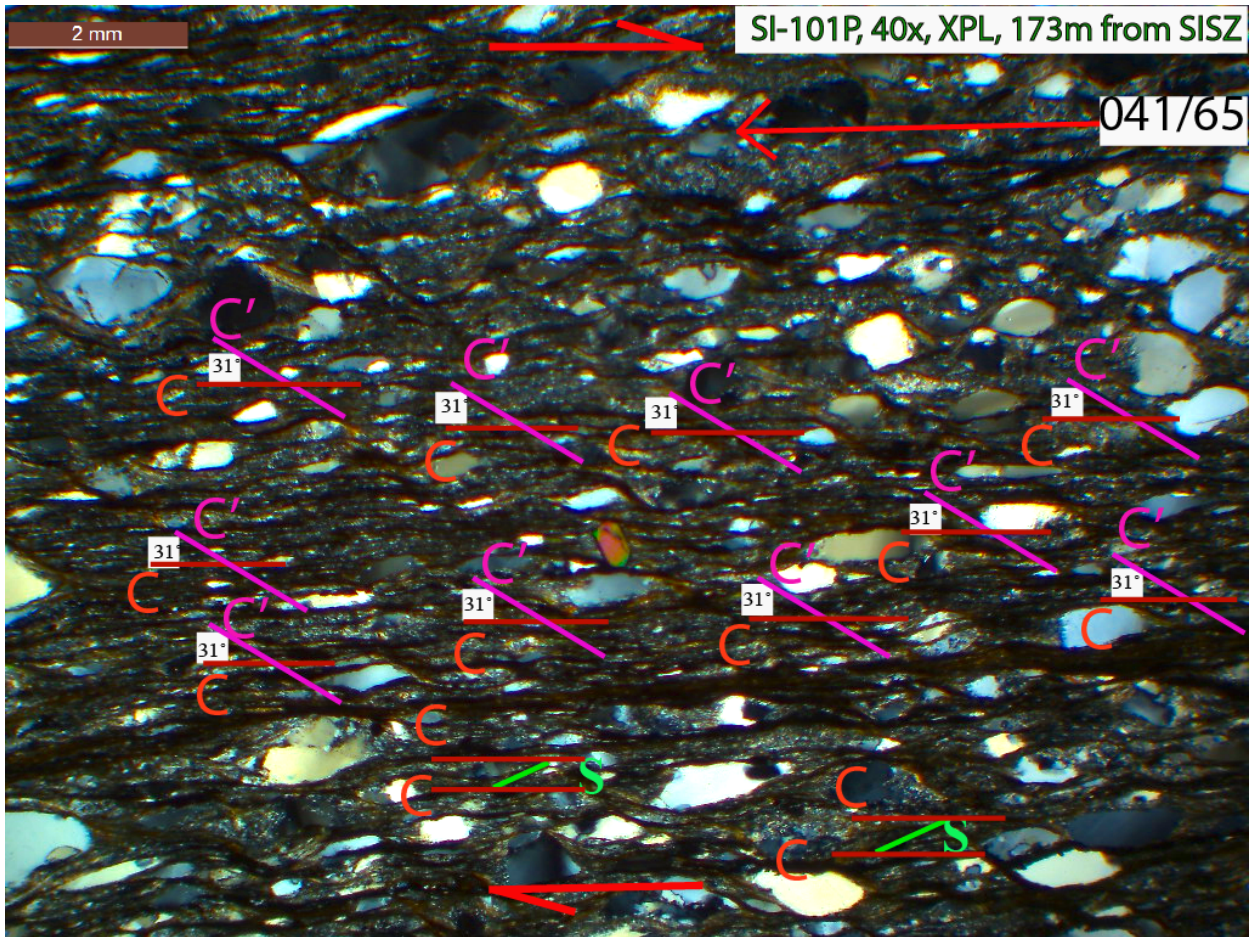

Figure 55: Observed SC fabric and measured angle between C'& C to estimate the vorticity of SI-101P.

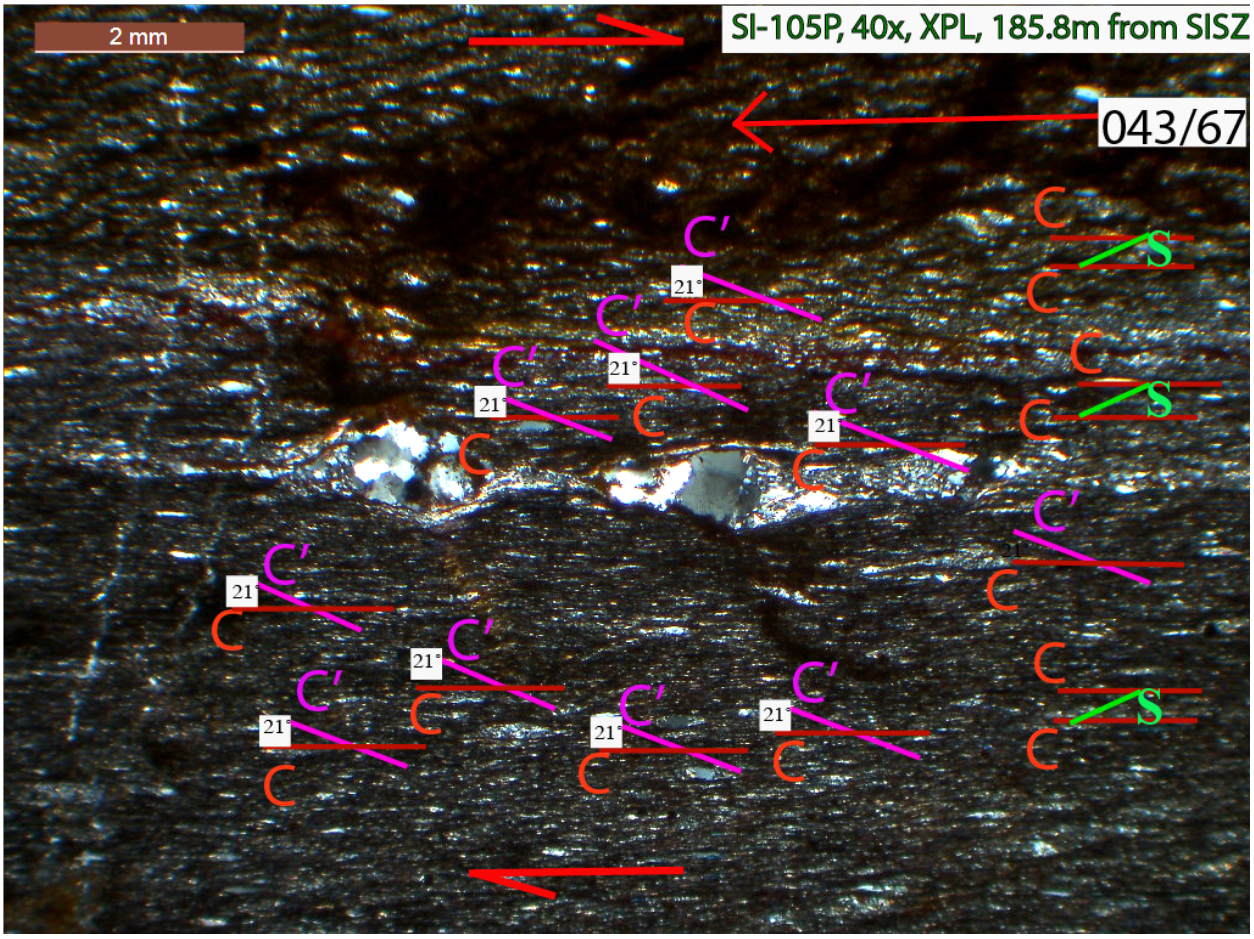

Figure 56: Observed SC fabric and measured angle between C'& C to estimate the vorticity of SI-105P.

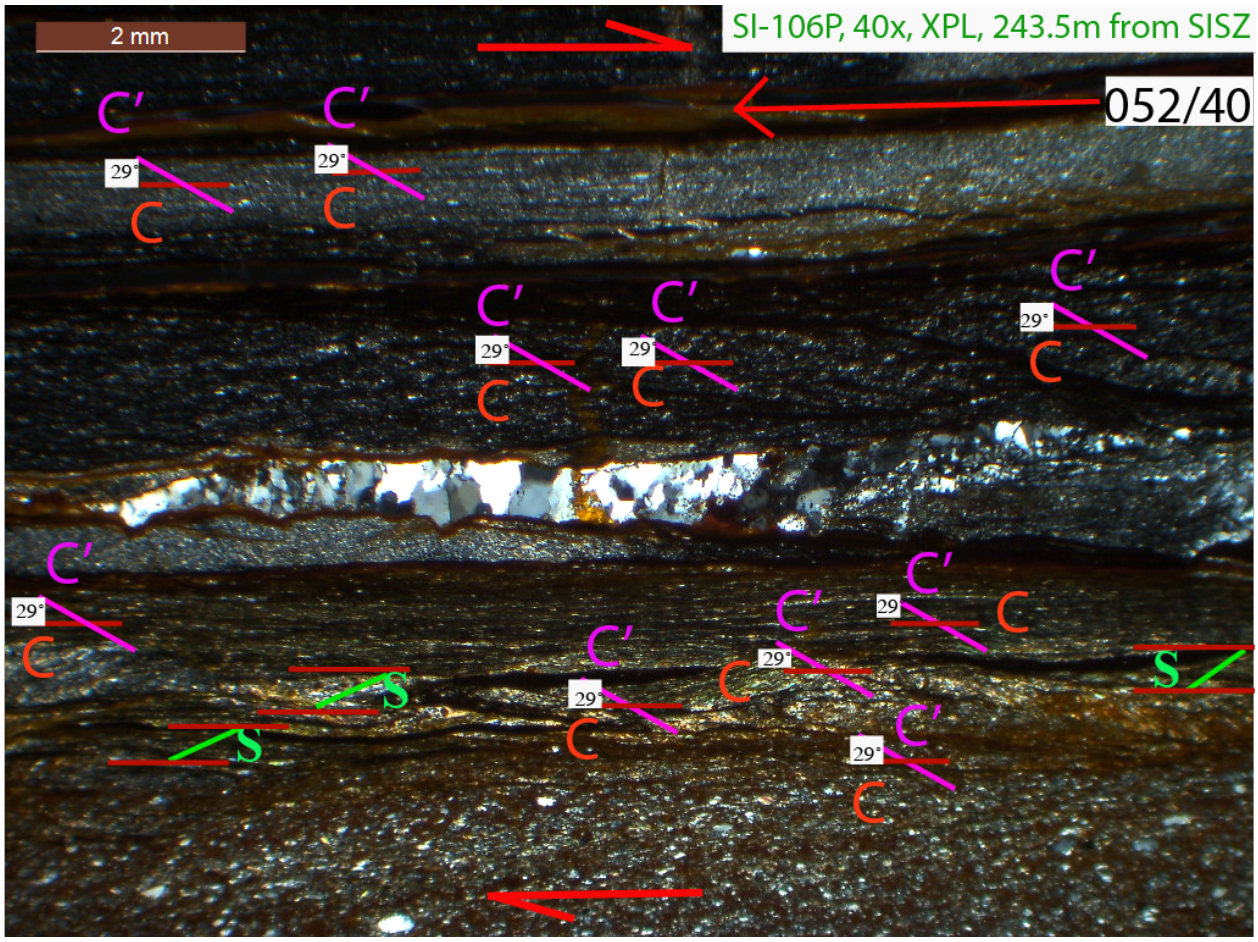

Figure 57: Observed SC fabric and measured angle between C'& C to estimate the vorticity of SI-106P.

Table 5: Maximum vorticity values were determined for SI-83 to SI-106P.

Transect	Sample ID	Distance (m)	Max Vorticity (Wn)	Average Vorticity (Wn)	Vorticity Ranges
Almonaster	SI-83	7.2	0.88	0.88	0.88
Almonaster	SI-85	12.8	0.73	0.72	0.69-0.73
Almonaster	SI-94P	56.1	0.98	0.98	0.98
Almonaster	SI-95P	71.3	0.68	0.68	0.68
Almonaster	SI-97P	107.3	0.91	0.90	0.83-0.91
Almonaster	SI-100P	155.4	0.87	0.87	0.87
Almonaster	SI-101P	173	0.86	0.86	0.86
Almonaster	SI-105P	185.8	0.93	0.93	0.93
Almonaster	SI-106P	243.5	0.87	0.87	0.87

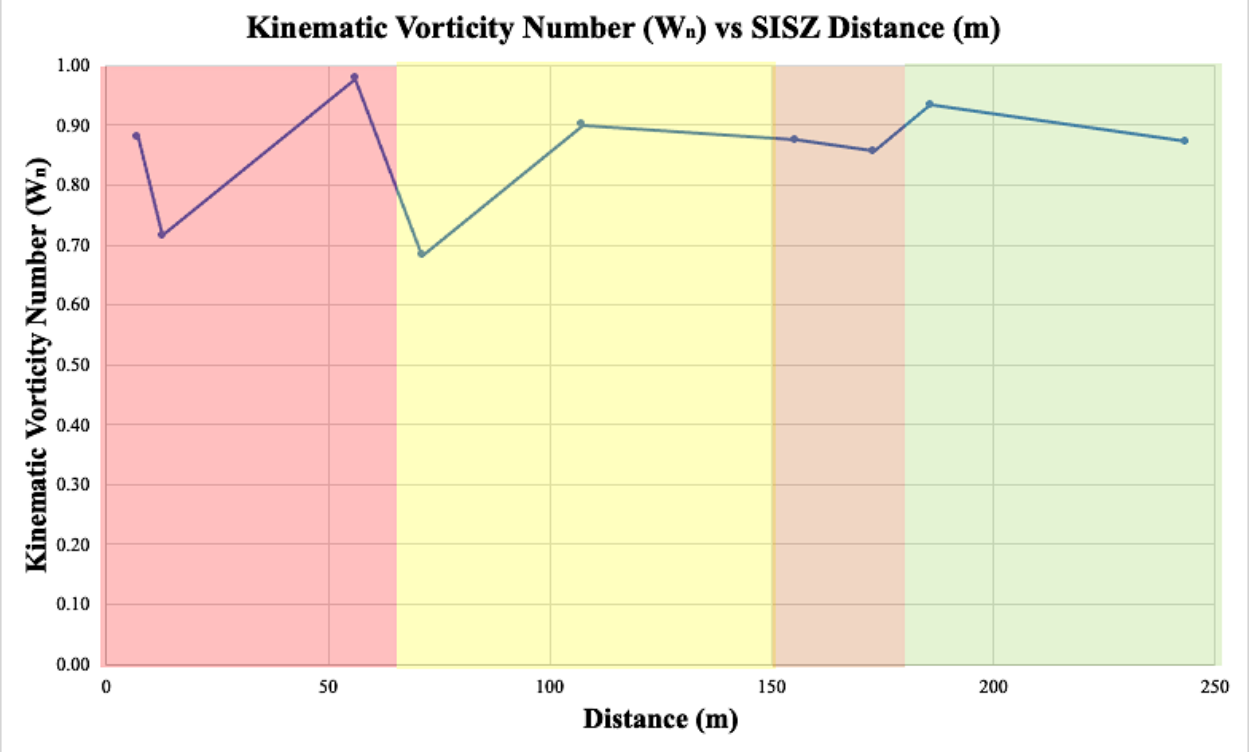

Figure 58: Average kinematic vorticity number versus shear zone distance (m) of the 9 PdL samples.

CHAPTER 5: Discussion

5.1 Interpretation of Metamorphic and Strain Gradient

At the regional scale, the SISZ took advantage of the rheological contrasts between the Beja Acebuches Metabasites and metasedimentary rocks of the Pulo do Lobo. However, other factors played a role in localization at the meter to decameter scale within the PdL Formation along the Almonaster transect. Within the 150 meter transect, fabric strength and metamorphic grade increase toward the shear zone contact. The highest strain and metamorphic grade is seen closest to the shear zone (0-65 m). The metamorphic grade closest to the shear zone (<20 m) is amphibolite facies (garnet zone) which is evident by the mineral phases including garnet, potential Ca rich plagioclase, and extensive muscovite. Although it should be noted that minerals like chlorite, characteristic of lower metamorphic grades are also found. This zone has the strongest fabrics with closely-spaced schistose foliations.

The intermediate strain zone (65-171 m), consists of phyllites, interpreted to be upper greenschist facies indicated by dominance of biotite. It has heterogeneous deformation observed by the complex geometries such as S-C fabric, shear bands, etc.

The lowest strain zone (>172 m) is presumably unaffected by the SISZ and consists of slates at low-mid greenschist facies. Foliations are slaty and consistent with the regional foliations in the neighboring PdL unaffected by the SISZ.

This metamorphic grade in the PdL is heavily localized around 105m away from SISZ with comparison to the much broader localization of retrograde metamorphic reactions in the BAM. This suggests that hydrothermal fluids localized along the SISZ. The heat caused an extremely localized prograde increase in metamorphic grade and fluid acting as a catalyst to metamorphic reaction. This hydrothermal fluid effect can explain the contrast between the garnet

zone metamorphism close the SISZ and peak metamorphism within most of the PdL which reached greenschist facies with temperatures of 400-450° C and pressure of 2 kbar pressure (Ábalos et al., 2002). The metamorphic reactions along the SISZ likely promoted strain softening through generation of weaker mineral phases like extensive muscovite.

5.2 Microstructures

Microstructures throughout the transect indicate that all three groups of deformation mechanisms: brittle, DMT, and crystal-plasticity were active across the entire strain gradient. This is not unusual in shear zones at greenschist and amphibolite facies, especially those with complex mineral assemblages (e.g., Yonkee et al., 2013).

The microstructures indicating crystal-plasticity gradually increase with strain suggesting that dislocation creep was responsible for ongoing strain accumulation over the life of the SISZ. It is possible that the hydrothermal fluid, largely localized near the SISZ, enhanced crystal plasticity through hydrolytic weakening of quartz. Recovery accommodated by recrystallization is much more prominent in the high strain zone, and it is likely that this recrystallization is enhanced in the presence of a fluid.

DMT is also heavily concentrated adjacent to the SISZ within the entire high strain zone. This suggests that the syndeformational hydrothermal fluids were not channelized only in a narrow band of the SISZ but extended out at least through the high strain zone (65 m). DMT in the low-grade slates is likely due to initial dewatering of the metapelites during D1.

Brittle deformation is most localized right at the SISZ (<10 m) with extensive veining and fracturing. The coincidence of enhanced brittle deformation and concentrated fluid flow

along the shear zone suggests that fracturing could have been intermittently induced by high fluid pressures. Fracturing is a probable mechanism for cross shear zone fluid flow, as has been hypothesized within the BAM (Stephenson, 2018; Czeck et al., 2019).

The presence of fluid along the SISZ simultaneously or intermittently enhanced all three groups of deformation mechanisms. Combined with the strain softening metamorphic reactions, fluid created a positive feedback whereby fluids enhanced crystal plasticity and DMT, creating strong fabrics and fluid corridors along mica planes. Fluids also generated transient embrittlement which created pathways for more fluids to enter the rocks.

5.3 Interpretation of the major element compositional data

5.3.1 Selection of Protolith

Since an undeformed and unaltered protolith of the PdL does not exist, we tried two methods to choose our best protolith. In method 1, seven altered samples (closer to the SISZ) were compared against the one least altered sample furthest from the SISZ. Subsequently in method 2, four altered samples were compared against the average of the four unaltered samples furthest from the SISZ.

We decided that the average of a group of samples (Method 2) is better than using a single sample (Method 1) as our unaltered reference. This is due to the inherent geochemical variability of the PdL. Some elemental trends that seemed apparent in element versus distance plots were reflected in Method 2 average protolith isocon plot and not Method 1single protolith (such as CaO enrichment), supporting the use of Method 2.

5.3.2 Volume Change

Based on the degree of their geochemical distribution during alteration, the isocon plot indicates whether there is volume change due to depletion of mobile elements (Si) and enrichment of immobile elements (Al, Ti). In the PdL data, a straight 1:1 line fits through the elements that are assumed immobile. Their lack of enrichment combined with the lack of SiO_2 depletion is consistent with relatively constant volume alteration.

5.3.3 Geochemical variations

The most significant major element changes in the SISZ are enrichment in MgO, K_2O, and possibly CaO and decrease in Na_2O towards the SISZ.

The trends in Na and Ca may be related to plagioclase chemistry because Na-rich albite, which is stable at low temperatures below 500° C, may have been replaced by Ca-rich anorthite which is stable at high temperatures such as in the garnet zone. Metamorphism in the main area of the PdL only peaked at 400° - 450 C at 2kbar (Ábalos et al., 2002). Metamorphic grade typically does not vary this much within such a short distance without contact metamorphism or hydrothermal alteration, so this suggests that hydrothermal fluids increased the temperature locally near the SISZ and catalyzed metamorphic reactions in the PdL.

The increase of K_2O is most likely also due to fluid flow related to the SISZ. Within the BAM, Stephenson (2018) found unusually high K_2O and hypothesized that the source was from fluid that crossed from the PdL due to intermittent fracturing due to fluid-induced embrittlement. Within the PdL, the K may be located within muscovite and chlorite grains formed during metamorphism. The interaction between muscovite and aqueous fluid may form chlorite, which is present in the high strain zones SI-83 to SI-88 of the PdL (1).

[Muscovite] $2KAl_3Si_3O_{10}(OH)_2 + 3H_4SiO_4 + 9Fe^{2+} + 6Mg^{2+} + 18H_2O$ [fluid]= [chlorite] $3Mg_2Fe_3Al_2Si_3O_{10}(OH)_8 + 2K^+ + 28H^+$ [fluid] (1)

The source of K_2O enrichment near the PdL is potentially fluid released from either the PdL Formation or from another formation within the PdL Domain.

MgO (and possibly FeO, seen only in Method 2 isocon plot) is also enriched within the altered PdL. MgO (and possibly FeO) enrichment is consistent with hydrothermal alteration, possibly sourced from metabasites on opposite side of shear zone. This observation further supports that the SISZ experienced cross fluid flow.

5.4 Interpretation of Vorticity Data

Based on work within the BAM, we anticipate that the SISZ experienced left-lateral transpression with flattening fabrics and oblique extrusion (Fernández et al., 2013). Given that model, we would expect kinematic vorticity numbers to fall in between 0 (pure shear) and 1 (simple shear). In this study, seven out of nine kinematic vorticity number calculations were indicative of simple shear dominated flow, while the other two were close to simple shear dominated but in the pure shear dominated category. These values indicate that the motion of the SISZ within the PdL is almost entirely simple shear with very little pure shear (2D) or flattening (3D). Interestingly, the asymmetric indicators within the PdL suggest that the simple shear is consistent with thrust motion in comparison to largely strike-slip motion within the BAM (Díaz

Azpiroz and Fernández, 2007; Fernández et al., 2013). It is not clear why this should be the case.

The kinematic vorticity numbers do not vary with respect to distance from the shear zone, suggesting that kinematic partitioning is not observed with increasing strain. This result for the PdL is different than what has been found in several other studies where strain is partitioned into simple shear dominated high strain areas and pure shear dominated low strain areas (e.g., Jones and Tanner, 1995; Zhang et al., 2009). Alternatively, it is possible that within this study, all the samples were close enough to the SISZ to be within a simple shear dominated area.

CHAPTER 6: Future Work

Since fluids are catalysts to metamorphic reactions and strain localization of the rocks, a full-scale geochemistry project is needed to better understand the fluid history of the heterogeneous sheared domain in the Pulo do Lobo formation. For example, some of the studied PdL samples were in the heterogeneously sheared domain, where there were large differences in chemistry from one sample to another. These differences may be due to further localized features, the shear bands that cut the main foliation at high angle, allowing another channel of fluid flow and thereby geochemically altering the rocks. We also observed different metamorphic gradients in our reconnaissance of other transects (i.e.: some transects do not have schists at the SISZ boundary). This observation suggests that fluid flow may have varied along strike. In addition to further major/minor element geochemical analyses, trace element geochemistry may also allow us to learn more about the fluids. In addition, stable isotope analysis may allow us to distinguish the origin (meteoric versus metamorphic) of the hydrous fluids (Webb et al., 1998; Wawrzyniec et al.,1999; Yonkee et al., 2013). Taken together, these further geochemical studies may help us better understand fluid origin and composition (Stephenson, 2018).

To further constrain the relative contribution of deformation mechanisms with strain, future research could employ Electron Backscatter Diffraction (EBSD) on quartz grains. EBSD is used to quantify strength of crystallographic preferred orientation (CPO), which only forms in crystal plasticity. This technique would provide a more quantitative way to determine the relative contributions of crystal plasticity, DMT, and brittle deformation across the strain gradient.

The shape of CPO patterns derived from EBSD can also be used as another way to estimate kinematic vorticity within plastically deformed sheared rocks. We can compare the

results of this technique with the one used in this study to further test whether kinematic vorticity number varies with strain magnitude (Toy et al., 2008).

In addition, EBSD crystallographic vorticity axis (CVA) can be used as an independent method to determine the orientation of the vorticity vector (Michels, 2015). In this study, the asymmetric features indicated thrust motion which requires a horizontal vorticity vector. Within the BAM, previous analysis indicates mostly a left-lateral motion with a vertical-subvertical vorticity vector (Fernández et al., 2013). Therefore, these differences imply that the simple shear component of deformation is partitioned into strike-slip and dip-slip components restricted to each side of the SISZ. This type of strain partitioning is unusual and should be given further scrutiny.

CHAPTER 7: Conclusions

Previous work has focused on the Acebuches metabasites where a highly localized strain gradient, synkinematic fluid flow, and triclinic transpression kinematics have been well-documented. This study focused on the shear zone's effects on the lesser-studied Pulo do Lobo formation, a mixture of metapelites and quartzites. The purpose of this project was to evaluate factors that contribute to strain localization at a variety of scales including lithologic variations encompassing composition and grain size, metamorphism, tectonic fabrics, and fluid flow.

Detailed lithological mapping along a 250 m transect perpendicular to the shear zone was conducted to document lithologic units and associated rheology contrasts. The predominantly quartz rich PdL formation is comprised of metapelites including slates, phyllites, and mica schists and quartzites. Qualitative measures of fabric were used as a proxy for strain magnitude. Closest to the shear zone contact (0-65 m), highest strain is identified by closely spaced strong schistose foliation. At 65-171 m from the shear zone, strain is manifested by anastomosing phyllitic foliations surrounding lozenges of relatively unstrained quartzite zones and cm-dm scaled folds. Approximately 172 m from the shear zone, foliation intensity diminishes and metamorphic grade decrease resulting in slates that match the fabric and metamorphic grade found regionally. This relatively large metamorphic facies change in a small area was likely facilitated by hydrothermal aqueous fluid that moved along the BAM during peak metamorphism and deformation.

Microstructural observations were used to determine the dominant deformation mechanisms and whether they varied across the zone. Crystal-plasticity gradually increased towards the shear zone which most likely allowed a gradual strain increase. Near the SISZ, fluids enabled deformation via DMT which is promoted by fluid. Very close to the shear zone (< 10 m), localized embrittlement occurred, likely induced by transient high fluid pressures.

Syndeformational fluid promoted strain softening via many mechanisms including strain softening metamorphic reactions, hydrolytic weakening which enhances crystal-plasticity and promotion of DMT. Transient brittle behavior, likely caused by intermittent increases in fluid pressure allowed more fluid into the PdL which allowed further strain softening. Thus, there was likely ongoing ductile deformation accommodated by crystal plasticity and DMT with occasional brittle fracturing events.

Major element geochemical measurements along the transect allowed determination of elemental changes which indicate effects of fluid along the shear zone. Samples selected for geochemical analysis include those of intermediate silica compositions. Isocon plots comparing samples far outside the shear zone to those clearly affected by the shear zone indicate that typical immobile elements like Al_2O_3 and TiO_2 and major mobile elements like Si remain relatively constant, suggesting little to no volume change. K_2O and possibly CaO are enriched towards the shear zone while Na_2O is depleted. The CaO and Na_2O concentrations are likely related to the stability of more Ca rich feldspars at higher metamorphic grade, suggesting that the fluid migration along the shear zone enhanced feldspar reactions. The enrichment in K_2O, also observed in the metabasites by previous researchers, is additional evidence of fluid flow along the shear zone. The enrichment of MgO and possibly Fe_2O_3 suggest that fluid sourced from the BAM crossed the SISZ, perhaps during localized fracturing events.

Factors that control strain localization along the Southern Iberian Shear Zone are scalar. At the terrane scale, the shear zone is localized along the metabasite/ metapelite contact. At the outcrop scale, lithological contrasts control strain magnitude. But at an intermediate scale, fluids play a major role by catalyzing strain-softening metamorphic reactions and enhancing deformation via diffusive mass transfer and transient embrittlement. This study provides an example of how

strain localization is accomplished within the mid-lower crust during tectonic events, with a particular focus on fluid-enhanced strain.

Fluids moving through shear zones often follow a conduit-barrier model, where fluids generally flow into and move along the shear zone but do not cross sides (e.g., Yonkee et al., 2003). Generally, the increased concentration of geochemical and microstructural evidence for aqueous hydrothermal fluids closer to the SISZ suggest that the structure acted as a major conduit for fluid flow. Previous researchers found evidence that fluids from the PdL may have crossed into the BAM (Stephenson, 2018; Czeck et al., 2019) and the MgO enrichment in this study suggests that fluids from the BAM may have also crossed into the PdL. These observations support a model of a conduit-barrier that occasionally allowed leakage of fluid across the structure. The fluid source for the K_2O enrichment is potentially metamorphic fluid from the broader PdL which dewatered when turning into slates and even occasionally from the BAM. The fluid source for the MgO and Fe_2O_3 enrichment is possibly the BAM where these elements were mobilized during retrograde metamorphic reactions involving amphiboles and chlorite (Stephenson, 2018).

Fluid flow, metamorphism, and fluid enhanced deformation formed a positive feedback whereby deformation resulted in increased softening which resulted in further deformation; all of which resulted in extreme localization of strain along the SISZ.

CHAPTER 8: References

Ábalos, B., Carreras, J., Druguet, E., Escuder Viruete, S., Gómez Pugnaire, M.T., Lorenzo Álvarez, S., Quesada, C., Rodríguez Fernández, L.R., Gil Ibarguchi, J.I., 2002. Variscan and Pre-Variscan tectonics. In: Gibbons, W., Moreno, T. (Eds.), The Geology of Spain. Geological Society, London, pp. 156–183

Arbaret, L., Chaudhry, G., Dawood, H., Hussain, S., Zeilinger, G., 2000. Pre-collisional anastomosing shear zones in the Kohistan Complex (NW Pakistan). Geological Society, London, Special Publications. 295-311.

Axen, G. J., 2001. High-temperature embrittlement of extensional Alpine mylonite zones in the midcrustal ductile-brittle transition. Journal of Geophysical Research 106, 4337-4348.

Azor, A., Rubatto, D., Simancas, J.F., González Lodeiro, F., Martínez Poyatos, D., Martin Parra, L.M., and Matas, J., 2008. Rheic Ocean ophiolitic remnants in southern Iberia questioned by SHRIMP U-Pb zircon ages on the Beja-Acebuches amphibolites. Tectonics 27 TC5006, doi:10.1029/2008TC002306.

Bard, J.P., Moine, B., 1979. Acebuches amphibolites in the Aracena Hercynian metamorphic belt (southwest Spain): Geochemical variations and basaltic affinities, Lithos 12, 271-282.

Barnes, J. D., Selverstone, J., Sharp, Z. D, 2004. Interactions between serpentine devolitization, metasomatism and strike-slip strain localization during deep-crustal shearing in the Eastern Alps. Journal of Metamorphic Geology 22(4), 283-300.

Barszewski, C.E., 2012. Microstructural and cathodoluminescence (SEM-CL) analyses of clasts in a tectonically deformed diamictite from the Willard Thrust, UT. MS Thesis. University of Wisconsin-Milwaukee, 107 pages.

Beach, A., 1980. Retrogressive metamorphic processes in shear zones with special reference to the Lewisian complex. Journal of Structural Geology 2, 257-263.

Behrmann, J.H., 1987. A precautionary note on shear bands as kinematic indicators. Journal of Structural Geology 9, 659-666.

Berthé, D., Choukroune, P., Gapais, D., 1979. Orthogneiss mylonite and non-coaxial deformation of granites: the example of the South Armorican shear zone. Journal of Structural Geology 1, 31-42.

Blenkinsop, T., 2000. Deformation Microstructures and Mechanisms in Minerals and Rocks. Springer, 150 pp. doi:10.1007/0-306-47543-X.

Bobyarchick, A., 1986. The eigenvalues of steady state flow in Mohr space. Tectonophysics 122, 35–51.

Braid, J.A., 2010. The Dynamics of Allochthonous Terranes in the Pangean Suture Zone of Southern Iberia. PhD Dissertation. Dalhousie University, 293 pages.

Braid, J. A., Murphy, J. B, Quesada, C., 2010. Structural Analysis of an Accretionary Prism in a Continental Collisional Setting, the Late Paleozoic Pulo Do Lobo Zone, Southern Iberia. Gondwana Research 17, 422-439.

Braid, J.A., Murphy, J.B., Quesada, C., Bickerton, L., and Mortensen, J.K., 2012. Probing the composition of unexposed basement, South Portuguese Zone, southern Iberia: Implications for the connections between the Appalachian and Variscan orogens. Canadian Journal of Earth Sciences 49, 591–613.

Braudy, N., Dair, L., Giorgis, S., Michels, Z., Tikoff, B., 2016. Kinematic and vorticity analyses of the western Idaho shear zone, USA. Lithosphere 8, 1-12.

Bukovská, Z., Jeřábek, P., Morales, L.F.G., 2016. Major softening at brittle-ductile transition due to interplay between chemical and deformation processes: An insight from evolution of shear bands in the South Armorican Shear Zone. Journal of Geophysical Research 121, 1158-1182.

Byers, H., McHenry, L.J., Grundl, T.J. 2016. Forty-nine major and trace element concentrations measured in Soil Reference Materials NIST SRM 2586, 2587, 2709a, 2710a and 2711a using ICP-MS and Wavelength Dispersive-XRF. Geostandards and Geoanalytical Research 40: 433- 445.

Cambeses, A., Scarrow, J.H., Montero, P., Molina, J.F., and Moreno, J.A., 2015. SHRIMP U-Pb zircon dating of the Valencia del Ventoso plutonic complex, Ossa-Morena Zone, SW Iberia: Early Carboniferous intra-orogenic extension-related “calc-alkaline” magmatism. Gondwana Research 28, 735–756.

Carter, N.L., Kronenberg, A.K., Ross, J.V., Witltschko, D.V., 1990. Control of fluids on deformations of rocks. In: Knipe, R.J, Rutter, E.H. Eds., Deformation Mechanism, Rheology and Tectonics. Geol. Soc. Spec. Publ. 54, 1-13.

Castro, A., Fernández, C., de la Rosa, J. D., Moreno-Ventas, I., Rogers, G., 1996. Significance of MORB-derived amphiboles from the Aracena Metamorphic Belt, southwest Spain, J. Petrol. 37, 235–260.

Crespo-Blanc, A., Orozco, M., 1988. The southern Iberian shear zone: A major boundary in the Hercynian folded belt, Tectonophysics 148, 221-227.

Cox, S. F., 2002. Fluid flow in mid- to deep crustal shear systems: Experimental constraints, observations on exhumed high fluid flux shear systems, and implications for seismogenic processes. Earth Planets Space 54, 1121-1125.

Czeck, D.M., Hudleston, P.J., 2003. Testing models for obliquely plunging lineations in transpression: a natural example and theoretical discussion. Journal of Structural Geology 25, 959-982.

Czeck, D.M., Stephenson, S.I., Díaz-Azpiroz, M., Fernández, C., García-Arias, M., 2019. Syndeformational fluid flow in metabasite rocks along the Southern Iberian Shear Zone. Geological Society of America Abstracts with Programs 51, No. 5. Phoenix, AZ. doi: 10.1130/abs/2019AM-339027.

Dahn, D.R.L., Braid, J.A., Murphy, J.B., Quesada, C., Dupuis, N., Mcfarlane, C.R.M., 2014. Geochemistry of the Peramora Mélange and Pulo do Lobo schist: Geochemical investigation and tectonic interpretation of mafic mélange in the Pangean suture zone, Southern Iberia. International Journal of Earth Sciences 103, 1415-1431.

Davis, D., Suppe J., Dahlen, F.A. 1983. Mechanics of fold-and-thrust belts and accretionary wedges. Journal of Geophysical Research 88, 1153–1172.

Díaz Azpiroz, M., Fernández, C., 2005. Kinematic analysis of the southern Iberian shear zone and tectonic evolution of the Acebuches metabasites (SW Variscan Iberian Massif). Tectonics 24, 1–19. doi: 10.1029/2004TC001682.

Díaz Azpiroz, M., Fernández, C., Castro, A., El-Biad, M., 2006. Tectonometamorphic evolution of the Aracena metamorphic belt (SW Spain) resulting from ridge-trench interaction during Variscan plate convergence. Tectonics 25. TC1001, doi:10.1029/2004TC001742.

Díaz Azpiroz, M., Fernández, C., Lloyd, G.E., 2007. Development of lattice preferred orientation in clinoamphiboles deformed under low-pressure metamorphic conditions. A SEM/EBSD study of metabasites from the Aracena metamorphic belt (SW Spain). Journal of Structural Geology 629-645.

Deer, W.A., Howie, R.A., and Zussman, J., 2013. An introduction to rock forming minerals. The Mineralogical Society, 498 pp. doi.org/10.1180/DHZ

Druguet, E., Czeck, D. M., Carreras, J., and Castaño, L. M., 2008. Emplacement and deformation features of syntectonic leucocratic veins from Rainy Lake zone (Western Superior Province, Canada). Precambrian Research 163, 384–400.

Fernández, C., Czeck, D. M., Díaz-Azpiroz, M., 2013. Testing the model of oblique transpression with oblique extrusion in two natural cases: steps and consequences. Journal of Structural Geology 54, 85-102.

Finch, M. A., Bons, P.D., Steinbach, F., Griera, A., Llorens, M.-G., Gomez-Rivas, E., Ran, H., de Riese, T., 2020. The ephemeral development of C′ shear bands: A numerical modelling approach. Journal of Structural Geology 139, 104091.

Fletcher, R.C., 1989. Approximate analytical solutions for a cohesive fold-and-thrust wedge: some results for lateral variation in wedge properties and for finite wedge angle. Journal of Geophysical Research 94, 10347-10354.

Fossen, H., Tikoff, B., 1993. The deformation matrix for simultaneous simple shearing, pure shearing and volume change, and its application to transpression-transtension tectonics. Journal of Structural Geology 15, 413-422.

Fossen, H., 2016. Structural Geology (2nd edition). Cambridge University Press, 524 pp.

Fossen, H., Cavalcante, G. C. G., 2017. Shear zones – A review. Earth-Science Reviews 171**,** 434–455

García-Navarro, E., Fernández, C., 2004. Final stages of the Variscan orogeny at the southern Iberian massif: Lateral extrusion and rotation of continental blocks. Tectonics TC6001, doi:10.1029/2004TC001646.

Giese, U., Hoymann, K.-H., Glodny, J., Kramm, U., Dallmeyer, R.D., 1999. Age constraints for the tectonometamorphic evolution of the Pulo do Lobo Zone in SW Spain. Zeitschrift Der Deutschen Geologischen Gesellschaft 150, 565 - 582.

Grant, J.A., 1986. The isocon diagram; a simple solution to Gresens' equation for metasomatic alteration. Economic Geology 81, 1976-1982.

Giorgis, S., Michels, M., Dair, L., Braudy, N., Tikoff, B., 2017. Kinematic and vorticity analyses of the western Idaho shear zone, USA. Lithosphere 9, 223–234.

Griggs, D., 1967. Hydrolytic weakening of quartz and other silicates. Royal Astronomical Society Geophysical Journal 14, 19–31.

Horsman, E., Tikoff, B., and Czeck, D. M., 2008. Rheological implications of heterogeneous deformation at multiple scales in the Late Cretaceous Sierra Nevada, California. Geological Society of America Bulletin 120, 238-255.

Huntington, K.W., Klepeis, K.A., with 66 community contributors, 2018. Challenges and opportunities for research in tectonics: Understanding deformation and the processes that link Earth systems, from geologic time to human time. A community vision document submitted to the U.S. National Science Foundation. University of Washington, 84 pp., https://doi.org/10.6069/H52R3PQ5.

Jessup, M. J., Law, R.D., Frassi, C., 2007. The Rigid Grain Net (RGN): An alternative method for estimating mean kinematic vorticity number (Wm). Journal of Structural Geology 29, 411-421.

Jessup, M.J., Cottle, J.M., 2010. Progression from south-directed extrusion to orogen-parallel extension in the Southern Margin of the Tibetan Plateau, Mount Everest region, Tibet. Journal of Geology 118, 467–486.

Jiang, D., Williams, P.F., 1998. High-strain zones: a unified model. Journal of Structural Geology 20, 1105-1120.

Jiang, D., Lin, S., Williams, P.F., 2001. Deformation paths in high-strain zones, with reference to slip partitioning in transpressional plate-boundary regions. Journal of Structural Geology 23, 991-1005.

Jones, R.R., Holdsworth, R.E., McCaffrey, K.J.W., Clegg, P., Tavarnelli, E. 2005. Scale dependence, strain compatibility and heterogeneity of three-dimensional deformation during mountain building: a discussion. Journal of Structural Geology 27, 1190-1204.

Jones, R. R., Tanner, P. W. G., 1995. Strain partitioning in transpression zones. Journal of Structural Geology 17, 793-802.

Kurz, G.A., Northrup, C.J., 2008. Structural analysis of mylonitic fault rocks in the Cougar Creek Complex, Oregon-Idaho using the porphyroclast hyperbolic distribution method, and potential use of SC'-type extensional shear bands as quantitative vorticity indicators. Journal of Structural Geology 30, 1005-1012.

Lin, S., Jiang, D., Williams, P.F., 1998. Transpression (or transtension) zones of triclinic symmetry: natural example and theoretical modeling. In: Holdsworth, R.E., Strachran, R.A., Dewey, J.F. (Eds.), Continental Transpressional and Transtensional Tectonics, Geological Society of London, Special Publications, vol. 135. Geological Society of London, London, pp. 41-57.

Lister, G.S., Snoke, A.W., 1984. S-C mylonites. Journal of Structural Geology 6, 617-638.

Marquer, D., Challandes, N., Baudin, T., 1996. Shear zone patterns and strain distribution at the scale of a Penninic nappe: the Suretta nappe (Eastern Swiss Alps). Journal of Structural Geology 18, 753–764.

Marquer, D., Peters, T., Gnos, E., 1995. A new structural interpretation for the emplacement of the Masirah ophiolites (Oman): A main Paleocene intra-oceanic thrust. Geodinamica Acta, 8(1), 13-19.

Matte, P., 2001, The Variscan collage and orogeny (480 – 290 Ma) and the tectonic definition of the Armorica microplate: A review. Terra Nova 13, 122-128. doi:10.1046/j.1365-3121.2001.00327.x

McHenry, L.J, 2009. Element mobility during zeolitic argillic alteration of volcanic ash in a closed-basin lacustrine environment: Case study Olduvai Gorge, Tanzania. Chemical Geology, 540-552.

Means, W.D., Hobbs, B.E., Lister, G.S., Williams, P.F., 1980. Vorticity and noncoaxiality in progressive deformations. Journal of Structural Geology 2, 371–378.

Michels, Z.D., Kruckenberg, S., Davis, J.R., Tikoff, B., 2015. Determining vorticity axes from grain-scale dispersion of crystallographic orientations. Journal of Structural Geology 43, 803-806.

Mukherjee, K., Gupta, P.K., 2008. Arbitrary scaling in ISOCON method for geochemical mass balance: An evaluation of the graphical approach. Geochemical Journal 42, 247-253.

Nance, R.D., Gutiérrez-Alonso, G., Keppie, D., Linnemann, U., Murphy, J.B., Quesada, C., Strachan, R.A., Woodcock, N.H., 2010. Evolution of the Rheic Ocean. Gondwana Research 17, 194-222.

Nance, R.D., Linnemann, U., 2008. The Rheic Ocean: origin, evolution and significance. GSA Today 18, 4-12.

Newman, J., Mitra, G., 1993. Lateral variations in mylonite zone thickness as influenced by fluid-rock interactions, Linville Falls fault, North Carolina. Journal of Structural Geology 15, 849-863.

O'Hara, K., 1990. State of strain in mylonites from the western Blue Ridge province, southern Appalachians: the role of volume loss. Journal of Structural Geology 12, 419-430.

Passchier, C.W., 1998. Monoclinic model shear zones. Journal of Structural Geology 20, 1121-1137.

Passchier, C.W., 2001. Flanking structures. Journal of Structural Geology 23, 951-962.

Pereira, Z., Fernandes, P., Matos, J. X., Jorge, R. C. G. S., Oliveira, J. T., 2018. Stratigraphy of the Northern Pulo do Lobo Domain, SW Iberia Variscides: A palynological contribution. Geobios 51, 491–506.

Ponce, C., Carreras, J., Druguet, E., 2010. Development of "lozenges" in anastomosing shear zone networks in foliated rocks. Geogaceta 48, 207-210.

Quesada, C., Braid, J. A., Fernandes, P., Ferreira, P., Jorge, R. S., Matos, J. X., Murphy, J. B., Oliveira, J. T., Pedro, J., Pereira, Z., 2019. Chapter 5: SW Iberia Variscan Suture Zone: Oceanic Affinity Units. From: The Geology of Iberia: A Geodynamic Approach, Regional Geology Reviews, C. Quesada and J. T. Oliveira (eds.). Springer, 131-171. https://doi.org/10.1007/978-3-030-10519-8_5

Quesada, C., Fonseca, P., Munhá, J., Oliveira, J.T., Ribeiro, A., 1994. The Beja-Acebuches Ophiolite (Southern Iberia Variscan Fold Belt): geological characterization and geodynamic significance. Boletín Geológico Minero 105, 3–49.

Sánchez-García, T., Bellido, F., Quesada, C., 2003. Geodynamic setting and geochemical signatures of Cambrian–Ordovician rift-related igneous rocks (Ossa-Morena Zone, SW Iberia). Tectonophysics 365, 233–255.

Sánchez-García, T., Quesada, C., Bellido, F., Dunning, G.R., González de Tánago, J., 2008. Two-step magma flooding of the upper crust during rifting: the Early Paleozoic of the Ossa Morena Zone (SW Iberia). Tectonophysics 461, 72–90.

Scotese, C.R., Barret, S.F., 1990. Gondwana's movement over the South Pole during the Palaeozoic: evidence from lithological indicators of climate. In: McKerrow, W.S., Scotese, C.R. (Eds.), Palaeozoic Palaeogeography and Biogeography: Geological Society of London Memoir, vol. 12, pp. 75–85.

Shea, W.T., Kronenberg, A.K., 1993. Strength and anisotropy of foliated rocks with varied mica contents. Journal of Structural Geology 15, 1097-1121.

Stephenson, S. I., 2018. Characterizing the geochemical changes across a strain gradient in the Beja-Acebuches metabasites due to retrograde metamorphism and fluid flow along the Southern Iberian Shear Zone. MS Thesis. University of Wisconsin-Milwaukee, 112 pages.

Tomkins, A.G., Weinberg, R.F., McFarlane, C.R.M., 2009, Preferential magma extraction from K- and metal-enriched source regions in the crust. Mineralium Deposita, 44, 171.

Toy, V. G., Prior, D. J., Norris, R. J., 2008. Quartz fabrics in the Alpine Fault mylonites: Influence of pre-existing preferred orientations on fabric development during progressive uplift. Journal of Structural Geology 20, 602-621.

Vernon, R.H., A practical guide to rock microstructure, Cambridge University Press, Cambridge, UK, 593 pp.

Wawrzyniec, T., Selverstone, J., Axen, G. J., 1999. Correlations between fluid composition and deep-seated structural style in the footwall of the Simplon low-angle normal fault, Switzerland. Geology 27(8), 715-718.

Webb, J.A., Golding, S.D., 1998. Geochemical mass-balance and oxygen-isotope constraints on Silcrete Formation and its paleoclimatic Implications in Southern Australia. Journal of Sedimentary Research 5, 981-993.

Wintsch, R.P., Yi, K., 2002. Dissolution and replacement creep: a significant deformation mechanism in mid-crustal rocks. Journal of Structural Geology 24, 1179–1193.

Xypolias, P., 2010. Vorticity analysis in shear zones: a review of methods and applications. Journal of Structural Geology 32, 2072–2092.

Yonkee, W.A., Czeck, D.M., Nachbor, A., Barszewski C.B., Pantone, S., Balgord, E., Johnson, K. R., 2013. Strain accumulation and fluid-rock interaction in a naturally deformed diamictite, Willard thrust system, Utah (USA): Implications for crustal rheology and strain softening. Journal of Structural Geology 50, 91-118.

Zhang, B., Zhang, J.J., Zhong, D.L., and Guo, L., 2009. Strain and kinematic vorticity analysis: An indicator for sinistral transpressional strain-partitioning along the Lancangjiang shear zone, western Yunnan, China. Science in China, Series D: Earth Sciences 52, 602–618.

CHAPTER 9: Appendices

9.1 Pulo do Lobo data

9.1.1 Samples

Almonaster Transect							
Sample ID	GPS coordinates	Distance from Shear Zone (m)	Rock Type	Mineralogy	Foliation	Lineation	Orientation of Thin Section (strike/dip of Plane; trend/plunge long axis)
SI-83	N 37.86428, W 006.78566	7.2	Schist	Quartz, muscovite, biotite, chlorite, plagioclase, garnet	133, 81NE	assume down-dip	223/90; 043/83
SI-84	N 37.87009, W 006.78473	11.2	Schist	Quartz, muscovite, biotite, chlorite, plagioclase, garnet	126, 75NE	assume down-dip	216/90; 036/75
SI-85	N 37.87010, W 006.78471	12.8	Schist	Quartz, muscovite, biotite, chlorite, plagioclase, garnet	139, 66NE	assume down-dip	229/90; 049/66
SI-86	N 37.87008, W 006.78474	14.6	Schist	Quartz, muscovite, biotite, chlorite, plagioclase, garnet	137, 69NE	assume down-dip	227/90; 047/69
SI-87	N 37.87005, W 006.78473	16.1	Schist	Quartz, muscovite, biotite, chlorite, plagioclase, garnet	132, 69NE	assume down-dip	222/90; 042/69
PL1		17.3	Schist		125, 67NE		
SI-88	N 37.87004, W 006.78476	20.2	Schist	Quartz, muscovite, biotite, chlorite, plagioclase, garnet	133, 66NE	assume down-dip	223/90; 043/66
PL2		21.2	Schist		135, 52NE		
PL3		22.7	Schist		134, 63NE		
SI-89	N 37.87002, W 006.78480	24.1	Phyllite	Quartz, muscovite, biotite	125, 70NE	assume down-dip	215/90; 035/70
SI-90	N 37.87001, W 006.78484	23.8	Phyllite	Quartz, muscovite, biotite	123, 69NE	assume down-dip	213/90; 033/69
SI-91	N 37.87002, W 006.78486	25.8	Phyllite	Quartz, muscovite, biotite	125, 50NE	assume down-dip	215/90; 035/50
PL4		26.6	Phyllite		118, 63NE		
PL5		40.6	Phyllite		135, 65NE		
SI-92A (Q)	N 37.86993, W 006.78487	43.6	Phyllite	Quartz, muscovite, biotite	147, 70NE	assume down-dip	237/90; 057/70
SI-92B (P)	N 37.86993, W 006.78487	43.1	Phyllite	Quartz, muscovite, biotite	145, 69NE	assume down-dip	235/90; 055/69
SI-93	N 37.86987, W 006.78491	46.7	Phyllite	Quartz, muscovite, biotite	120,73NE	assume down-dip	210/90; 030/73

PL6		51.5	Phyllite		127, 66NE		
PL7		53.4	Phyllite		127, 67NE		
PL8		55.2	Phyllite		121, 70NE		
PL9		55.7	Phyllite		125, 80NE		
SI-94P	N 37.86980, W 006.78503	56	Phyllite	Quartz, muscovite, biotite	133, 75NE	assume down-dip	223/90; 043/75
SI-94Q	N 37.86983, W 006.78504	56.1	Quartzite	Quartz	123, 78NE	assume down-dip	213/90; 033/78
PL10		57.7	Phyllite		125, 65NE		
PL11		62.2	Phyllite		113, 38NE		
PL12		65.5	Phyllite		107, 58NE		
PL13		68.1	Phyllite		120, 60NE		
SI-95P	N 37.86967, W 006.78514	71.3	Slate, Phyllite	Quartz, muscovite, biotite	142, 40NE	107/16	232/90; 052/40
SI-96P	N 37. 86962, W 006.78518	?	Slate, Phyllite	Quartz, muscovite, biotite	137, 56NE	assume down-dip	227/90; 047/56
SI-96Q	N 37.86963, W 006.78518	?	Quartzite	Quartz	142, 68NE	assume down-dip	232/90; 052/68
PL14		76.4	Phyllite		130, 62NE		
PL15		82.9	Phyllite		135, 59NE		
PL16		92.4	Phyllite		130, 58NE		
PL17		98	Phyllite		135, 40NE		

SI-97P	N 37.86934, W 006.78532	107.3	Phyllite	Quartz, muscovite, biotite	133, 58NE	assume down-dip	223/90; 043/58
SI-98P	N 37.86918, W 006.78524	120.7	Phyllite	Quartz, muscovite, biotite	132, 60NE	assume down-dip	222/90; 042/60
PI18		122.8	Phyllite		145, 57NE		
SI-99P	N 37.86912, W 006.78531	134.5	Slate	Quartz, muscovite, biotite	133, 80NE	assume down-dip	223/90; 043/89
SI-100P	N 37.86899, W 006.78544	155.4	Phyllite	Quartz, muscovite, biotite	121, 61NE	assume down-dip	211/90; 031/61
PL19		171.1	Phyllite		135, 54NE		
SI-101P	N 37.86889, W 006.78547	173	Phyllite	Quartz, muscovite, biotite	131, 65NE	assume down-dip	221/90; 041/65
SI-102P	N 37.6877, W 006.78551	182.1	Slate	Quartz, muscovite, biotite	125, 82NE	assume down-dip	215/90; 035/82
SI-103P	N 37.86872, W 006.7556	185.8	Slate	Quartz, muscovite, biotite	120, 68NE	assume down-dip	210/90; 030/68
PL20		192.6	Slate		146, 54NE		
SI-104P	N 37.86855, W 006.78574	202.8	Slate	Quartz, muscovite, biotite	118, 50NE	assume down-dip	208/90; 028/50
SI-105P	N 37.86852, W 006.78586	212	Slate	Quartz, muscovite, biotite	133, 67NE	assume down-dip	223/90; 043/67
SI-106P	N 37.86818, W 006.78605	243.5	Slate	Quartz, muscovite, biotite	142, 40NE	assume down-dip	232/90; 052/40
SI-82	N 37.86428, W 006.78566	>400	Slate	Quartz, muscovite, biotite	107, 65N	assume down-dip	197/90; 017/65
SI-107	N 37.86307, W 006.78506	>400	Slate	Quartz, muscovite, biotite	070, 61NW		
SI-108A	N 37.86176, W 006.78613	>400	Dirty quartzite	Quartz, micas	095, 85S	100/43	
SI-108B	N 37.86176, W 006.78613	>400	Dirty quartzite	Quartz, micas	097, 82S	099/33	

Almonaster y La Escalada Transect						
SI-109A	N 37.86035, W 006.79471		Slate	Quartz, muscovite, biotite, albite	266, 55SE	
SI-109B	N 37.86026, W 006.79478		Slate	Quartz, muscovite, biotite, albite	243, 60SE	
SI-109C	N 37.86021, W 006.79476		Slate	Quartz, muscovite, biotite, albite	266, 60SE	
SI-109D	N37. 86026, W 006.79476		Slate	Quartz, muscovite, biotite, albite	297, 44SE	
SI-110A	N37.86035, W 006.79471		Slate	Quartz, muscovite, biotite, albite	280,67NE	
SI-110B	N 37.86922, W 006.79021		Slate	Quartz, muscovite, biotite, albite	276, 52NE	
SI-110C	N 37.86919, W 006.79024		Slate	Quartz, muscovite, biotite, albite	295, 55NE	
Alajar Transect						
SI-111	N 37.86094, W 006.65612		Phyllite	Quartz, muscovite, biotite, albite	103, 45N	064/16
SI-112	N 37.86027, W 006.65624		Phyllite	Quartz, muscovite, biotite, albite	114, 72NE	
SI-113	N 37.85969, W 006.65644		Phyllite	Quartz, muscovite, biotite, albite	087, 85N	
SI-114	N 37.85895, W 006.65605		Phyllite	Quartz, muscovite, biotite, albite	092, 50NE	150/44
SI-115	N 37.85887, W 006.65567		Phyllite	Quartz, muscovite, biotite, albite	078, 76N	
SI-116	N 37.85814, W 006.65473		Phyllite	Quartz, muscovite, biotite, albite	092, 72N	
SI-117	N 37.85062, W 006.64727		Phyllite	Quartz, muscovite, biotite, albite	075, 51N	
SI-118	N 37.84833, W 006.64364		Phyllite	Quartz, muscovite, biotite, albite	064, 76 S	

9.2 Thin section data

9.2.1 Microstructural Qualitative Observations

Table 6: Brittle, Twinning, and Diffusive Mass Transfer (DMT) Microstructures; X = present; XX = common, XXX = abundant

	Brittle						Twinning			DMT			
Sample ID	Intergranular Fractures	Intragranular Fractures in Quartz	Intragranular Fractures in Plagioclase	Veins	Vein fill material	Fluid inclusion trails	Albite (growth) twinning in plagioclase	Deformation twinning in plagioclase	Cross-hatch twinning in K-spar	Selvage seams	Sutured grain boundaries	Strain shadows	strain shadow fill
SI-83	XXX	XXX	XX	XX	quartz, micas	XX	XX	XX	XX	XXX	XXX	XXX	quartz, chlorite
SI-84	XXX	XXX	XX	XX	quartz, micas	XX	XX	XX	XX	XXX	XXX	XXX	quartz, chlorite
SI-85	XXX	XXX	XX	XX	quartz, micas	XXX	XX	XX		XXX	XXX	XXX	quartz, chlorite
SI-86	XXX	XXX	XX	XX	quartz, micas	XXX	XX	XX		XXX	XXX	XXX	quartz, chlorite
SI-87	XXX	XXX	XX	XX	quartz, micas	XXX	XX	XX		XXX	XXX	XXX	quartz, chlorite
SI-88	XXX	XXX		XX	quartz, micas	XXX				XXX	XXX	XXX	quartz, chlorite
SI-89	XXX	XXX				XX				XXX	XXX	XXX	quartz, mica
SI-90	XXX	XXX				XX				XXX	XXX	XXX	quartz, mica
SI-91	XXX	XXX				XX				XXX	XXX	XXX	quartz, mica
SI-92A (Q)	XXX	XXX				XX				XXX	XXX	XXX	quartz, mica
SI-92B (P)	XXX	XXX				XXX				XXX	XXX	XXX	quartz, mica
SI-93	XXX	XXX				XXX				XXX	XXX	XXX	quartz, mica
SI-94P	XXX	XXX				XXX				XXX	XXX	XXX	quartz, mica
SI-94Q	XXX	XXX		XX	micas and brown alteration	XXX				XXX	XXX	XXX	quartz
SI-95P	XX	XX		XX	reddish alteration	XXX				XX	XX	XX	quartz, mica

SI-96P													
SI-96Q	XX	XX		X	brown-orange alteration	XX				XX	XX	XX	quartz
SI-97P	XX	XX		X	quartz, micas	XX				XX	XX	XX	quartz, mica
SI-98P		XX		X	quartz, micas	X				XX	XX	XX	quartz, mica
SI-99P		XX		X	quartz, micas								
SI-100P	XX	XX				XX				XX	XX	XX	quartz, mica
SI-101P	XX	XX				XX				XX	XX	XX	quartz, mica
SI-102P		X		X	quartz	X						X	quartz
SI-103P													
SI-104P	X	X		X	quartz	X					X	X	quartz, mica
SI-105P	X	X		X	quartz	X					X	X	quartz, mica
SI-106P	X	X		X	quartz								
SI-82				X	orange alteration								

Table 7: Crystal-Plastic Microstructures: X = present; XX = common, XXX = abundant

crystal-plasticity													
Sample ID	Undulose Extinction quartz	Grain boundary migration (puzzle-pieces)	Bulged grain boundaries quartz	Subgrain formation quartz	Recrystallization quartz (sugary texture)	deformation lamellae in quartz	undulose extinction in plagioclase	Bulged grain boundaries in plagioclase	Subgrain formation in plagioclase	Recrystallization in plagioclase	deformation lamallae in plagioclase	kinked mica grains	triple junctions
SI-83	XXX	XXX	XXX	XXX	XXX	XX	XXX	XX	XX	XX	XX	XX	XX
SI-84	XXX	XXX	XXX	XXX	XXX	XX	XXX	XX	XX	XX	XX	XX	XX
SI-85	XXX	XXX	XXX	XXX	XXX	XX	XXX	XX	XX	XX	XX	XX	XX
SI-86	XXX	XXX	XXX	XXX	XXX	XX	XXX	XX	XX	XX	XX	XX	XX
SI-87	XXX	XXX	XXX	XXX	XXX	XX	XXX	XX	XX	XX	XX	XX	XX
SI-88	XXX	XXX	XXX	XXX	XXX	XX							XX
SI-89	XXX	XXX	XXX	XXX	XXX	XX							XX
SI-90	XXX	XXX	XXX	XXX	XXX	XX							XX
SI-91	XXX	XXX	XXX	XXX	XXX	XX						XX	XX
SI-92A (Q)	XXX	XXX	XXX	XXX	XXX	XXX						XX	XX
SI-92B (P)	XXX	XXX	XXX	XXX	XXX	XXX						XX	XXX
SI-93	XXX	XXX	XXX	XXX	XXX	XXX						XX	XXX
SI-94P	XXX	XXX	XXX	XXX	XXX	XXX						XX	XXX
SI-94Q	XXX	XXX	XXX	XXX	XXX	XXX						XX	XXX
SI-95P	XX	XX	XX	XX	XX	XX						XX	XX

SI-96P	X												
SI-96Q	XX	XX	XX	XX	XX	XX							XX
SI-97P	XX	XX	XX	XX	XX								XX
SI-98P	XX	XX	XX	XX	XX								
SI-99P	X		X										
SI-100P	XX	XX	XX	XX	XX	XX						XX	XX
SI-101P	XX	XX	XX	XX	XX	XX						XX	XX
SI-102P	X	X	X	X	X	X							X
SI-103P	X												
SI-104P	X	X	X	X	X	X							
SI-105P	X	X	X	X	X	X							
SI-106P	X	X	X	X	X								
SI-82	X												

Table 8: Kinematic criteria, strain intensity, and other notes; X = present; XX = common, XXX = abundant

kinematic criteria				deformation intensity			notes
Sample ID	sense of shear criteria	which criteria	sense of shear	strength of fabric	folds	boudined grains	notes
SI-83	XXX	Asymmetric tails, S-C fabric	top to SW	High	XX		bimodal grain size, reddish-brown alteration
SI-84	XXX	Asymmetric tails, S-C fabric	top to SW	High	XX		bimodal grain size
SI-85	XXX	Asymmetric tails, S-C fabric	top to SW	High	XXX		z-folds, bimodal grain size
SI-86	XXX	Asymmetric tails, S-C fabric	Both	High	XX		bimodal grain size
SI-87	XXX	Asymmetric tails, S-C fabric	top to SW	High	XXX		z-folds, bimodal grain size
SI-88	XXX	Asymmetric tails, S-C fabric	top to SW	High	XXX		z-folds, bimodal grain size
SI-89	XXX	Asymmetric tails, S-C fabric	Both	High	XX		bimodal grain size, orange alteration
SI-90	XXX	Asymmetric tails, S-C fabric	Both	High	XX		bimodal grain size, orange alteration
SI-91	XXX	Asymmetric tails, S-C fabric	top to SW	High		XX	bimodal grain size, orange alteration
SI-92A (Q)	XXX	Asymmetric tails, S-C fabric	top to SW	High	X	X	bimodal grain size, orange alteration
SI-92B (P)	XXX	Asymmetric tails, S-C fabric	top to SW	High			Lot of small to large quartz grains
SI-93	XXX	Asymmetric tails, S-C fabric	top to SW	High	XX		z-folds, bimodal grain size
SI-94P	XXX	Asymmetric tails, S-C fabric	Both	High		XXX	bimodal grain size, orange alteration
SI-94Q	XXX	Asymmetric tails, S-C fabrics	Both	High			bimodal grain size, reddish-brown alteration
SI-95P	XX	Asymmetric tails, S-C fabrics	top to SW	Intermediate	XX	XX	variable grain size, reddish-brown alteration

SI-96P	X	Asymmetric tails	top to SW	Low			
SI-96Q	XX	Asymmetric tails, S-C fabrics	top to SW	Intermediate			variable grain size, reddish-brown alteration
SI-97P	XX	Asymmetric tails, S-C fabrics	top to SW	Intermediate	XX	XX	
SI-98P	XX	Asymmetric tails	top to SW	Intermediate	X	X	bimodal grain size, crenulations
SI-99P	XX	Asymmetric tails	top to SW	Intermediate	X		S-fold
SI-100P	XX	Asymmetric tails, S-C fabrics	top to SW	Intermediate			bimodal grain size
SI-101P	XX	Asymmetric tails, S-C fabrics	top to SW	Intermediate			bimodal grain size
SI-102P	X	Asymmetric tails	top to SW	Low			bimodal grain size
SI-103P	X	Asymmetric tails	top to SW	Low			
SI-104P	X	Asymmetric tails	top to SW	Low		X	
SI-105P	X	Asymmetric tails	top to SW	Low		X	reddish-orange alteration
SI-106P	X	Asymmetric tails	top to SW	Low			orange alteration
SI-82	X	Asymmetric tails	top to SW	Low			

9.2.2 Additional Microstructural Quantitative Analysis Data

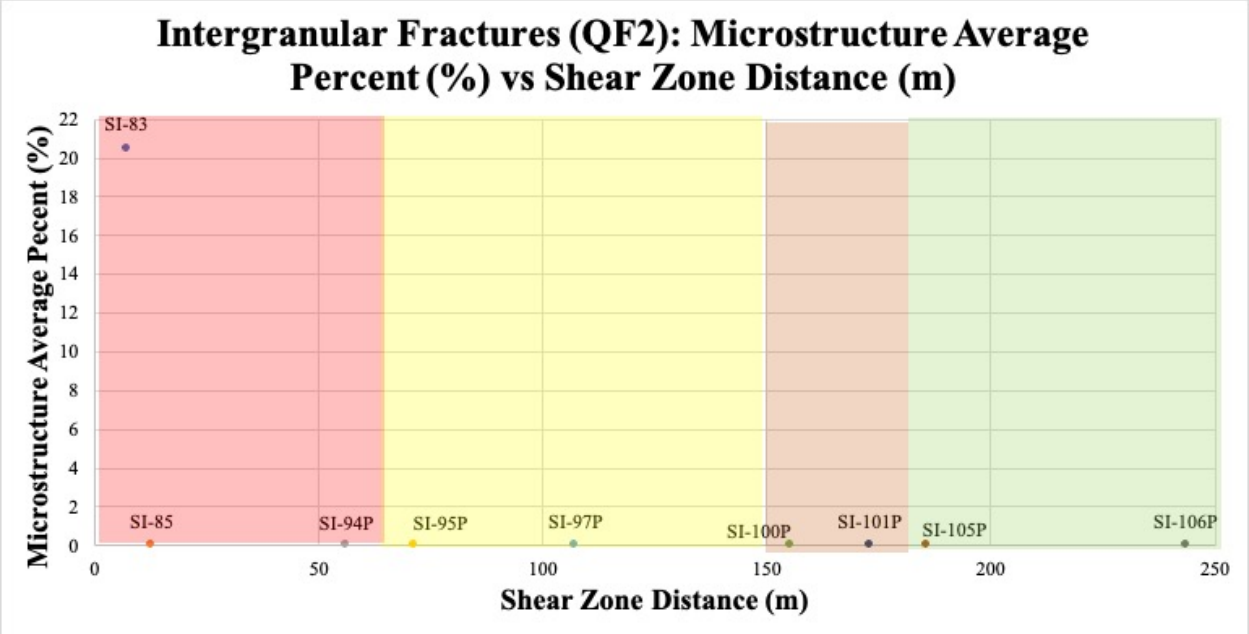

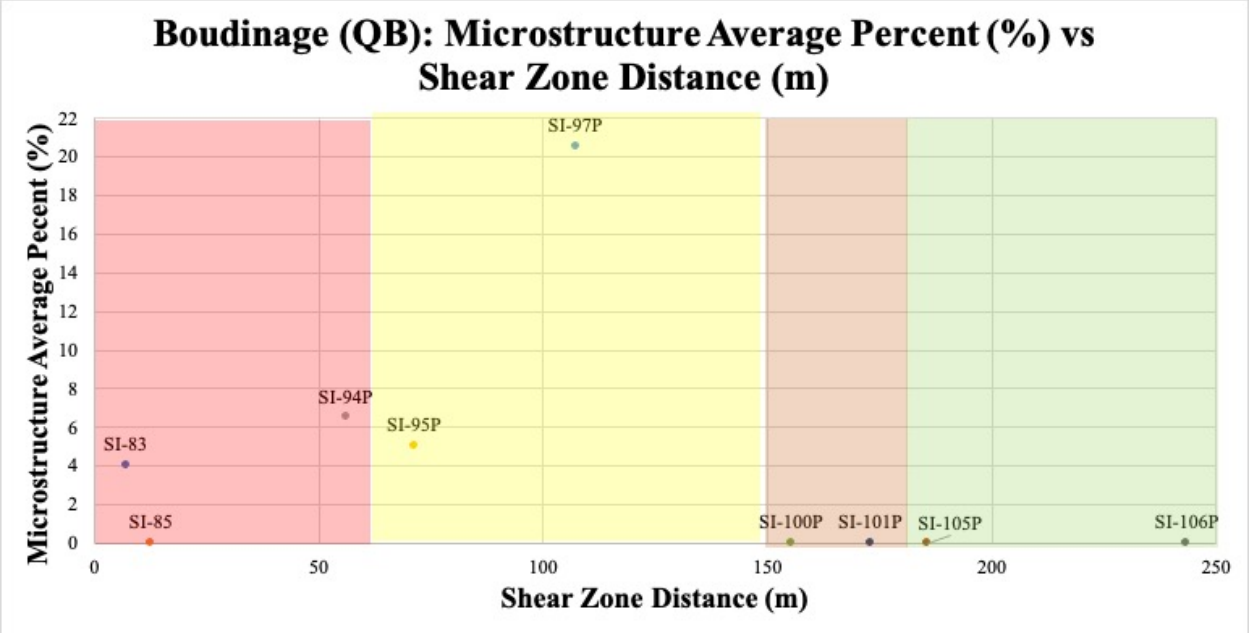

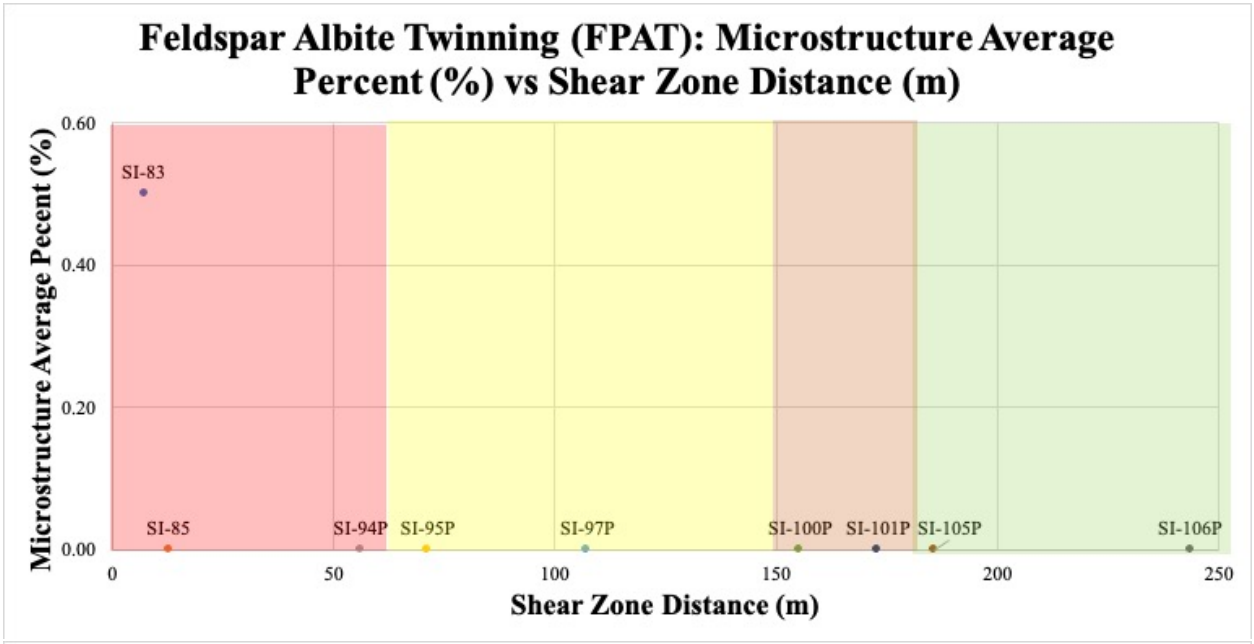
Feldspar Albite Twinning (FPAT): Microstructure Average Percent (%) vs Shear Zone Distance (m)
Microstructure Average Pecent (%)
0.60
0.40
0.20
0.00
SI-83
SI-85
SI-94P
SI-95P
SI-97P
SI-100P
SI-101P
SI-105P
SI-106P
0
50
100
150
200
250
Shear Zone Distance (m)

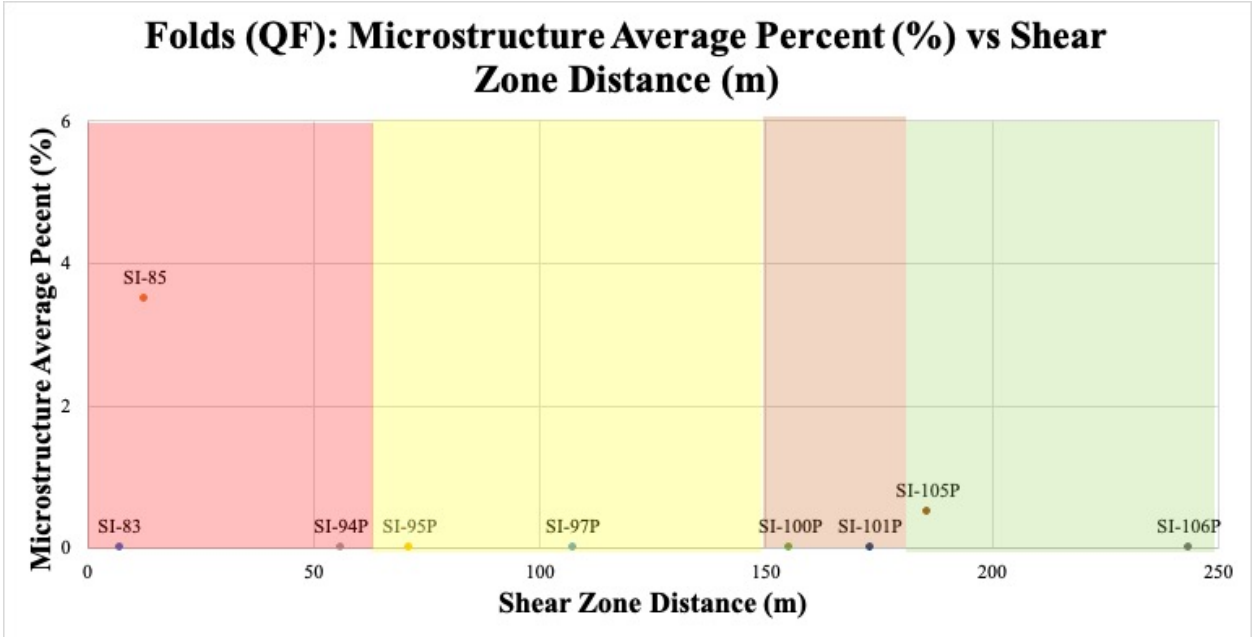
Folds (QF): Microstructure Average Percent (%) vs Shear Zone Distance (m)
Microstructure Average Pecent (%)
6
4
2
0
SI-85
SI-83
SI-94P
SI-95P
SI-97P
SI-100P
SI-101P
SI-105P
SI-106P
0
50
100
150
200
250
Shear Zone Distance (m)

Table 9: Point count data of mineral assemblages in the 9 thin sections of Almonaster.

Sample #	Quartz	Biotite	Muscovite	Albite	K-feldspar	Garnet	Chlorite	Cryptocrystalline orange/red/brown grain
SI83	53.27	27.14	19.10	Trace	Trace	Trace	Trace	Trace
SI85	39.50	32.50	27.50	Trace	Trace	Trace	Trace	Trace
SI94P	33.5	20	45	Trace	Trace	Trace	Trace	1.50
SI95P	31	4.50	61.50	None	None	None	None	3
SI97P	28.64	32.66	38.69	None	None	None	None	Trace
SI100P	15.68	36.76	47.57	None	None	None	None	Trace
SI101P	43	21	36	Trace	None	None	None	Trace
SI105P	17.68	35.86	46.46	Trace	None	None	None	Trace
SI106P	16.32	34.74	48.95	Trace	None	None	None	Trace

9.3 X-ray Methods data

Table 10: Relative abundances of minerals in samples from Almonaster La Real y La Escalada (ALR) and Alajar, where XX represents more abundant minerals, X represents minerals present in lower amounts, and + represents minerals that are detectable but rare.

Transect Name	Sample ID	Quartz	Muscovite	Chlorite	Albite
ALR	SI-110A	XX	XX	X	+
ALR	SI-110B	XX	XX	XX	+
ALR	SI-110C	XX	XX	XX	+
ALR	SI-82	XX	XX	XX	+
ALR	SI-109A	XX	XX	XX	+
ALR	SI-109B	XX	XX	XX	+
ALR	SI-109D	XX	XX	XX	+
ALR	SI-109C	XX	XX	XX	+
Alajar	SI-111	XX	XX	X	+
Alajar	SI-112	XX	XX	XX	+
Alajar	SI-113	XX	XX	X	+
Alajar	SI-114	XX	XX	XX	+
Alajar	SI-115	XX	XX	XX	+
Alajar	SI-116	XX	XX	XX	+
Alajar	SI-117	XX	XX	X	+
Alajar	SI-118	XX	XX	XX	+

Table 11: X-ray Fluorescence data for all samples. No distances were calculated for the Almonaster y La Escalada and Alajar samples.

Almonaster Transect													
Sample ID	**Distance (m)**	**SIO2**	**TiO2**	**Al2O3**	**Fe2O3**	**MnO**	**MgO**	**CaO**	**Na2O**	**K2O**	**P2O5**	**LOI**	**Sum**
PL-1	17.3	60.7	0.91	18.69	7.88	0.15	1.62	0.20	0.43	4.02	0.14	5.07	94.7
PL-2	21.2	61	0.87	18.02	6.84	0.21	1.43	0.31	0.50	3.90	0.10	4.72	93.2
PL-3	22.7	61.3	0.88	18.52	6.85	0.22	1.57	0.43	0.58	4.34	0.16	4.08	94.9
PL-4	26.6	65.1	0.76	16.3	6.08	0.15	1.62	2.04	2.55	2.24	0.14	2.72	97
PL-5	40.6	61.9	0.88	18.66	6.94	0.22	1.83	0.25	0.32	4.49	0.14	3.76	95.6
PL-6	51.5	51.8	0.93	18.63	12.29	0.22	5.49	0.04	0.05	3.08	0.06	6.17	92.6
PL-7	53.4	61.4	1.01	21.59	4.62	0.10	0.57	0.03	0.41	4.83	0.08	4.41	94.7
PL-8	55.2	68.8	0.83	14.23	7.22	0.11	0.83	0.03	0.24	2.83	0.16	4.10	95.3
PL-9	57.7	55	0.95	19.39	7.25	0.20	1.73	0.03	0.32	4.02	0.08	4.64	89
PL-10	60.4	71.8	0.72	14.14	5.08	0.12	0.92	0.03	0.19	2.94	0.07	3.29	96
PL-11	62.2	59.8	0.86	19.49	6.93	0.17	0.88	0.05	0.57	3.46	0.07	4.7	92.3
PL-12	65.5	67	0.78	15.85	6.48	0.12	1.13	0.04	0.35	2.85	0.07	4.56	94.7
PL-13	68.1	52	1.14	26.42	6.51	0.06	0.17	0.13	0.92	4.95	0.09	5.72	92.4
PL-14	76.7	68.8	0.70	15.37	4.80	0.08	0.46	0.09	0.41	2.34	0.05	4.87	93.1
PL-15	82.9	61.4	0.95	17.03	8.13	0.07	1.84	0.04	0.20	2.82	0.17	5.54	92.7
PL-16	92.4	60.2	1.02	17.52	7.88	0.15	2.38	0.10	0.40	2.68	0.13	5.26	92.5
PL-17	98	61.7	1.17	19.56	5.32	0.04	0.55	0.06	0.73	3.45	0.07	4.56	92.7
PL-18	122.8	61.3	1.03	20.34	6.58	0.09	0.62	0.24	0.88	2.15	0.09	4	93.3
PL-19	171.1	57	0.99	18.8	6.77	0.04	1.08	0.03	0.38	3.94	0.10	4.29	89.1
PL-20	192.6	54.2	1.08	24.17	6.62	0.07	1.10	0.08	0.70	4.55	0.08	4.44	92.7
SI-82	>400	55.5	0.97	21.74	8.02	0.06	1.28	0.23	0.55	3.46	0.05	0.05	91.9
Almonaster y La Escalada Transect													
Sample ID	**Distance (m)**	**SIO2**	**TiO2**	**Al2O3**	**Fe2O3**	**MnO**	**MgO**	**CaO**	**Na2O**	**K2O**	**P2O5**	**LOI**	**Sum**
SI-110A		63.3	0.93	15.21	7.17	0.08	1.72	0.09	0.46	2.77	0.09	0.05	97
SI-110B		73	0.65	14.54	3.21	0.02	0.59	0.07	0.19	3.17	0.05	0.04	98.8
SI-110C		59.5	0.85	18.44	9.01	0.12	1.80	0.07	0.06	3.57	0.10	0.06	98.1
SI-109A		53.3	0.99	24.33	7.26	0.14	1.48	0.03	0.35	5.31	0.05	0.05	97.1
SI-109B		54.5	0.93	22.97	7.33	0.12	1.64	0.07	0.47	5.01	0.08	0.05	97.8
SI-109C		53.8	0.93	22.81	6.50	0.12	1.36	0.08	0.53	5.2	0.07	0.04	94.7
SI-109D		54.7	1.07	23	6.61	0.10	1.45	0.14	0.63	5.13	0.07	0.05	98.6

Alajar Transect													
Sample ID	**Distance (m)**	**SIO2**	**TiO2**	**Al2O3**	**Fe2O3**	**MnO**	**MgO**	**CaO**	**Na2O**	**K2O**	**P2O5**	**LOI**	**Sum**
SI-111		72.5	0.25	13.37	2.67	0.04	0.52	1.86	3.34	3.32	0.10	0.01	97.4
SI-112		61.4	0.97	17.34	7.28	0.14	1.87	0.66	1.12	3.93	0.18	0.03	98.4
SI-113		64	0.81	15.76	7.31	0.13	1.56	0.17	1.18	2.73	0.10	0.04	96.8
SI-114		59.7	0.98	16.95	6.59	0.13	1.82	0.44	1.69	3.24	0.16	0.04	93.5
SI-115		65	0.84	16.85	6	0.08	1.48	0.11	0.60	3.41	0.11	0.04	97.9
SI-116		56.5	1.12	19.26	9.09	0.08	2.44	0.09	0.66	3.23	0.14	0.06	99.1
SI-117		55.5	0.99	22.27	7.55	0.09	1.09	0.13	0.46	4.68	0.10	0.06	97.8
SI-118		53.2	0.92	20.67	10.51	0.21	2.24	0.10	0.20	4.46	0.15	0.06	97.8

9.4 Vorticity data

Table 12: Vorticity calculations from nine select samples that were chosen for detailed analysis.

Transect	Sample ID	Distance (m)	Angle (C' to C)	Angle in radians	W_n
Almonaster	SI-83	7.2	28.4	0.50	0.88
Almonaster	SI-83	7.2	28.4	0.50	0.88
Almonaster	SI-83	7.2	28.4	0.50	0.88
Almonaster	SI-83	7.2	28.4	0.50	0.88
Almonaster	SI-83	7.2	28.4	0.50	0.88
Almonaster	SI-83	7.2	28.4	0.50	0.88
Almonaster	SI-83	7.2	28.4	0.50	0.88
Almonaster	SI-83	7.2	28.4	0.50	0.88
Almonaster	SI-83	7.2	28.4	0.50	0.88
Almonaster	SI-83	7.2	28.4	0.50	0.88
				Average	**0.88**

Transect	Sample ID	Distance (m)	Angle (C' to C)	Angle in radians	Wn
Almonaster	SI-85	12.8	44.6	0.78	0.71
Almonaster	SI-85	12.8	45	0.79	0.71
Almonaster	SI-85	12.8	43.7	0.76	0.72
Almonaster	SI-85	12.8	43.7	0.76	0.72
Almonaster	SI-85	12.8	43.7	0.76	0.72
Almonaster	SI-85	12.8	43.7	0.76	0.72
Almonaster	SI-85	12.8	43.7	0.76	0.72
Almonaster	SI-85	12.8	45.3	0.79	0.70
Almonaster	SI-85	12.8	46	0.80	0.69
Almonaster	SI-85	12.8	43.5	0.76	0.73
				Average	**0.72**

Transect	Sample ID	Distance (m)	Angle (C' to C)	Angle in radians	Wn
Almonaster	SI-94P	56.1	12	0.21	0.98
Almonaster	SI-94P	56.1	12	0.21	0.98
Almonaster	SI-94P	56.1	12	0.21	0.98
Almonaster	SI-94P	56.1	12	0.21	0.98
Almonaster	SI-94P	56.1	12	0.21	0.98
Almonaster	SI-94P	56.1	12.9	0.23	0.97
Almonaster	SI-94P	56.1	12	0.21	0.98
Almonaster	SI-94P	56.1	12	0.21	0.98
Almonaster	SI-94P	56.1	12	0.21	0.98
Almonaster	SI-94P	56.1	12	0.21	0.98
				Average	**0.98**

Transect	Sample ID	Distance (m)	Angle (C' to C)	Angle in radians	Wn
Almonaster	SI-95P	71.3	47	0.82	0.68
Almonaster	SI-95P	71.3	47	0.82	0.68
Almonaster	SI-95P	71.3	47	0.82	0.68
Almonaster	SI-95P	71.3	47	0.82	0.68
Almonaster	SI-95P	71.3	47	0.82	0.68
Almonaster	SI-95P	71.3	47	0.82	0.68
Almonaster	SI-95P	71.3	47	0.82	0.68
Almonaster	SI-95P	71.3	47	0.82	0.68
Almonaster	SI-95P	71.3	47	0.82	0.68
Almonaster	SI-95P	71.3	47	0.82	0.68
				Average	**0.68**

Transect	Sample ID	Distance (m)	Angle (C' to C)	Angle in radians	Wn
Almonaster	SI-97P	107.3	24	0.42	0.91
Almonaster	SI-97P	107.3	24	0.42	0.91
Almonaster	SI-97P	107.3	24	0.42	0.91
Almonaster	SI-97P	107.3	24	0.42	0.91
Almonaster	SI-97P	107.3	30	0.52	0.87
Almonaster	SI-97P	107.3	24	0.42	0.91
Almonaster	SI-97P	107.3	24	0.42	0.91
Almonaster	SI-97P	107.3	24	0.42	0.91
Almonaster	SI-97P	107.3	24	0.42	0.91
Almonaster	SI-97P	107.3	34	0.59	0.83
				Average	**0.90**

Transect	Sample ID	Distance (m)	Angle (C' to C)	Angle in radians	Wn
Almonaster	SI-100P	155.4	29	0.51	0.87
Almonaster	SI-100P	155.4	29	0.51	0.87
Almonaster	SI-100P	155.4	29	0.51	0.87
Almonaster	SI-100P	155.4	29	0.51	0.87
Almonaster	SI-100P	155.4	29	0.51	0.87
Almonaster	SI-100P	155.4	29	0.51	0.87
Almonaster	SI-100P	155.4	29	0.51	0.87
Almonaster	SI-100P	155.4	29	0.51	0.87
Almonaster	SI-100P	155.4	29	0.51	0.87
Almonaster	SI-100P	155.4	29	0.51	0.87
				Average	**0.87**

Transect	Sample ID	Distance (m)	Angle (C' to C)	Angle in radians	Wn
Almonaster	SI-101P	173	31	0.54	0.86
Almonaster	SI-101P	173	31	0.54	0.86
Almonaster	SI-101P	173	31	0.54	0.86
Almonaster	SI-101P	173	31	0.54	0.86
Almonaster	SI-101P	173	31	0.54	0.86
Almonaster	SI-101P	173	31	0.54	0.86
Almonaster	SI-101P	173	31	0.54	0.86
Almonaster	SI-101P	173	31	0.54	0.86
Almonaster	SI-101P	173	31	0.54	0.86
Almonaster	SI-101P	173	31	0.54	0.86
				Average	**0.86**

Transect	Sample ID	Distance (m)	Angle (C' to C)	Angle in radians	Wn
Almonaster	SI-105P	185.8	21	0.37	0.93
Almonaster	SI-105P	185.8	21	0.37	0.93
Almonaster	SI-105P	185.8	21	0.37	0.93
Almonaster	SI-105P	185.8	21	0.37	0.93
Almonaster	SI-105P	185.8	21	0.37	0.93
Almonaster	SI-105P	185.8	21	0.37	0.93
Almonaster	SI-105P	185.8	21	0.37	0.93
Almonaster	SI-105P	185.8	21	0.37	0.93
Almonaster	SI-105P	185.8	21	0.37	0.93
Almonaster	SI-105P	185.8	21	0.37	0.93
				Average	**0.93**

Transect	Sample ID	Distance (m)	Angle (C' to C)	Angle in radians	Wn
Almonaster	SI-106P	243.5	29	0.51	0.87
Almonaster	SI-106P	243.5	29	0.51	0.87
Almonaster	SI-106P	243.5	32	0.56	0.85
Almonaster	SI-106P	243.5	29	0.51	0.87
Almonaster	SI-106P	243.5	29	0.51	0.87
Almonaster	SI-106P	243.5	29	0.51	0.87
Almonaster	SI-106P	243.5	29	0.51	0.87
Almonaster	SI-106P	243.5	29	0.51	0.87
Almonaster	SI-106P	243.5	29	0.51	0.87
Almonaster	SI-106P	243.5	29	0.51	0.87
				Average	**0.87**